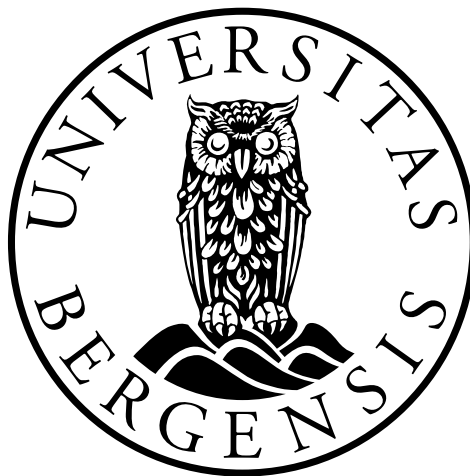


Characterization of 3D Silicon Microdosimeters and corresponding Readout System

by
Øyvind Lye

**THESIS
for the degree of
MASTER OF SCIENCE IN PHYSICS
(Specialisation in Microelectronics)**



Department of Physics and Technology
University of Bergen

September 2016

Abstract

This thesis is related to the 3DMiMic micro-dosimeter project by SINTEF and the University of Wollongong. 3DMiMic is made to mimic the response of biological tissue to radiation, and will be used to learn more about the effects of radiation to tissue on a small scale. This knowledge can be used to reduce the uncertainties when treating cancer with particle radiotherapy, which will lead to more successful treatments. The thesis includes some work on the characterization of the 3DMiMic detectors. This includes I-V & C-V characterisation and measurements with radiation. A circuit board to interface the detectors has also been created. The measurements show good results for the newest revisions of the detectors, and suggests that the collaboration project has been a success.

The main focus of the thesis has been the readout electronics for the 3DMiMic detectors. The work started with assembling a list of viable systems with their relevant properties. The system selected as the main focus for the thesis was an early prototype pre-amplifier & shaper by IDEAS, called IDE1180. As an early prototype, the IDE1180 needed a lot of tests before it could be properly compared to other, more proven, systems. The work includes gain characterization, and measurements on noise, pulse shape, dynamic range, crosstalk, power consumption, and pile-up. The thesis shows some unexpected gain behaviour that must be considered before use, and noise measurements that are higher than shown in the datasheet. Because of the high noise requirements for the 3DMiMic detectors, the thesis does not recommend using this system for these detectors at its current state, but it is recommended to pay attention to future revisions.

Acknowledgements

First of all, I would like to thank my supervisor Professor Kjetil Ullaland for helping me when needed and for running the microelectronics group. Secondly, I would like to thank my co-supervisor Professor Dieter Röhrich for giving me the opportunity to work with a project related to something as important as cancer research.

A huge thanks to Andreas Samnøy who has in practice worked as a co-supervisor for me due to Dieter's busy schedule. It has been great to have you around to bring advice and laughs. I would also like to thank Thomas Poulianitis and Sanjeeda Sharmin for the cooperation and discussions.

I would like to thank Marco Povoli for letting me and Andreas come to SINTEF to work on the detectors, and for letting me pick the detectors up on short notice when they were ready. Related to this, I would like to thank Jørgen Lien, Kristin Imenes, and Thai Anh Tuan Nguyen for on very short notice letting me borrow the wire-bonding machine at Vestfold Innovation Park. Special thanks to Tuan for assistance with the bonding. Also thanks to everyone else who has helped me with the project in some way.

Finally, I would like to thank to my friends and family for always being there. A special thanks to Ole Faltin, Lars Bratrud, Torgrim Næss, Daniel Follesø, Vaffel (they know who they are), and everyone in room 312.

Contents

Abstract	i
Acknowledgements	iii
1 Introduction	1
1.1 Background and Motivation	1
1.2 About this work	2
1.3 Structure of the Thesis	2
1.3.1 Note on Citations	3
1.4 Scientific Environment	4
2 Radiation and Radiotherapy	5
2.1 Radiation	5
2.1.1 Interactions of Radiation with Matter	5
2.1.2 Biological Effects of Radiation	7
2.2 Radiation Therapy	9
2.2.1 Proton Therapy	10
2.2.2 Carbon Therapy	13
2.2.3 Relative Biologic Effectiveness	14
3 Testing and Characterization of the 3DMiMic Detector	15
3.1 Semiconductors	15
3.1.1 Semiconductor Diodes	15
3.2 Radiation Detectors	16
3.2.1 Semiconductor Detectors	17
3.3 Semiconductor Characterization	18
3.3.1 Capacitance-Voltage Measurements	18
3.3.2 Current-Voltage Measurements	19
3.4 3DMiMic	19
3.4.1 3DMiMic Response to Radiation	22
3.5 I-V Measurements of 3DMiMic Detectors on Wafer	22
3.6 Detector Interface PCB	25
3.7 Wire Bonding	26
3.8 I-V Measurements of 3DMiMic Detectors on PCB	26

3.9	C-V Measurements of 3DMiMic Detectors	29
3.10	Radiation Measurements with Americium source	30
4	Readout Electronics for the 3DMiMic Detectors	33
4.1	Detector Readout	33
4.1.1	Pre-Amplifier	33
4.1.2	Shaper	35
4.1.3	Analog-to-Digital Conversion	38
4.2	Choice of Readout Electronics for the 3DMiMic Detectors	39
4.2.1	Medipix and Timepix	39
4.2.2	UiO Portable Front-End Readout System	39
4.2.3	IDEAS IDE1180 Amadeus Preamp-Shaper	40
4.2.4	Ortec 142A Pre-Amplifier	40
4.3	Portable PCIe ADC System	40
4.3.1	SP Devices ADQ14AC-4C ADC	41
5	Characterization of IDE1180	43
5.1	Measurement Setups	44
5.2	Gain vs. Input Load Capacitance	47
5.2.1	Gain vs. Capacitance Simulations	50
5.2.2	Ballistic deficit	52
5.3	Noise Measurements	54
5.3.1	Gain Compensation	56
5.3.2	Noise from Input Circuitry	58
5.4	Gain Linearity	59
5.5	Dynamic Range	60
5.5.1	Input Sharing	61
5.6	Shaping Time	61
5.7	Peaking Time	62
5.8	Crosstalk	63
5.9	Power Consumption	64
5.10	Pile-up Considerations	65
5.11	The 7048 Evaluation Board	65
Conclusions & Outlook	67	
Appendices	69	
A 3DMiMic Layouts	70	

B 3DMiMic I-V Measurements	74
C Detector Interface PCB	77
D List of Readout Electronics Systems	84
E IDE1180 Gain Linearity Graphs	86
F IDE1180 Shape Graphs	88
Bibliography	90
Glossary	94

Chapter 1: Introduction

1.1 Background and Motivation

In 2013 the Norwegian government started a project to build centers for cancer treatment using particle radiotherapy. The main reason for this is that radiotherapy using heavy charged particles does less damage to healthy tissue than the more conventional radiotherapy using photons that Norway has today. Many photon radiotherapy patients develop cancer again a few decades after the original treatment as a result of the treatment radiation, which makes photon radiotherapy little suited for treating cancer in children. Every year 1000 to 1500 Norwegians will experience fewer side effects by being treated with protons instead of photons [Lynnebakken, 2012]. When treating cancer with heavy charged particles it is critical to be able to deposit the energy of the radiation at the correct position inside the patient, both to kill the tumor and to avoid unnecessary damage to healthy tissue around the tumor.

To be able to assure the quality of the treatment system, the oncologists need to be able to predict how the energy from a beam of heavy charged particles will be absorbed in the body. The uncertainties because of the lack of knowledge on this causes an increased risk of side effects for particle therapy patients. To bolster the research on the effects of radiation on humans, SINTEF, together with the University of Wollongong, is developing a silicon based radiation detector, named 3DMiMic, which mimics the response of biological tissue to ionizing radiation on a cellular and sub-cellular level. By measuring how the energy is distributed in the detector, researchers will learn more about how radiation effects tissue on a small scale, which will reduce the uncertainties in future treatment systems. [SINTEF, 2015]

1.2 About this work

The original goal of the thesis was to read the data from the 3DMiMic detector into a computer. The thesis should also include some work on characterizing the detectors, and radiation tests with an alpha source at the University of Bergen, and hopefully also tests in a proton beam facility. The Medipix family of chips were considered as possibilities for the first stage of the readout system.

Many of the projects goal changed during the work on the thesis. Firstly, the detectors, which had been expected to be delivered in August 2015, were delayed multiple times and not received until June 2016. This lead to the planned work on the detectors being reduced. When the work on the thesis started, it turned out that the Medipix chips are not usable for this project. Some time was spent to assess available readout systems from different sources and how well they compare to the 3DMiMic specifications.

The work that was done on the detectors was design of a PCB, I-V measurements on wafer and PCB, C-V measurements on PCB, and basic radiation tests with an alpha-source. Concerning the readout electronics, the thesis mostly focused on characterizing the IDE1180 pre-amplifier and shaper by IDEAS.

1.3 Structure of the Thesis

Chapter 1: Introduction

Introduces the thesis, including background, motivation and goals.

Chapter 2: Radiation and Radiotherapy

Includes theory of ionizing radiation, biological effects of radiation, and radiotherapy.

Chapter 3: Testing and Characterization of the 3DMiMic Detector

Includes theory about radiation detectors, an introduction to the 3DMiMic detectors, and measurement results from the detectors.

Chapter 4: Readout Electronics for the 3DMiMic Detectors

Background theory on detector readout, and short introductions to the main readout electronics systems that were considered for this project.

Chapter 5: Characterization of IDE1180

Measurement setups, results, and conclusions from the characterization of the IDE1180 pre-amplifier shaper from IDEAS.

Conclusions & Outlook

Main conclusions from the work, and outlook for the continuation of the 3DMiMic project.

Appendix A: 3DMiMic Layouts

Figures and explanations on the different 3DMiMic layouts and wafers.

Appendix B: 3DMiMic I-V Measurements

Figures with all I-V measurements done at SINTEF.

Appendix C: Detector Interface PCB

Description of the interface PCB that was made for the 3DMiMic detectors. Includes pictures of how the detectors should be wire-bonded to the PCB.

Appendix D: List of Readout Electronics Systems

Table including all readout electronics systems that was considered for the project with relevant specifications.

Appendix E: IDE1180 Gain Linearity Graphs

Figures with all gain linearity measurements. Includes gain and dynamic range.

Appendix F: IDE1180 Shape Graphs

Figures with all measurements on peaking time and shaping time.

1.3.1 Note on Citations

Citations in this thesis generally follows the guidelines recommended for Wikipedia authors. A citation placed after the last punctuation in a paragraph supports multiple claims through the paragraph, while a citation placed before a punctuation only supports one or a few claims just before the citation. In this thesis, citations at the end of a paragraph is much used in the theory sections, where they refer to sources with more detailed information for the interested reader.

1.4 Scientific Environment

This master project is supervised by Professor Kjetil Ullaland in the electronics and measurement science research group at the Department of Physics and Technology (IFT) at the University of Bergen (UiB). The 3DMiMic project is a part of the subatomic physics research group at IFT and this master project was assigned by Professor Dieter Röhrich. The dissertation of Röhrich's Ph.D. student Andreas Tefre Samnøy shares many of this master projects objectives. Post doctor Kristian Smeland Ytre-Haugen at IFT leads an ongoing project that looks into microdosimetry and relative biological effectiveness of proton and heavy ion therapy.

SINTEF's department of Microsystems and Nanotechnology produces the 3DMiMic pixel detector that this project is based on. The University of Wollongong (UOW) in Australia designed the detectors. The University of Oslo (UiO) is also involved in the 3DMiMic project.

Chapter 2: Radiation and Radiotherapy

2.1 Radiation

Radiation is defined as the emission and propagation of energy through space or a material medium. *Particle radiation* refers to energy propagated by particles with a definite rest mass. A particle beam is a group of particles that move in the same direction, similar to a light beam. Examples of these particles are electrons, neutrons, protons, and heavy ions. *Electromagnetic radiation* is energy propagated by the massless photons in phenomena such as light waves, radio waves, microwaves, X-rays, and gamma (γ) rays. Electromagnetic waves propagate at the speed of light (in vacuum) and are represented by the spatial intensity variations of an electric field and a magnetic field. [Khan and Gibbons, 2014, chap. 1]

Ionizing radiation carries enough energy to break molecular bonds by *ionizing* atoms it passes, meaning that the atom acquires a positive or negative charge. If the radiation strips an electron from the atom, the latter becomes a positive ion. If a stripped electron later combines with a neutral atom, it becomes a positive ion. Charged particles with enough kinetic energy are called *directly ionizing radiation* because they can ionize atoms through collisions. [Khan and Gibbons, 2014, chap. 5]

2.1.1 Interactions of Radiation with Matter

Interactions of charged particles with matter

Charged particles, for example protons, primarily interact by ionization and excitation. Electrons also commonly react through bremsstrahlung (deceleration radiation), where the particle is decelerated and emits the lost kinetic energy as a photon. When charged particles travel through a medium, they interact with atomic electrons and nuclei through the Coulomb force. These interactions can be inelastic collisions with atomic electrons, or elastic scattering without energy loss. In the inelastic collisions, the particle loses part of its kinetic energy to produce ionizations and excitations of atoms. This results in energy being absorbed in the medium as the particle is decelerated. [Khan and Gibbons, 2014, chap. 5 & 27]

Stopping power is the average energy loss of a particle per unit path length ($-dE/dx$) in a medium. The Linear Energy Transfer (LET) of a particle is the energy locally deposited per length and is usually expressed in MeV/cm or keV/ μ m. The LET will always be equal to or smaller than the stopping power. These parameters are used to describe energy deposition in matter and the biological effect of radiation (see section 2.1.2). The LET of a heavy charged particle (a particle of equal or greater mass than a proton) travelling through matter is inversely proportional to the square of its velocity. This means that as the particle loses energy and slows down, the rate of energy loss will increase and the particle slows down at a faster rate. The rate of energy loss (and energy deposition in the medium) becomes maximum as the particle velocity approaches zero. This leads to the particle stopping relatively quickly after travelling a certain distance and makes it possible to define a range for a certain type of particle with a defined energy in a type of matter. The intensity of a particle beam plotted versus depth in tissue can be seen in figure 2.1 where the sudden drop in the proton plots is defined as the particle's range for that energy. [Khan and Gibbons, 2014, chap. 27]

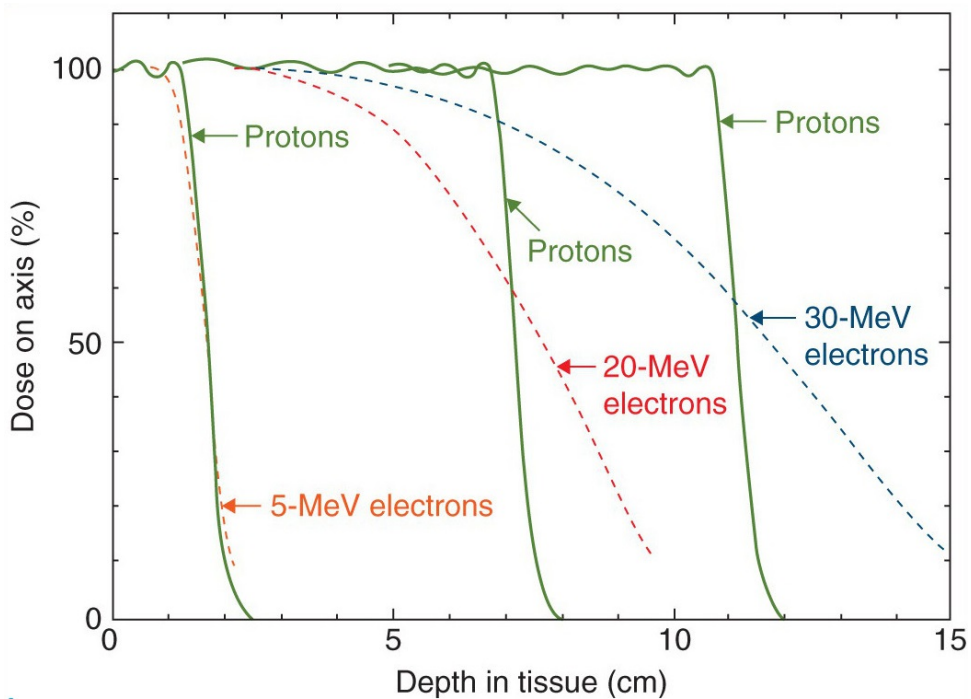


Figure 2.1: Comparison of depth dose distribution for protons and electrons of different energies. [Khan and Gibbons, 2014, fig. 5.15]

Interactions of photons with matter

The five dominating processes for photon interactions with matter are Rayleigh scattering, the photoelectric effect, the Compton effect, pair production, and photodisintegration. Rayleigh scattering happens when a low energy photon collides with an electron and is scattered to a different angle. This does not deposit any energy in the medium, but the photon is scattered away from its original path. The photoelectric effect is a phenomenon where all the energy of a photon is absorbed in an atom. This leads to one of the orbital electrons being emitted, and the shell vacancy will lead to emission of X-rays as a higher energy electron fills the vacancy. Occasionally, these X-rays will also cause more electrons to be emitted. The Compton effect is when a photon collides with a quasi-free electron, scattering the photon and transferring some of its energy to the electron. This is given to the electron as kinetic energy. Pair production can happen with photons of energy greater than 1.022 MeV, where a photon travelling near an atomic nucleus gives all its energy to produce an electron and a positron. The positron will later find an atomic electron and they will annihilate each other by producing two photons of 0.511 MeV each. A high energy photon can cause photodisintegration by reacting with an atomic nucleus, leading to a nuclear reaction. [Khan and Gibbons, 2014, chap. 2 & 5]

Due to all the above processes, a photon travelling through matter will at each instant in time have a certain chance of being absorbed or scattered by the medium. Because of this, the intensity of a photon beam will start to go down instantly when it leaves vacuum, but will never be reduced to zero, see figure 2.2. It is therefore very difficult to simply define the range of a photon beam, as can be done with a beam of heavy charged particles. The reduction in the number of photons is proportional to the number of incident photons through the *attenuation coefficient*. [Khan and Gibbons, 2014, chap. 5]

2.1.2 Biological Effects of Radiation

As discussed in the previous sections, radiation travelling through matter deposits energy in the medium. Examining the effects of this in biological tissue is an extremely complex field. Non-ionizing radiation can heat the matter it passes through. Ionizing radiation is much more dangerous as it breaks molecular bonds, causing molecules to fall apart. This can cause massive damage to tissue cells, change the genetic material (DNA), and destroy the components that produce red blood cells. [Young et al., 2007, chap. 43]

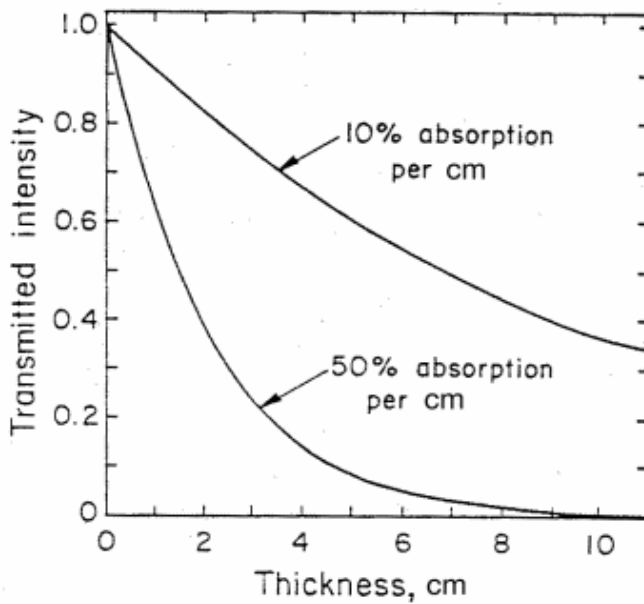


Figure 2.2: Photon intensity through an absorber as a function of thickness [ASU, 2000]

When a cell has been damaged by radiation, there are three possible effects: The cell dies, the cell is repaired correctly, or the cell is repaired incorrectly. The human body has very effective repair mechanisms which constantly repair cellular damage, including damage to DNA. Occasionally, these repair mechanisms will perform their function incorrectly, which can result in cells that cannot perform their normal function, or cells that damage other cells. Some of these cells are unable to reproduce themselves, while others reproduced at an uncontrolled rate, which can be the cause of cancers.[JLab]

To be able to describe the quantity of ionizing radiation for all energies, materials, and types of radiation, it is common to use the quantity *absorbed dose*, or simply *dose*, which can be used as a measure of the biologically significant effects that ionizing radiation produces. It is defined as the radiation energy delivered to tissue per unit mass. The SI unit for dose is gray (Gy), where $1\text{Gy} = 1\text{J/kg}$. The quantity *dose equivalent* has been defined because the biological effects of radiation depend on the type of radiation in addition to the dose. Dose equivalent is the dose multiplied by a quality factor for the type of radiation, in units of sievert (Sv). $1\text{Sv} = 1\text{J/kg}$. Additionally, the sensitivity to radiation-induced effects will vary for different types of tissue, leading to the definition of *effective dose equivalent*, defined as "the sum of the weighted dose equivalents for irradiated tissues or organs". [Khan and Gibbons, 2014, chap. 8 & 16]

2.2 Radiation Therapy

Radiation therapy, also known as radiotherapy, is therapy using the biological effects of ionizing radiation to kill or control cancer cells. One of the main principles behind radiotherapy's effectiveness in treating cancer is that radiation causes much more damage to rapidly dividing cells, and tumor cells divide extremely rapidly [Serway and Jewett, 2014, chap. 45]. Roughly half of all cancer patients receive radiotherapy as a part of their treatment. The radiation can originate from a machine outside the body (external beam radiation therapy), or from a radioactive source being placed into the body (internal radiation therapy). Traditional external beam radiation therapy is delivered using photon beams (photon therapy), but treatment with beams of heavy charged particles (commonly called "particle therapy"), like protons (proton therapy) or carbon ions, are becoming more common. Electron beam therapy is also used, mainly to treat cancer close to the surface of the body. [NIH, 2010]

The radiation will also damage healthy tissue, but a lot of work is put into reducing this as much as possible. Planning and simulations are done to increase the certainty of avoiding complications. Detailed imaging scans are done to get a 3D map of the patient's tumor and surrounding areas. The basis for these maps are usually Computed Tomography (CT) scans, but can also be combined with Magnetic Resonance Imaging (MRI), Positron Emission Tomography (PET), X-ray images, or ultrasound scans [NIH, 2010]. One of the main reasons for CT's importance for photon therapy is that since it is based on photon beams, a CT scan also yields the body's tissue-density information and photon attenuation coefficient, which is needed for photon therapy planning. [Khan and Gibbons, 2014, chap. 12]

The particle beams of external beam radiation therapy are of high energy and needs to be produced in or near the treatment machine. For photon therapy, it is most common to accelerate photons using a linear accelerator, which is small enough to fit inside the same room as the patient table [NIH, 2010]. For particle therapy a bigger and more expensive accelerator is needed to accelerate the particles to high enough energies. For proton therapy a cyclotron or a synchrotron is used. [Khan and Gibbons, 2014, chap. 27]

A patient treatment dose is usually delivered once per day every workday for 4-6 weeks. One delivery is called a fraction. Fractionation is done for multiple reasons: One is to allow healthy tissue time to repair the damage from radiation. Another is to increase the chance of hitting the cancer cells at a time when they are vulnerable.

Fractionation also helps to minimize the effects of random variations in the patient's position and internal geometry. [Board of the Faculty of Clinical Radiology, 2006] [Hysing, 2015]

As already mentioned, radiation therapy also damages healthy tissue, which can produce both acute (early) and chronic (late) side effects. Acute side effects occur before the treatment ends, and are usually temporary. Examples include skin irritation, hair loss, fatigue and nausea. Chronic side effects develop months to decades after treatment is complete. Examples are skin damage, memory loss, infertility and secondary cancer. Secondary cancer is the development of a new cancer in a person that has previously had cancer. As this takes a long time to develop, it might not be a very large problem for older patients, but it is critical to avoid secondary cancer when treating cancer in children and adolescents. [NIH, 2010]

When plotting the absorbed dose in water (or tissue), the differences between photon beams and heavy charged particle beams become even more apparent than when plotting the intensities (section 2.1.1). Figure 2.3 shows the relative dose deposited in water for a proton and a photon beam. The photon beam's maximum is very close to the surface, and the photons will damage tissue far into the body. Also, if the tumor is deep into the body, and the beam only comes from one direction, the photons will have to do a lot of damage to the skin to be able to do enough damage to the tumor. Protons (and other heavy charged particles) on the other hand have their maximum deeper into the material, in what is called the *Bragg peak*. Protons deposit less energy before the maximum, and close to no damage behind the maximum.

2.2.1 Proton Therapy

Proton therapy is radiation therapy using high energy proton beams, and is the by far most tested type of particle therapy. The main principle behind the use of proton therapy is to exploit the Bragg peak to deposit a high dose to a tumor, with low dose delivered in front of it, and close to no dose behind. The Bragg peak is very narrow and is not able to cover most tumors, which has lead to the use of superposition of multiple beams of different energies. This superposition is called a Spread-Out Bragg Peak (SOBP), see figure 2.4. A SOBP has a lot higher dose deposited in front of the tumor than a single proton beam, but it is still lower than that of a photon beam. The dose behind the tumor is still low. [Khan and Gibbons, 2014, chap. 27]

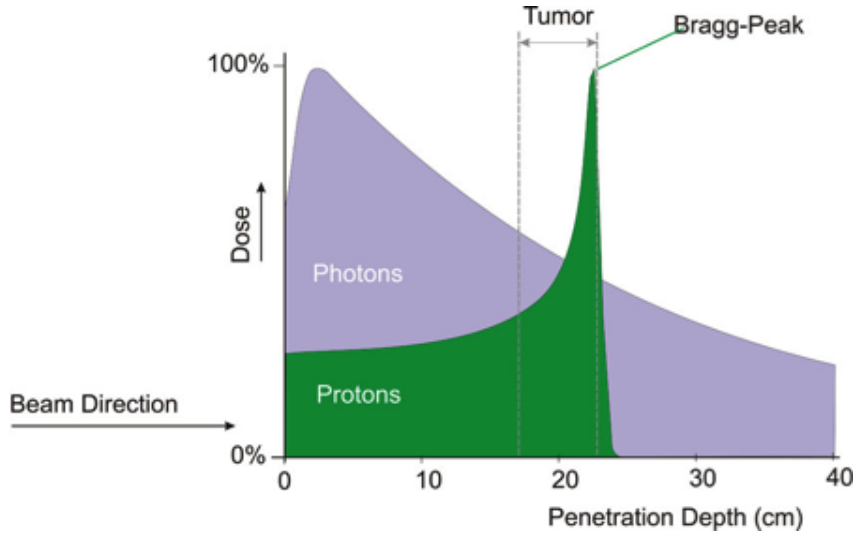


Figure 2.3: Percentage depth dose for a photon beam and a proton beam in tissue. [P-Cure]

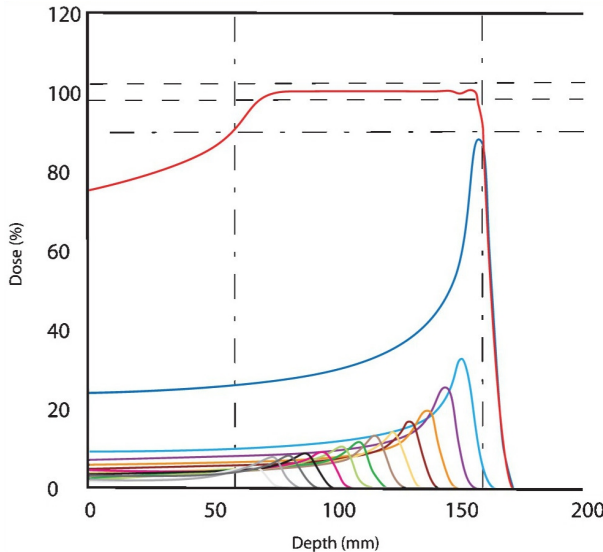


Figure 2.4: SOBP depth dose distribution [Khan and Gibbons, 2014, fig. 27.10]

The shape of the SOBP makes it possible to treat tumors with a lot less dose to the surrounding tissue than with photon therapy, which has two main benefits. One is the ability to treat tumors in close proximity to critical organs without damaging said organ. The other is to avoid the chronic side effects mentioned in section 2.2, which is very important when treating children with cancer [Khan and Gibbons, 2014, chap. 27]. Figure 2.5 compares photon (A) and proton (B) beams, where red is high dose, blue is low dose, and gray is negligible dose.

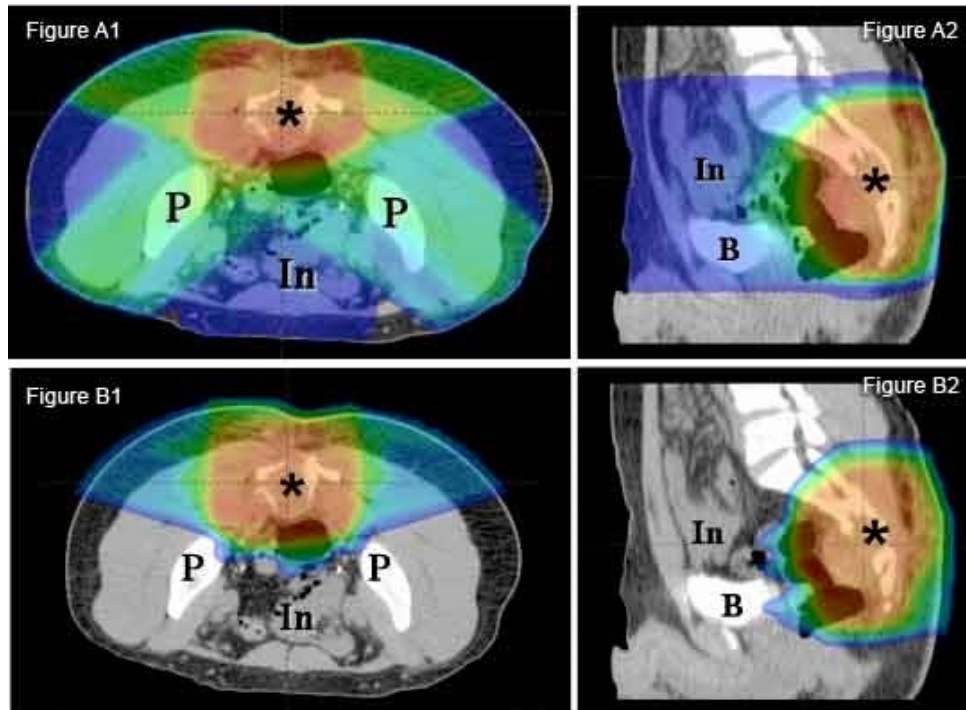


Figure 2.5: Photon (A1 & A2) and proton (B1 & B2) beam dose distributions. [P-Cure]

The geometrical accuracy in proton therapy is a lot more critical than in photon therapy. While a geometrical error between planning and delivery in photon therapy will give a smaller under-dosage to the tumor and over-dosage to surrounding tissue, similar errors in proton therapy could cause part of the tumor receiving no dose at all and healthy tissue receiving full dose, see figure 2.6. Geometrical uncertainties can come from setup and anatomical variations, biological considerations, organ motion, and dose calculation approximations. [Paganetti, 2012]

As mentioned in section 2.2, photon CT yields the patient's photon attenuation coefficient that is needed for photon therapy, but for proton therapy the stopping power is needed to greatly reduce range errors. Therefore proton CT imaging techniques are being developed, based on the same principles as conventional CT, but using low-intensity proton beams instead of photon beams. [Freeman, 2013]

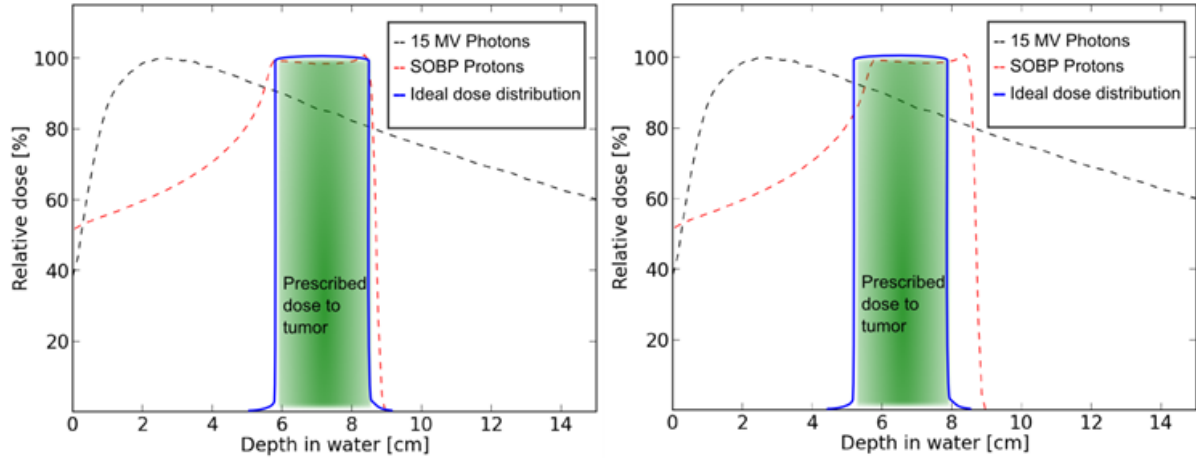


Figure 2.6: Comparison of dose distribution with correct (left) and incorrect (right) range assumptions. [Ytre-Hauge, 2015]

2.2.2 Carbon Therapy

Carbons have also been used clinically for radiotherapy since 1994 in Japan, and 2002 in Germany. Data from these centers suggest that carbon therapy is superior to proton therapy for certain types of cancer. By comparing depth dose distributions, figure 2.7, the carbon ion shows a sharper Bragg peak, but the dose is not reduced to zero after the Bragg peak. This suggests that carbon therapy might be worse than proton therapy when there is a critical organ just behind the tumor. Certain cancer types can however benefit from the sharper Bragg peak, lower entrance dose, and lower lateral spread of dose. As carbons are heavier, they also require more complex and expensive accelerators than protons. [Ytre-Hauge, 2015]

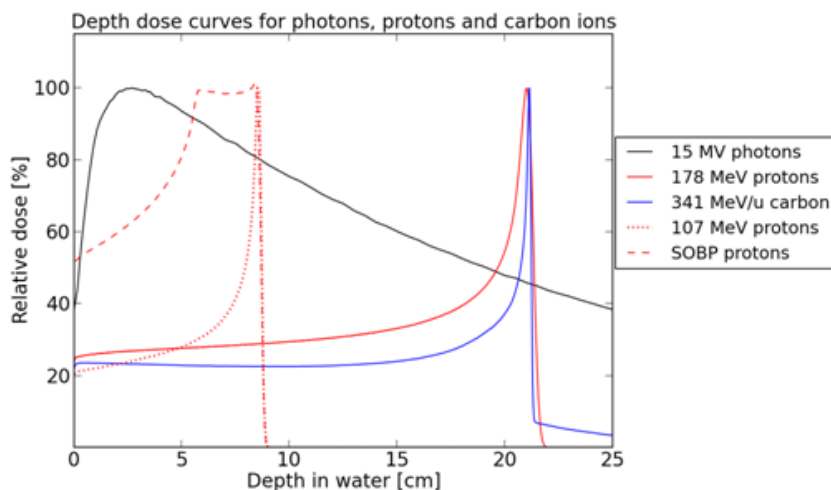


Figure 2.7: Comparison of photon, proton, and carbon depth dose distributions. [Ytre-Hauge, 2015]

2.2.3 Relative Biologic Effectiveness

Since the biological effect of radiation depends of the type of radiation, the term relative dose is often used. This is the physical dose multiplied with the factor Relative Biologic Effectiveness (RBE). The RBE of any radiation is the ratio of the dose of the given radiation to the dose of 250-kVp X-rays that produce the same biologic effect as the given radiation. This effect includes for example cell killing, tissue damage, and mutations. The RBE is critically dependant on the LET. Since the LET of a heavy charged particle is increased as the particle is slowed, the LET and RBE will increase as the particle moves deeper into the body during particle therapy. Because this variation is not well enough investigated, most treatment facilities use a constant RBE of 1.1 for protons. This causes an extra uncertainty that can be avoided by more research into RBE. The RBE for carbons changes a lot more than for protons, starting at about 1 upon entrance, and ending at about 5 in the deepest end of the SOBP, making RBE research even more critical for carbon therapy. [Khan and Gibbons, 2014, chap. 27] [Ytre-Hauge, 2015]

Chapter 3: Testing and Characterization of the 3DMiMic Detector

3.1 Semiconductors

A semiconductor is a material with higher resistance than typical resistive materials, like copper, but lower resistance than insulators. Silicon is the most widely used semiconductor element for electronic devices. A semiconductor's conducting properties can be altered by adding different atoms into the crystal lattice. This is called doping. An n-type semiconductor has been doped with atoms containing more free electrons. A p-type similarly has more free holes. Atoms with extra electrons are called donors, and phosphorus is a common donor for silicon doping. Atoms with extra holes are called acceptors, and boron is a common acceptor for silicon doping. [Knoll, 2010, chap. 11]

3.1.1 Semiconductor Diodes

A basic semiconductor diode is based on a pn junction, which is a p-type material in contact with a n-type material. Without an external bias applied, electrons from the n-region near the junction will recombine with holes in the p-region, leaving behind negatively charged ions in the n-region. The opposite happens in the p-region, creating positively charged ions. This creates a region in the junction with a strong electric field, which is called the depletion region, because it is depleted of charge carriers. This makes the depletion region non-conductive. A pn junction is shown in figure 3.1. The depletion region can be made smaller, eventually causing a current to flow, by setting up a voltage across the junction, with the higher potential on the p-side. This is called forward bias. The opposite, reverse bias, causes the depletion region to grow bigger as the charge carriers are pulled away from the junction. [Gray et al., 2009, chap. 1]

The insulating properties of the depletion region causes only a minimal leakage current to flow during reverse bias. This current is caused by drift, which increases with the electric field up to the point of velocity saturation. The increased interactions between the carriers and the lattice for higher electric fields causes the leakage current to

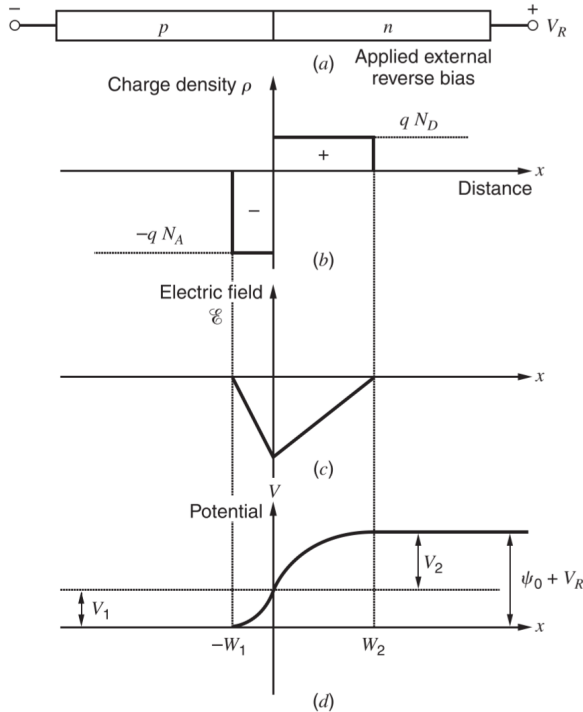


Figure 3.1: PN junction with depletion region. (a) Schematic. (b) Charge density. (c) Electric field. (d) Electrostatic potential. [Gray et al., 2009]

become almost independent of the voltage. This current is often called the reverse saturation current. Once the reverse bias becomes too strong, the high electric field causes the depletion region to break down and high current to flow. This current can break diodes that have not been made to withstand it. Currents for different bias voltages can be seen in figure 3.2. [Gray et al., 2009, chap. 1]

A PIN diode has a large undoped intrinsic semiconductor region between the p-region and n-region. The i-region is flooded with charge carriers from the p- and n-regions. This causes the electric field to cover almost the entire length of the i-region, which speeds up the transport of charge carriers. The depletion region is also independent of the bias voltage. [van Zeghbroeck, 2011]

3.2 Radiation Detectors

A radiation detector records interactions between incoming radiation and the detector. These interactions could be electrical, chemical, light- or heat-based. Detectors can be based on many different materials, including gas chambers, semiconductors, crystals, and liquid. In a simple radiation detector a single particle interacts with the detector, resulting in an electric charge appearing inside the detector. This charge is typically

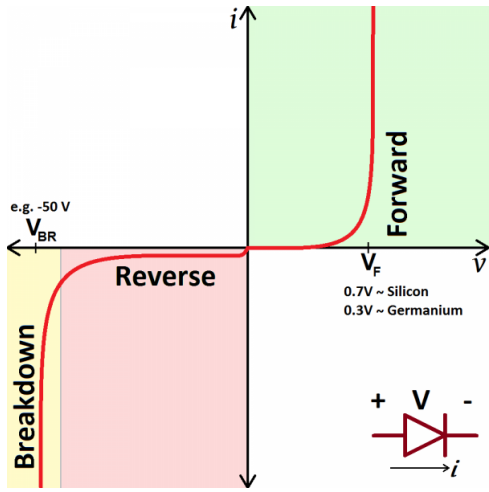


Figure 3.2: Current-voltage relationship of a diode. [SparkFun]

collected by setting up an electric field inside the detector, which causes positive and negative charge to flow in opposite directions, forming an electric signal. This signal could be measured as a current (current mode), voltage (mean square voltage mode), or a charge (pulse mode). [Knoll, 2010, chap. 4]

Pulse mode is the most common readout mode because the measurement records each individual quantum of radiation. Pulse mode is therefore required when attempting to measure the energy of individual radiation events. The charge generated in the detector is usually integrated over a certain period of time. Pulse mode, however, does not work well at very high event rates as the time between events becomes too short to analyse the data. Current mode measures the average current over many events, therefore loosing the amplitude and timing information of individual events, but allowing for measurement with high event rates. Mean square voltage mode works much like current mode, but the output signal will be more dependent on the charge per event, making this mode more useful for mixed radiation environments. [Knoll, 2010, chap. 4]

3.2.1 Semiconductor Detectors

Semiconductor diode detectors, also called simply semiconductor detectors or solid-state detectors, are radiation detectors employing semiconductor diodes as the basic detection medium. Semiconductor detectors offer energy resolutions that are superior to other radiation detectors in addition to small size and fast timing characteristics. A big drawback is that they are degraded by radiation-induced damage during normal use. [Knoll, 2010, chap. 11]

Charged particles passing through a semiconductor detector create electron-hole pairs along the particles path. By setting up an electric potential across the diode, there will be an electric field present that will cause the holes to drift in the same direction as the electric field vector, and the electrons in the opposite direction. By monitoring one of the diodes sides, a pulse is measured as the charge from either the holes or the electrons (depending on which side is measured) is collected.

A semiconductor detector, like other diodes, can be forward biased or reverse biased. It is possible to operate a semiconductor detector without external bias, but it will perform poorly as the electric field across the junction will be too weak to read out the charge carriers before many are lost. Applying forward bias to the detector reduces the electric field even further, while reverse bias increases it. Another important factor is that reverse bias increases the depletion region, which is also the active volume of the detector. A PIN diode with its large active volume is therefore very useful as a radiation detector. [Knoll, 2010, chap. 11]

3.3 Semiconductor Characterization

3.3.1 Capacitance-Voltage Measurements

Capacitance-Voltage (C-V) profiling is a semiconductor characterisation technique that is much used to find doping- and defect densities in semiconductor junctions. The technique relies on the fact that the width of a reverse biased depletion region depends on the applied voltage. The small signal capacitance is dependent on both the doping density and width of the depletion region. C-V profiles are made by measuring the capacitance while sweeping over a voltage range. The doping density is found from the slope of a C-V curve or a $1/C^2$ -V curve. [Schroder, 2005, chap. 2]

There are multiple ways to measure capacitance. A simple method is to supply a known current, and measure how fast the voltage across the capacitor rises. This method assumes an ideal capacitor, and is therefore inaccurate for a real capacitor. A more accurate method is to supply an AC signal to the device under test and measure the AC current and voltage. A high frequency signal (~ 10 MHz) will be better for measuring dynamic performance, while a low frequency signal (~ 10 kHz) is better to find quasistatic characteristics. The capacitance is calculated from the frequency, current, and voltage.

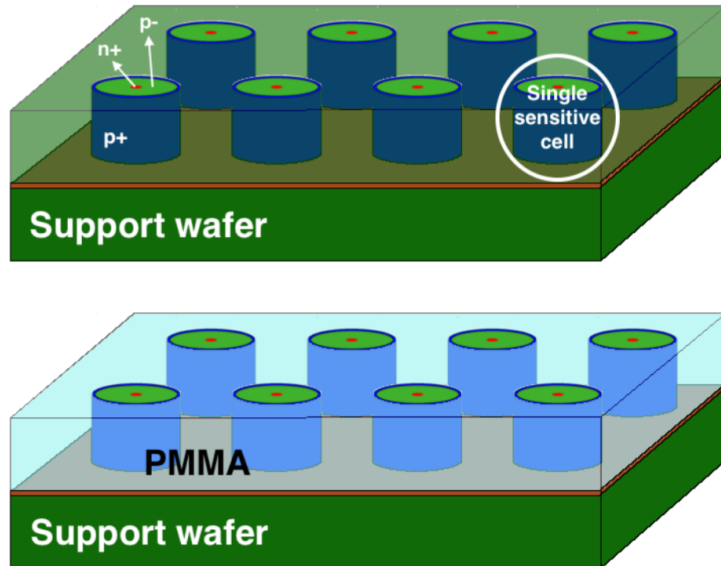


Figure 3.3: Presentation sketches of the 3DMiMic detector, shown without and with PMMA (tissue equivalent plastic). [Povoli et al., 2015]

3.3.2 Current-Voltage Measurements

Current-Voltage (I-V) characterization is observation of the current through a device when sweeping over the voltage across it. This can be used to find basic electrical parameters for the device. This includes leakage current, resistance, cut-in (threshold) voltage, breakdown voltage, saturation voltage, and hysteresis.

3.4 3DMiMic

Si-3DMiMic, or simply 3DMiMic, is a silicon-based 3D mini and micro-dosimeter being developed by SINTEF MiNaLab in Oslo, but was invented and ordered by Professor Anatoly Rozenfeld from the Centre for Medical Radiation Physics at the University of Wollongong. The detector is made to mimic the response of biological tissues to ionizing radiation on a cellular and sub-cellular level, and consists of an array of more than a thousand cylindrical p-i-n diodes (see figure 3.3). This is in an attempt to get a better estimate of the Relative Biologic Effectiveness (RBE) (section 2.2.3) by observing the microscopic distribution of the dose. Each diode, or cell, is made of a thin n+ core cylinder, a circular p+ trench some micrometers out, and in some cases a n+ guard ring further away from the core (see figure 3.4). There are multiple versions of the detectors, with differences including presence of n+ guard ring, size of cell, and structure. The silicon between the different cells should be etched away and replaced with tissue equivalent polymethyl methacrylate (PMMA), but this has not been attempted by

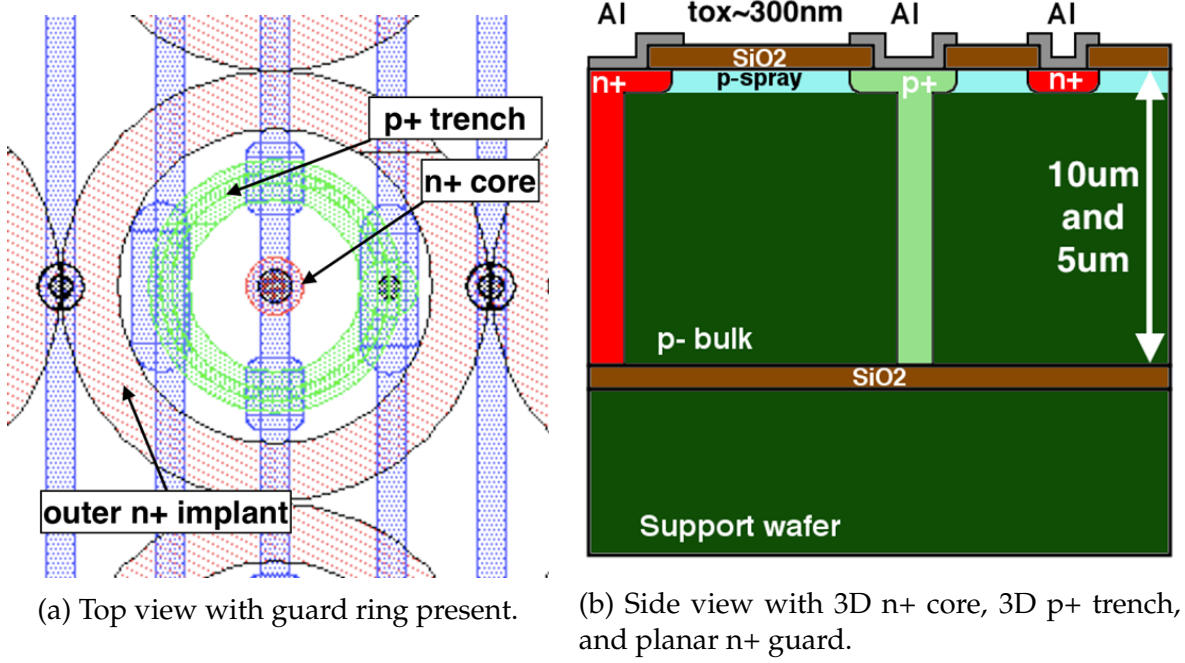


Figure 3.4: Layout of a 3DMiMic cell. [Povoli, 2016]

SINTEF yet as of the time this thesis is written. This should be done because PMMA produces secondary radiation in a very similar way to how tissue does, unlike silicon, due to the mass numbers of the atoms.

Figure 3.4b show a "3D" layout with the n+ core cylinder and the p+ trench going all the way through the bulk, and a planar n+ guard ring. There also exist designs with either or both the n+ core and p+ trench made planar. There are designs with cells in two different sizes, seen in figure A.2. The radii of the p+ trench circles are roughly 15 and 20 μm for the two designs. The detectors with the smaller diodes have 50x50 cells, while the larger variant has 32x33 or 33x33 cells depending on the layout. Images of some of the different layouts can be found in Appendix A.

In the main layout of 3DMiMic, all the n+ cores in a line is connected together. Every second line is also connected, leaving two channels (odd/even) for readout. When present, all the outer n+ rings are connected and can be read out if desired. A full die is shown in figure 3.5, where the "+" pads are the n+ cores, the "G" pads are for the p+ trenches, the "GUARD" pads are for the cell guard rings, and the large square around the detector is a guard ring. There also exist other layouts, for example with all diodes connected together, readout in eight channels, and a larger design made to be bump bonded to a Medipix chip (see section 4.2.1).

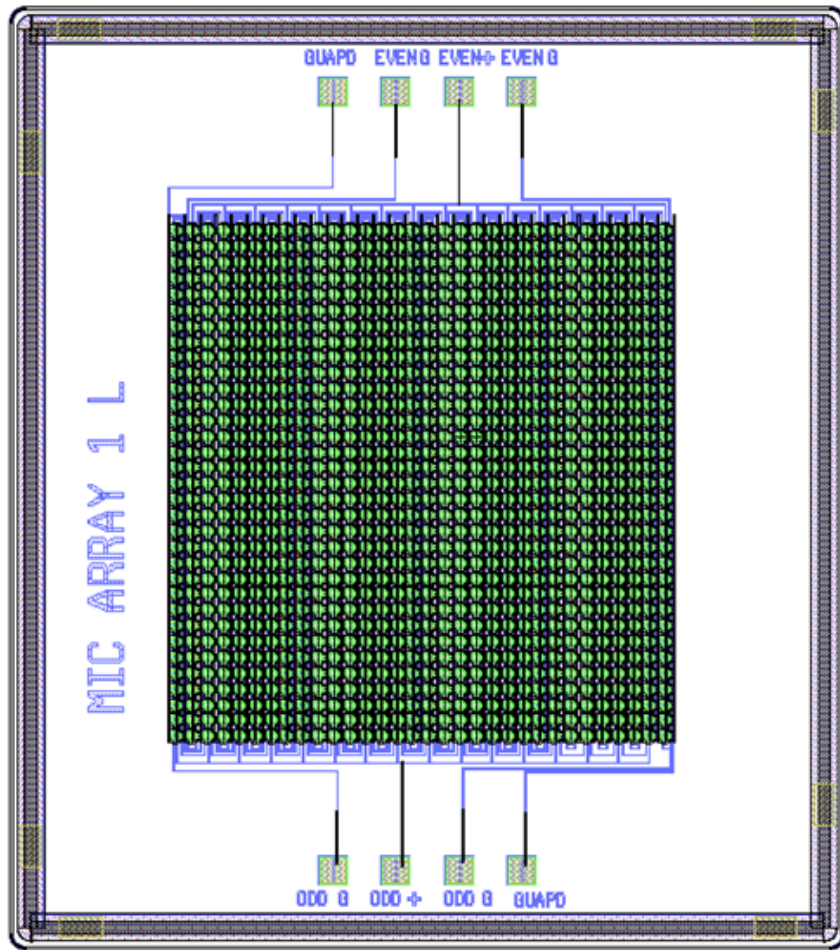


Figure 3.5: Layout of a full 3DMiMic die, showing bonding pads and the guard ring outside the active area. [Povoli, 2016]

Even though the odd/even readout scheme contains two channels, it does not provide any spacial information, as both channels cover the whole active area of the detector. The reason for this layout is to notice if a particle track goes through multiple adjacent cells. If both readout channels are triggered at the same time, this was not a single event, as it will look if all cells are read in a single channel.

3.4.1 3DMiMic Response to Radiation

Table 3.1 show the expected signal strength from the 3DMiMic detectors to a Minimum Ionizing Particle (MIP), a proton in the Bragg peak, and a carbon ion in the Bragg peak. The proton and carbon numbers are from Geant4 simulations done by Andreas Samnøy. The MIP numbers are calculated from the minimum stopping power for a proton in silicon. The table also show safety margins that are a bit higher than the expected signal. The electronics should be able to read out signals of at least the safety margins in case of simulation inaccuracies. The radiation will also deposit slightly more energy if they pass through the detector volume diagonally.

Table 3.1: Simulated response from some types of radiation. [Samnøy, 2016]

Radiation	Deposited energy		
	[keV]	[fC]	[e-]
MIP	3.87	0.172	1075
Proton in Bragg <i>(with safety margin)</i>	680	30	189k
Carbon in Bragg <i>(with safety margin)</i>	1080	48	300k
Carbon in Bragg	12000	533	3.3M
<i>(with safety margin)</i>	14400	640	4M

Table 3.1 sets the requirements for the readout electronics' dynamic range to between 1000 and 4 million electrons, which is equivalent to a range of 4000:1. A range this long can be very difficult to get without sacrificing too much of the other properties of the electronics. One possible method of reducing the required dynamic range is to exploit the odd / even readout scheme. The dynamic range can be split in two, one range for each readout channel. Then half the pixels can be used to read the smallest particles, and the other half can read the largest particles.

3.5 I-V Measurements of 3DMiMic Detectors on Wafer

I-V measurements of seven 3DMiMic wafers where performed in the cleanroom at SINTEF MiNaLab in Oslo by Øyvind Lye and Andreas Tefre Samnøy in May 2016. The equipment setup is shown in figure 3.6. These seven wafers have been produced

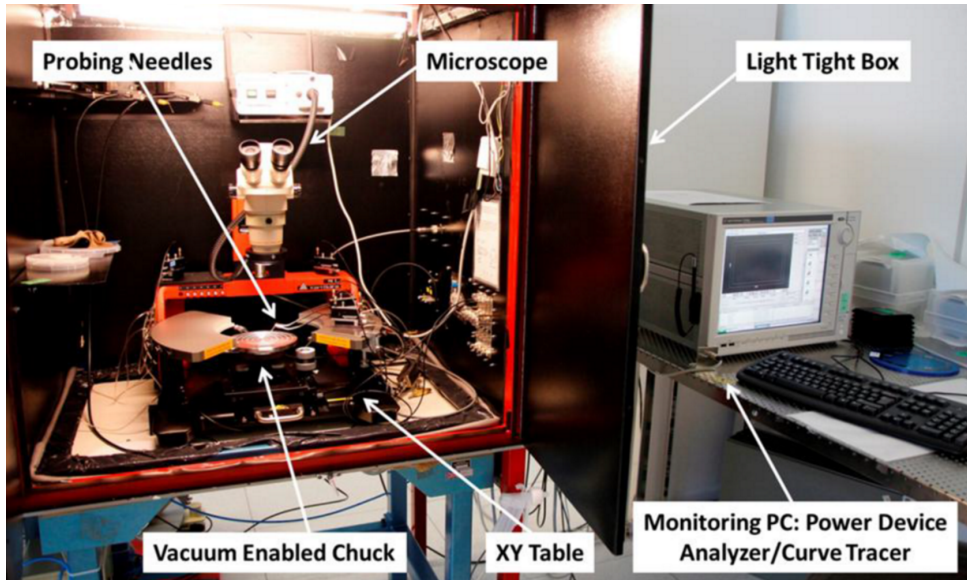


Figure 3.6: Equipment setup for I-V measurements at SINTEF. [Bansal, 2015]

with different designs and fabrication processes, see appendix A. Each wafer has 104 detectors with odd/even readout, 6 detectors with single channel readout, and several other experimental layouts. The detectors had to be tested with manual needle placement, as the designs are too different to use an automatic system with a probe card. The wafer is held in place on a stand using vacuum, and the stand can be moved in the horizontal plane. The needles can be manually placed at the desired location, and the position can be fine-tuned in Cartesian space using screws. The cell n+ guard ring was not connected on the detectors where it is present. This was done because it would require a separate test setup for the detectors with the ring, which would increase the time needed for the measurement. A total of 580 detectors were measured.

All measurements can be seen in appendix B. As an example, figure 3.7 shows the measurements from all the measured detectors on wafer S10-17. This clearly shows the huge differences between the detectors. This is also partly because there are multiple different layouts on one wafer, but figure 3.8 also shows large differences between the detectors of one layout. This is not very surprising, as the 3DMiMic detectors are made of very small, complex structures. Small variations in the production process, for example etching acting at different speeds on different parts of the wafer, can make a huge impact, especially if contacts to multiple pixels are broken. It would be interesting to test the number of dead pixels on the detector. This has previously been done at UiB by scanning a detector with a laser while moving the detector with an XY table. The laser point must be precise enough to not hit two pixels at once, and the XY table must be able to perform steps smaller than the distance between two pixels.

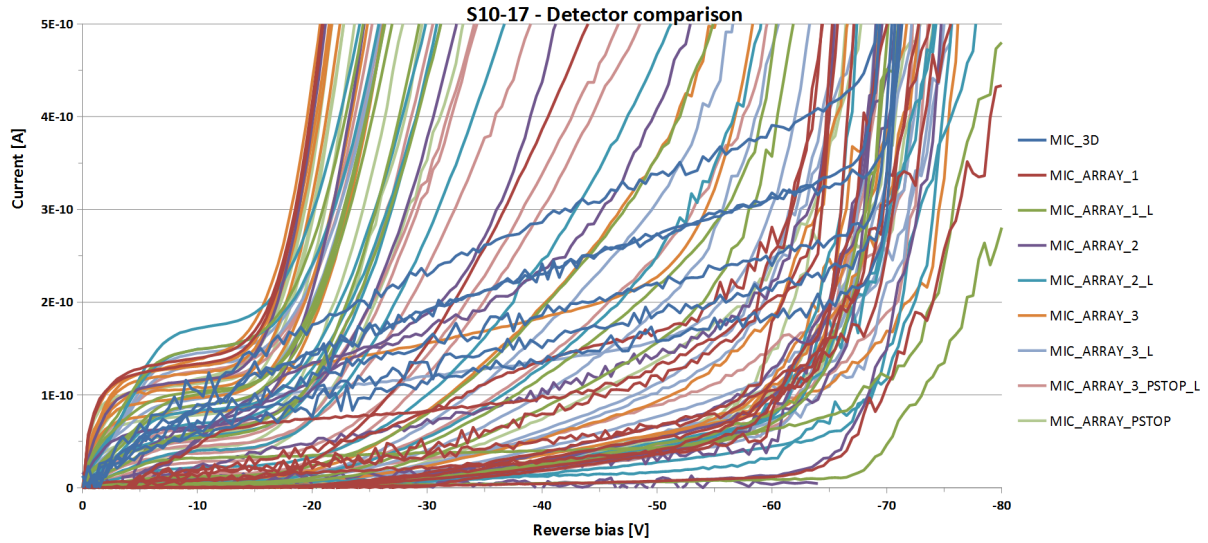


Figure 3.7: I-V measurement of the S10-17 wafer.

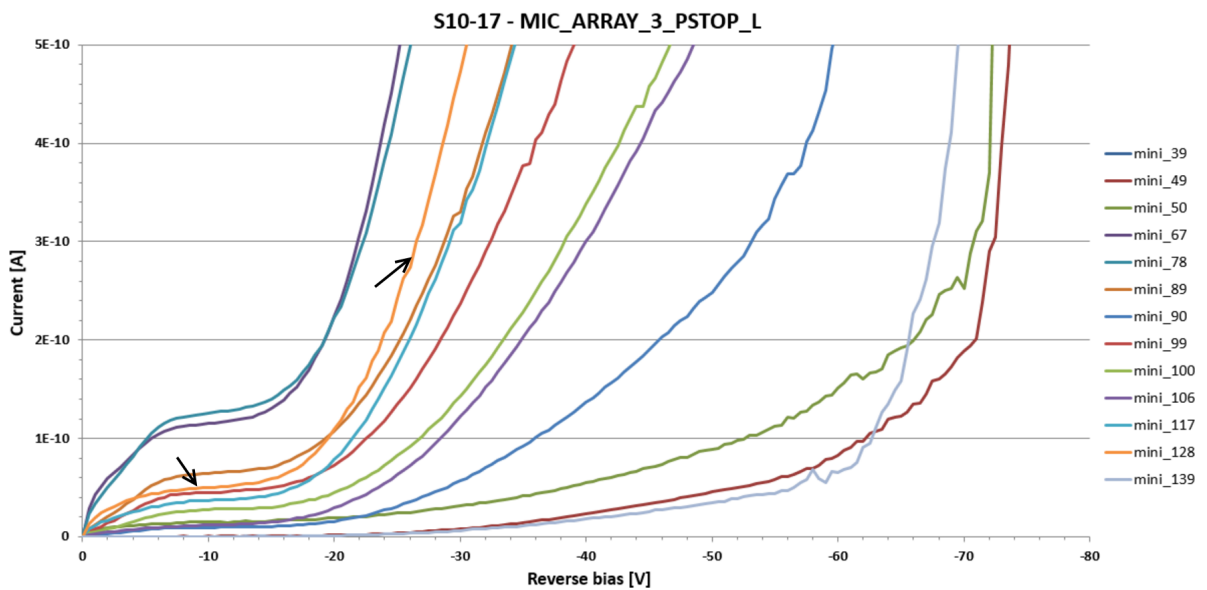


Figure 3.8: I-V measurement of the S10-17 MIC_ARRAY_3_PSTOP_L detectors. S10-17 #128 marked with arrows.

In general, wafers S10-1, S10-2, S10-11, S10-16 break down very early. S10-16 has a few good looking plateaus, but most of them are at very high currents. S10-15 currents increase rapidly and do not saturate. S10-14 also lacks the plateau curves. S10-4 has many relatively nice curves, but also many that rise too rapidly. S10-17 has the most curves with a nice saturation plateau at a not too high current. Which of the layouts that show the best characteristics varies a bit between the wafers, but MIC_ARRAY_3, 3_L, PSTOP, and 3_PSTOP_L seem to show the best characteristics. In general, MIC_ARRAY_1 and 2 seem to show the worst characteristics.

3.6 Detector Interface PCB

A Printed Circuit Board (PCB), see figure 3.9, was designed to interface 3DMiMic to the supply and readout electronics. This could have been very simple, but after discussions with Marco at SINTEF it was decided to make it as multi-purpose as possible with possibilities for quick reconnection for different setups. One of the main reasons for this was that the PCB was designed months before the detectors were finished. The PCB is described in detail in appendix C.

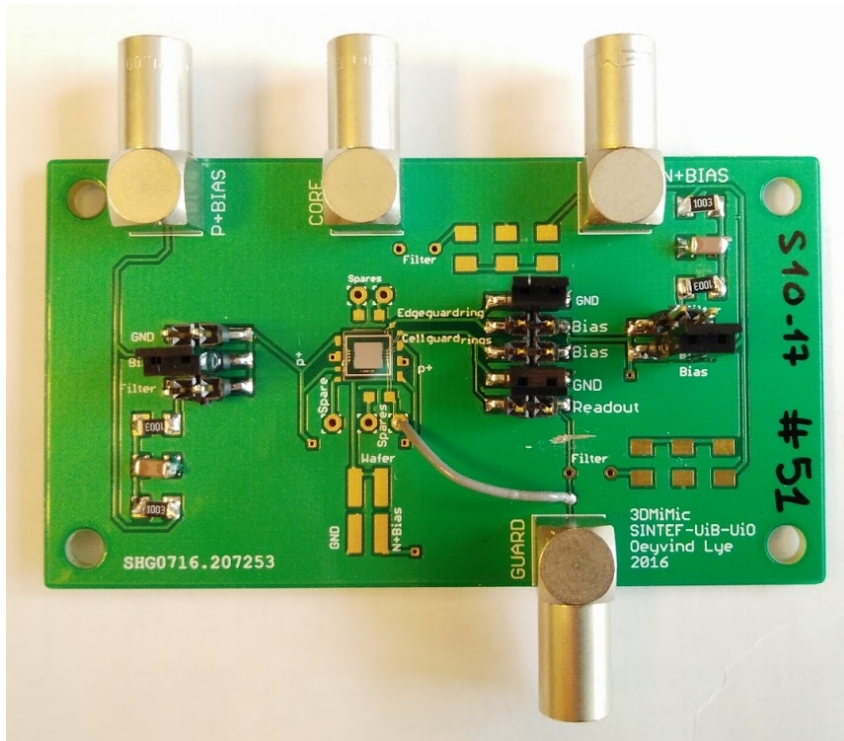


Figure 3.9: Photo of 3DMiMic detector on PCB.

3.7 Wire Bonding

Wire bonding the detectors to the PCB was supposed to be performed by SINTEF, but they had problems with the wire bonder in June 2016 which would have led to another delay. To avoid this delay, three detectors glued to PCBs were picked up at SINTEF and brought to the cleanroom at Vestfold Innovation Park for wire bonding. The wire bonder was already loaded with $17.5 \mu\text{m}$ gold wire, and this was used even though it is thinner than necessary for the 3DMiMic detectors. Each connection was done with two parallel wires for redundancy in case of mechanical damage to the thin wires. The three detectors are numbered: S10-15 #128 (MIC_ARRAY_3_PSTOP_L layout), S10-17 #51 (MIC_ARRAY_1 layout), and S10-17 #128 (MIC_ARRAY_3_PSTOP_L layout). See appendix A for the differences in the wafers and layouts, and appendix C for bonding schematics.

3.8 I-V Measurements of 3DMiMic Detectors on PCB

The I-V measurements in Bergen has been done with the Keithley 2635A sourcemeter, controlled by a LabVIEW program made by Enver Alagoz. The positive bias is set to the odd or even readout pin, while the p+ ring is connected to ground through the ground plane and the shielding of the bias wire. The exception to this is one measurement where ground is connected to the p+ ring with the separate p+ LEMO connector.

Both sides (odd/even) of the three detectors brought to Bergen have been repeatedly measured over a period of 1.5 months. The odd sides of both S10-17 #128 and S10-17 #51 appear to be short-circuited. Since the only measurements from SINTEF are the even sides of S10-17 #128 and S10-17 #51, it is unclear if the problem is on the detector, or on the PCB. For the S10-17 #51 it is considered likely that the wire bonding is the cause, as this is bonded according to figure C.5. The bond on the odd side is very long and difficult to perform. Microscope observations show that the bond is very close to, and possibly touching the edge of the detector. The S10-17 #51, which has guard rings for every pixel, was tested with guard rings disconnected and connected to ground. This showed no difference on the I-V measurements, so the rest of the measurements have been done with the guard rings connected to ground.

Figures 3.10 and 3.12 show the I-V measurements performed at UiB together with the corresponding measurements from SINTEF (dashed line). The S10-17 detectors show a large range where the current has saturated at a fairly low leakage current, see figure 3.11. The measurements do not fit perfectly with the SINTEF measurements

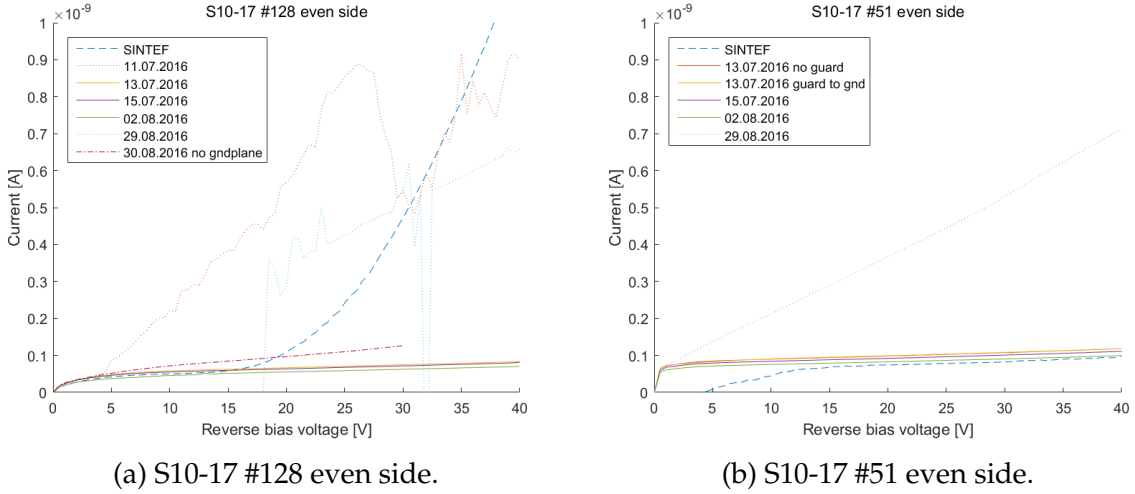


Figure 3.10: I-V measurements of S10-17 detectors on PCB.

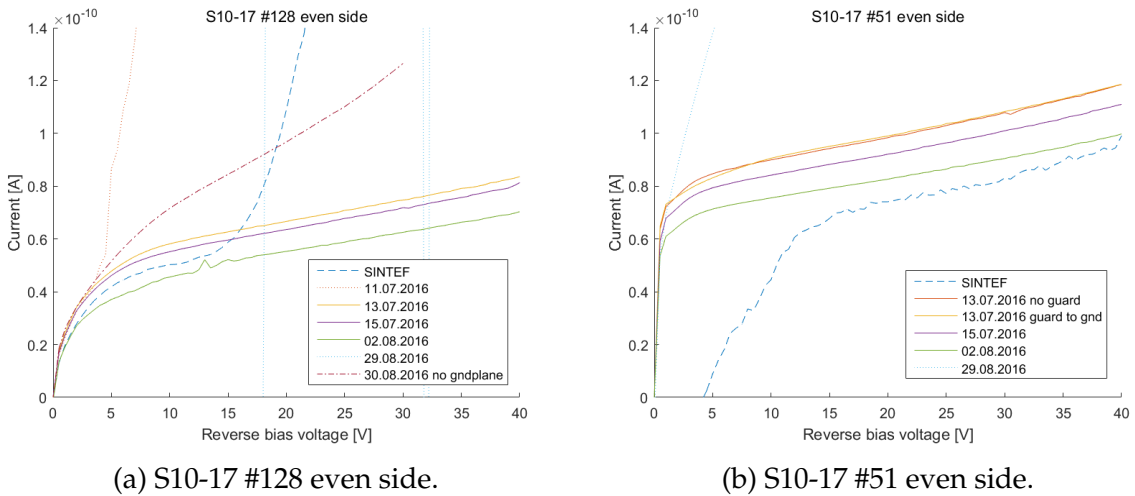


Figure 3.11: I-V measurements of S10-17 detectors on PCB. Zoom on flat area.

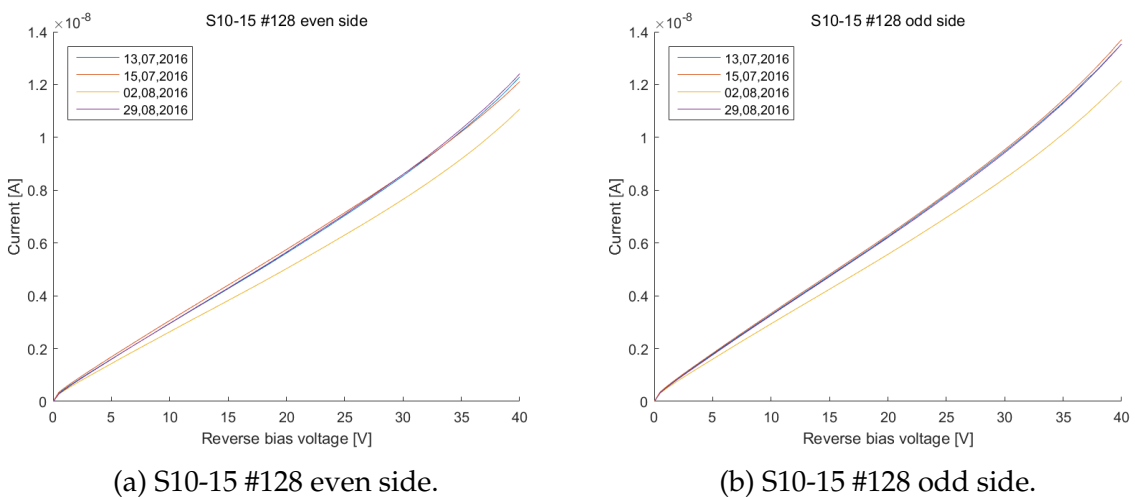


Figure 3.12: I-V measurements of S10-15 detectors on PCB.

however, because the S10-17 #128 went into breakdown much earlier at SINTEF, and the S10-17 #51 saturated much later. The reason behind this is unclear, as this should not be affected by the PCB. The slow saturation of the S10-17 #51 could be due to bad needle contact during the SINTEF measurement. There are also two UiB measurements for S10-17 #128, and one for S10-17 #51 (dotted line) that do not fit with the others. These have very strange behaviour, and is likely caused by equipment malfunction, for example bad cables can have a significant effect on currents as low as this. The S10-15 measurements are very consistent, but the current does not saturate, and is much higher than on the S10-17 detectors. The measurement performed with ground on a separate LEMO cable (dash-dotted line) does not fit with the SINTEF measurement, which is strange. All of the measurements show breakdown between 60 and 80 V (not shown in the figures).

3.9 C-V Measurements of 3DMiMic Detectors

C-V measurements have been performed in Bergen with the HP 4263B LCR meter and Keithley 2635A sourcemeter, controlled by a LabVIEW program made by Enver Alagoz. Ground is connected to p+ through a separate cable to the p+ connector.

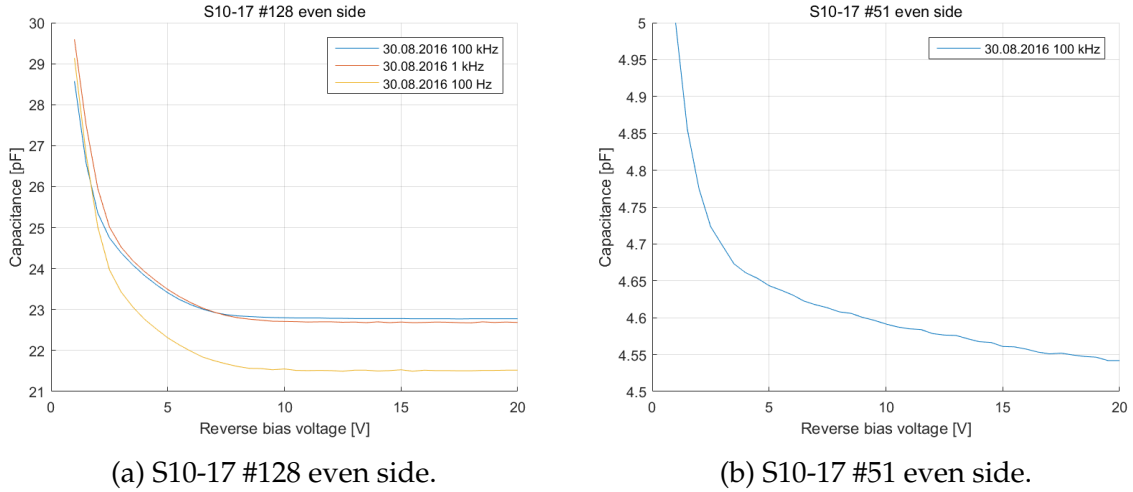


Figure 3.13: C-V measurements of S10-17 detectors on PCB.

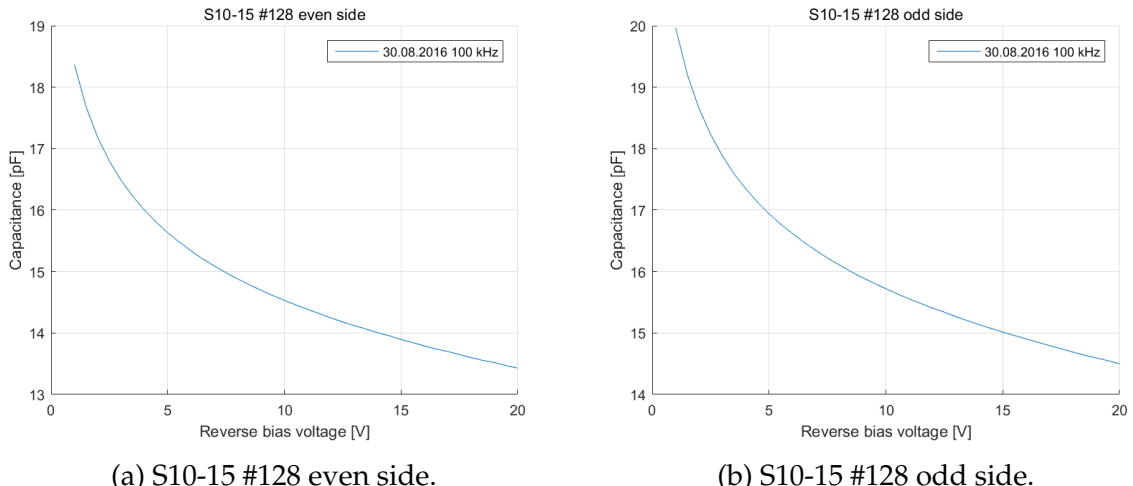


Figure 3.14: C-V measurements of S10-15 detectors on PCB.

The expected capacitance value from simulations from UOW was about 20 to 30 pF for the detectors with large pixels. These measurements therefore show very good results, with the highest value of less than 23 pF at 10 V. Assuming every pixel is connected and no capacitance from wires etc., the capacitance per pixel is 21 fF, 2 fF, 14 fF, and 15 fF at 10 V for the four detectors in the order they are shown in the figures.

3.10 Radiation Measurements with Americium source

A few radiation measurements have been performed in Bergen with an Americium-241 source after the detectors were received. Am-241 has a half-life of 432.2 years, and decays by releasing an alpha (helium-4 nucleus) and a photon. The alpha energy is 5.486 MeV 85 % of the time, 5.443 MeV 13 % of the time, and 5.388 MeV 2 % of the time. The most common photon energy is 59.54 keV. [LU, 1994] The even sides of the detectors from section 3.8 have been tested and seem to be working. Figures 3.15 and 3.16 show measurements with the S10-17 #128 detectors. These were measured with 10 V bias voltage on the detectors, and the Americium source at two different distances from the detector in order to attenuate the beam before reaching the detector, giving two different spectrums. The detectors were read out with the Ortec 142A pre-amplifier and the Caen V1729A ADC. The 10 and 25 mm measurements were taken over roughly 38 and 72 hours respectively. The figures show that the histogram consists of two Gaussians. The second, lower (in counts) Gaussian is for the radiation particles that pass through the metal on top of the pixel before entering the detector volume. This is much lower in number of counts, because the metal covers only a small part of the active volume.

The deposited energy is higher for longer distance between the source and detector, because the increased distance causes the Bragg peak to be closer to the detector. In figure 3.15 the peak from the alpha particles passing through the metal is at higher energy because the metal slows the particles, causing the Bragg peak to move closer. After going through 2.5 cm of air, the alphas will have lost a lot of energy, which makes them loose a lot of energy when passing he aluminium layer. They therefore have little energy left to deposit in the sensitive volume. This is why the lower Gaussian is to the left of the main Gaussian in figure 3.16.

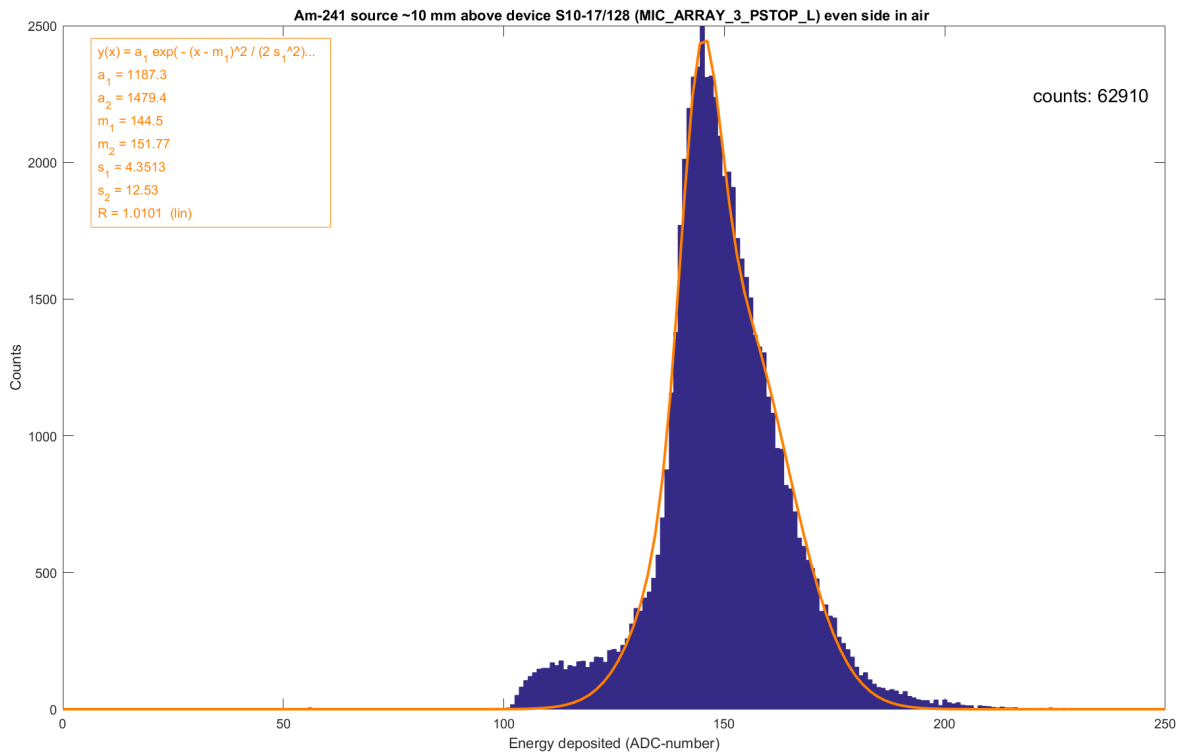


Figure 3.15: Am-241 radiation measurement at 10 mm distance.

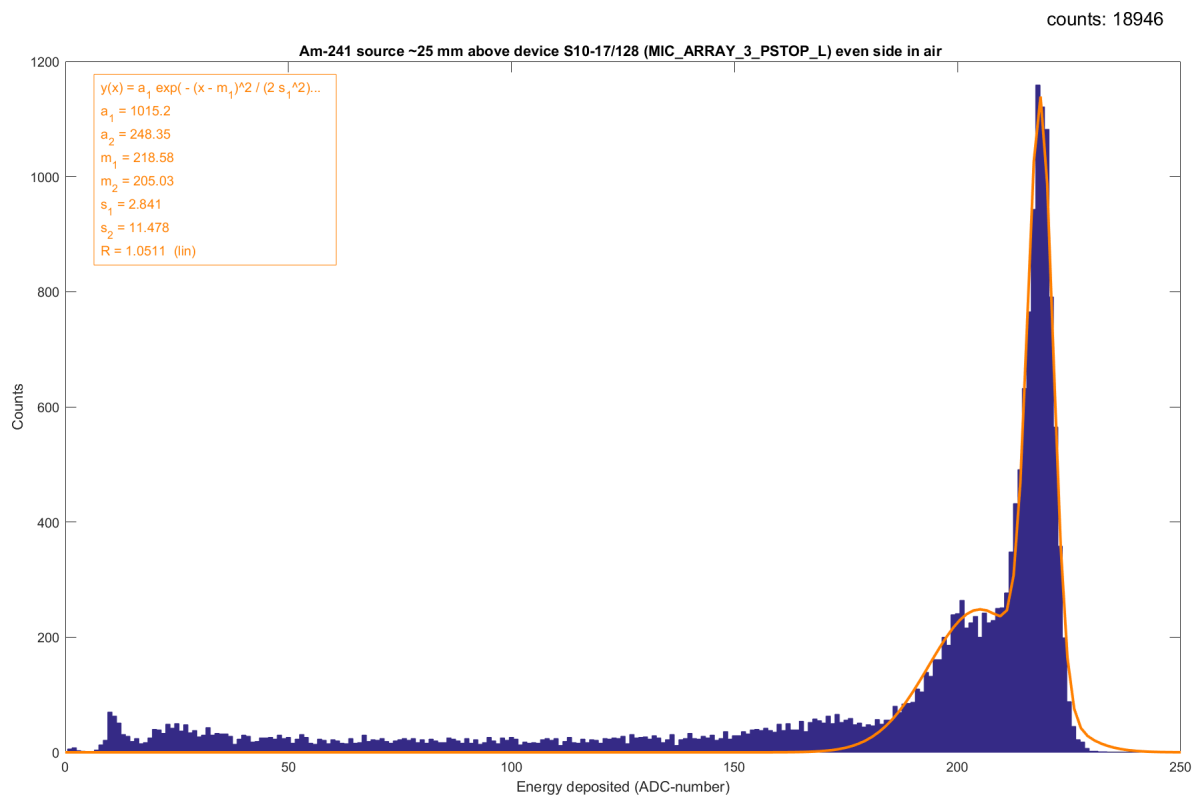


Figure 3.16: Am-241 radiation measurement at 25 mm distance.

Chapter 4: Readout Electronics for the 3DMiMic Detectors

4.1 Detector Readout

In different situations, the desired output from the detector readout will vary. In some cases, it is enough to simply count the radiation quanta, and in other cases one might want to read out an energy spectrum. In both cases the readout chain starts with a pre-amplifier that produces a voltage that is proportional to the radiation charge. The output from the pre-amplifier is sent to a shaping amplifier which converts the signal to a shape that is more suitable for the next component in the readout chain. This is to select the interesting pulses and convert the analog signal to a digital signal in one way or another. [Knoll, 2010, chap. 16]

4.1.1 Pre-Amplifier

For most radiation detectors, the liberated charge is too small to be processed, which is why pre-amplifiers are needed in most detector readout chains. The pre-amplifier is located close to the detector to reduce noise. A pre-amplifier can be voltage-sensitive or charge-sensitive. A voltage-sensitive pre-amplifier has an output signal proportional to the input voltage, which will be proportional to the input charge if the detector capacitance is constant. This is not the case for semiconductor detectors where the capacitance may change with the operating parameters. A charge-sensitive pre-amplifier (CSA) has an output signal that is independent of the input capacitance as long as the amplifier gain is high enough compared to a relationship between capacitances in the system. [Knoll, 2010, chap. 16]

One, often important, parameter to consider in a pre-amplifier is the dynamic range, which is the range of input signal amplitudes that can be reliably measured without changing the system. The lowest measurable input signal is limited by the noise in the system, mainly in the detector, detector cables, and pre-amplifier. A signal is not reliable if it is difficult to discern from the noise. The highest measurable input signal can be limited by the pre-amplifier or later stages, like the Analog-to-Digital Converter (ADC). If the pre-amplifier has a high gain, then a large input signal will require a

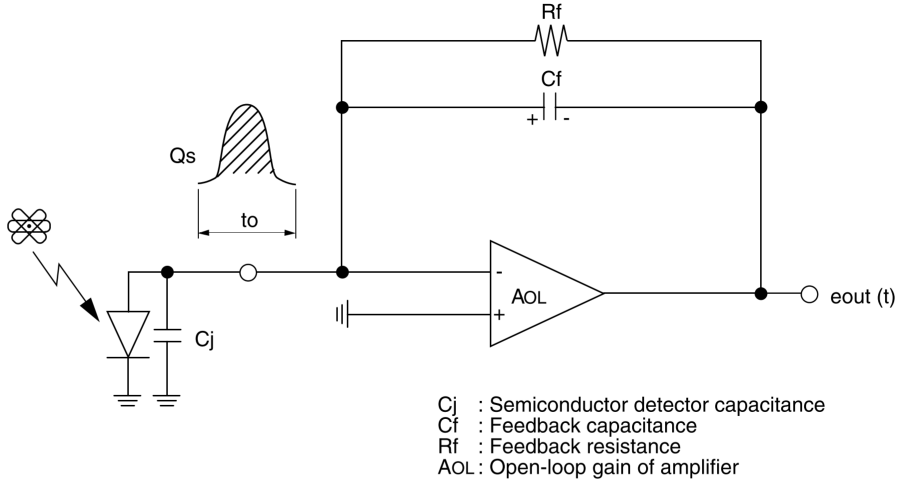


Figure 4.1: Schematic of a basic CSA. [Hamamatsu, 2001]

higher output signal than the pre-amplifier can deliver. If the gain is low, then another stage in the system will likely be the bottleneck before the pre-amplifier reaches its highest output level. [Halámek et al., 2001]

It is typically convenient to use the pre-amplifier to supply bias voltage to the detector. When this is done a single cable is used both to provide voltage to the detector and to transfer the signal pulses to the readout system. [Knoll, 2010, chap. 16]

Charge-sensitive amplifier operation

Figure 4.1 shows a general CSA. When a radiation quanta strikes the detector, a pulse of charge Q_s and width t_o is generated. This creates a rising potential on the negative input of the amplifier, which triggers a falling potential on the output of the amplifier. Because of the negative feedback, this will quickly draw the negative input close to zero, making it a point of virtual ground. The feedback currents charge the feedback capacitor, and then the capacitor is slowly discharged when there is no signal on the input. This creates a voltage pulse on the output that slowly falls from a peak value that is proportional to the input charge (figure 4.2). [Hamamatsu, 2001]

Since noise affects the resolution and dynamic range of a readout system, it is common to document the noise of an amplifier as *input referred noise*. This is the equivalent noise on the input of the amplifier that would create the noise that is seen on the output. This is done to more easily compare the noise to the expected signal strength at the input. For a charge-sensitive amplifier, it is then natural to refer to the noise as the Equivalent Noise Charge (ENC) on the input.

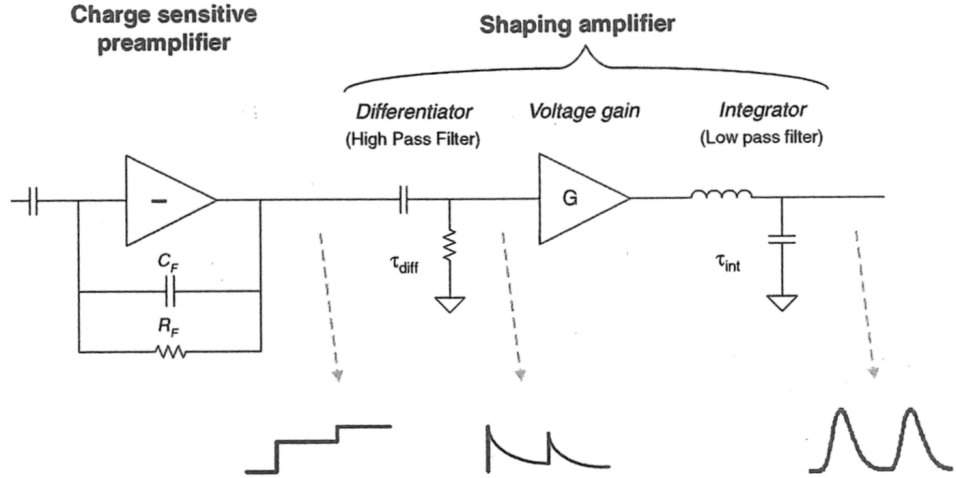


Figure 4.2: Schematic of simple charge sensitive pre-amplifier and shaper. Includes sketches of how the signal could look at different stages. [Knoll, 2010, chap. 16]

4.1.2 Shaper

The shaper, or shaping amplifier, converts the shape of the signal from the pre-amplifier to a form that is suitable for measurement. It is important that the output from the shaper quickly returns to the baseline to prevent pulse overlapping that will cause measurement errors. The first stage of a simple shaper, figure 4.2, is a differentiator (high pass filter) which passes the steep rise of the input pulse, but quickly returns to the baseline, and also reduces the noise. The differentiator decides the fall time of the pulse. The signal is then amplified to a level that is suitable for the ADC, before it is passed through the integrator (low pass filter) that filters away noise and increases the rise time of the pulse. This simple shaper is often called a CR-RC shaper, from the electronic components it is made from. [Knoll, 2010, chap. 16]

A much used parameter to describe a shaper is the shaping time, which is related to the duration of the shaped pulse. There is no standard for defining what shaping time is, but common practice is to use the (shaping) time constant ($\tau = RC$) of the filters, even though this does not clearly define all the time-related parameters. [Knoll, 2010, chap. 17] Since the shaping time constant is defined by the electronic components in the shaper, it is not possible to use this definition when measuring the shaping time of a shaper with unknown design. Therefore, in this thesis, the shaping time definition from [Ermis and Celiktas, 2012] is used. This is the time difference between the peak and 61 % of the peak value on the falling edge (figure 4.3).

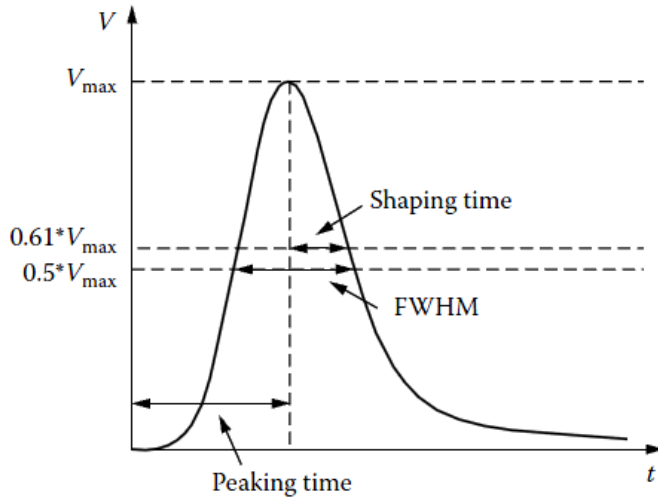


Figure 4.3: Definition of shaping time and peaking time. [Ermis and Celiktaş, 2012]

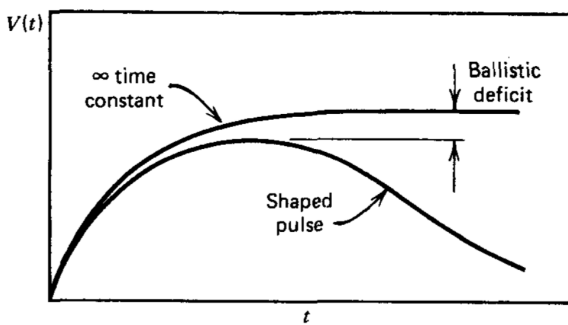


Figure 4.4: Definition of ballistic deficit. [Knoll, 2010]

There are many factors that come into play when deciding the shaping time. A short shaping time is needed to avoid subsequent pulses to overlap (pile-up), but a too short shaping time can lead to an error called ballistic deficit. This is when a too short shaping time compared to the rise time of the input pulse leads to a decrease in amplitude, see figure 4.4. When the shaping time is too short, not all of the charge will have had time to be collected, and the output pulse does not reach the full amplitude. The signal-to-noise ratio is also affected by both the shape and the shaping time. At short shaping times, the series noise component of the pre-amplifier dominates the total noise. The series noise is typically dominated by thermal noise in the first amplifying stage of the pre-amplifier. At long shaping times the parallel noise dominates. This could for example be detector leakage current, transistor leakage current, and thermal noise in the pre-amplifier feedback resistor. To total noise has a minimum where the series and parallel noise is equal, see figure 4.5. This is typically at 0.5 to 1 μs for semiconductor particle detectors. [ORTEC, 2009]

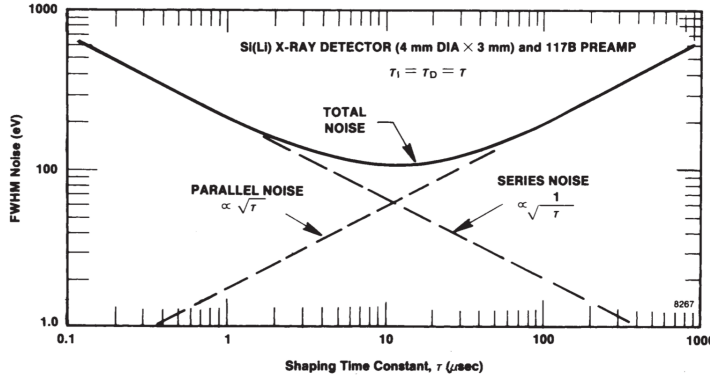


Figure 4.5: Noise versus shaping time. [ORTEC, 2009]

There are many other shaper configurations that can be used to create different shapes. One very popular choice is the CR-(RC)⁴ shaper, which uses fourth order low pass filter to make the pulse shape an almost perfect Gaussian. This type of shaper is therefore often called a semi-Gaussian shaper. A CR-(RC)⁴ shaper has about 18 % higher signal-to-noise ratio, and about 11 % lower deadtime than a CR-RC shaper. The fourth order filter can be implemented either by cascading four passive RC stages, or two active second order low pass filters. [ORTEC, 2009] [Knoll, 2010, chap. 17]

Most shapers include a pole-zero cancellation network (figure 4.6) to remove an undershoot that is often seen after the pulse. This makes it possible to have higher counting rates without problems with pile-up. Pole-zero cancellation is done with a potentiometer in parallel with the capacitor in the CR differentiator. The name comes from the poles and zeroes in the transfer function of the system. The network uses a zero to cancel out a pole in the complex plane. [ORTEC, 2009]

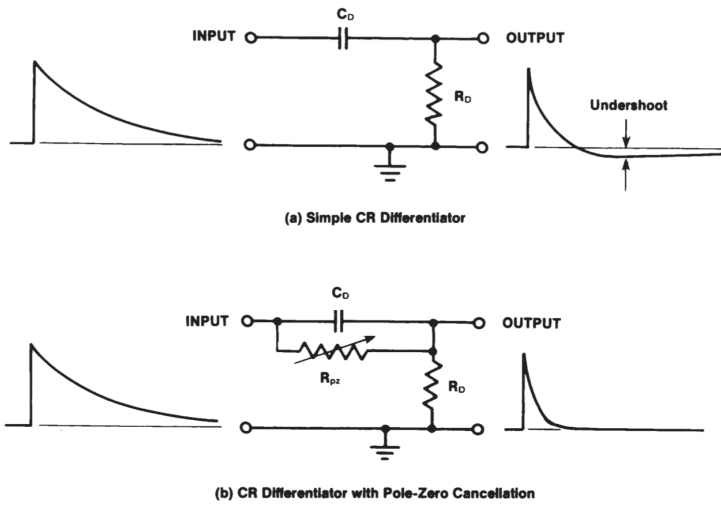


Figure 4.6: The benefit of Pole-Zero Cancellation. [ORTEC, 2009]

4.1.3 Analog-to-Digital Conversion

The analog signal from the shaper needs to be converted to a digital signal for processing and storage. When it is desired to keep as much information as possible, an Analog-to-Digital Converter (ADC) is used, but these use a lot of area and power. In situations where area, power, and cost is more important than accuracy of measurements (typically when there are a lot of channels), there are some simpler methods that can be used instead. The simplest is a counter, which merely counts the number of pulses with a height above a defined threshold. The information on the radiation quanta energy is lost, but the circuit is very simple. It is also possible to have multiple counters with different thresholds, which will keep some information about the distribution of radiation quanta energies. Another much used method is the Time over Threshold (ToT) technique. A ToT circuit measures the time that the pulse is over a defined threshold, and then this measurement can be used to estimate the height of the pulse. The relationship between pulse height and ToT is only linear within a certain range, and will usually limit the dynamic range of the readout system. [Iniewski, 2010, chap. 6]

An ADC samples the analog signal amplitude at a certain interval (sampling rate) and converts each sampled value to a digital signal. The resolution, which is the number of bits in the digital signal, will limit the accuracy of the conversion. The quantisation error is introduced as each analog value needs to be converted to the closest digital value. The maximum percentage quantisation error can be seen in equation 4.1, where n is the number of digits in the binary code and 2^n is the number of digital values. [Bentley, 2005, chap. 10]

$$e_q^{MAX} = \pm \frac{100}{2(2^n - 1)} \% \quad (4.1)$$

The dynamic range of an ADC will mainly be limited by its resolution, noise, linearity, and jitter (small timing errors). This can be summarized with effective number of bits (ENOB) to give a measure of the effective resolution, after noise and distortions. ENOB is defined as the resolution of an ideal ADC that would have the same effective resolution as the ADC in question.

4.2 Choice of Readout Electronics for the 3DMiMic Detectors

An overview of all readout electronics systems that was considered for use during this project can be found with relevant specifications in appendix D. The most promising systems are discussed and evaluated in this section.

4.2.1 Medipix and Timepix

Medipix is a family of chips developed to exploit technology from the experiments at CERN in other fields of science, mainly medical imaging. The chips made by the Medipix collaboration are; Medipix1, Medipix2, Timepix, Medipix3, Timepix3, and Dosepix. The Medipix 1-3 chips are made for photon counting and are therefore not useful for dosimetry. The Timepix chips are made to do ToT measurements, with Timepix and Timepix3 being based on Medipix2 and Medipix3 respectively. Dosepix is a currently in development chip made for photon dosimetry. They have extremely good noise properties, down to 60 e- of noise without a detector connected for Timepix3. Timepix3 and Dosepix were considered for the 3DMiMic project, but as ToT devices their dynamic range is not very large. Also, since they are made for photon detectors they cannot read the largest charges (table 3.1) that can be expected from the 3DMiMic detectors. [CERN]

4.2.2 UiO Portable Front-End Readout System

During the school year 2014-2015 two master students at UiO made a portable front-end readout system for radiation detectors [Tali, 2015] [Oltedal, 2015]. This system consists of two custom made cards and a Field-Programmable Gate Array (FPGA) evaluation board. The first card, the analog card, has three channels with pre-amplifiers while two of those channels also including shapers. The second card, the digital card, includes an ADC, comparators, and current monitors. The components of the digital card is connected to the FPGA on the SoCKit evaluation board by Arrow, which is connected to a computer through network. The system is made to detect fission fragments which produce very large signals, and therefore has a low gain. This makes the system too noisy for the low noise requirements of the 3DMiMic detector at the default gain, but this can be changed using external components.

4.2.3 IDEAS IDE1180 Amadeus Preamp-Shaper

IDE1180, or Amadeus, by Oslo-based IDEAS is a prototype Application-Specific Integrated Circuit (ASIC) for the front-end readout of radiation detectors. It features 16 channels of CSAs and shapers with adjustable shaping time. The preliminary datasheet [Maehlum et al., 2015] specifies a shaping time between 20 ns and 40 ns, negative and positive input charges up to 400 fC with lowest gain, and equivalent noise charge of 1106 e- plus 68 e- per pF load at default gain.

This chip was considered by multiple projects at IFT and a evaluation board (7045) was given to IFT so that more tests could be performed. Later, a second evaluation board (7048) was also received from IDEAS. The IDE1180 characterization is described in chapter 5.

4.2.4 Ortec 142A Pre-Amplifier

Ortec 142A is a single channel low-noise CSA optimized for charged particle or heavy-ion detectors. It was considered for the 3DMiMic project since UiB already owns a few of these. It features a very high dynamic range, up to 55 Me-, and an equivalent noise charge between 444 e- and 944 e- for detector capacitances between 0 pF and 100 pF. The University does not have a fitting portable shaping amplifier that can be used with the 142A, and it was therefore not prioritized for this project. The 142A is also well characterized and documented by Ortec. [ORTEC, 2011]

4.3 Portable PCIe ADC System

The current ADC system used at UiB is a Caen V1729A digitizer sitting in a VME crate. This features four 14 bit channels with 2 GS/s sampling rate, and 0.3 mV accuracy ($125 \mu\text{V}$ quantisation error and $175 \mu\text{V}$ noise), but is very large and heavy, making it cumbersome to bring for radiation tests. It was decided to purchase a new ADC for the department that could be put inside a small computer using Peripheral Component Interconnect Express (PCIe) to make a portable system. Three manufacturers that produced suitable ADCs for a reasonable price were found; AlazarTech, Keysight Technologies, and SP Devices. The considered models are listed in table 4.1.

The Keysight model was interesting with a signal interleaving feature where both 1.6 GS/s channels could be combined into one 3.2 GS/s channel. In the end SP Devices was chosen, being the only discovered company that produces 14 bit PCIe ADCs in the GS/s range. ADQ14AC-4C was chosen since having two extra channels was

Table 4.1: The analog-to-digital converters considered for purchase.

Manufacturer	Model	Channels	Resolution (bits)	Sampling (GS/s)
AlazarTech	ATS9360	2	12	1.8
Keysight	U5303A	2 (1)	12	1.6 (3.2)
SP Devices	ADQ14AC-2X	2	14	2
SP Devices	ADQ14AC-4C	4	14	1

considered more important than higher sampling rate for radiation tests, and the old Caen ADC can be used for projects and tests that require higher sampling rate.

4.3.1 SP Devices ADQ14AC-4C ADC

The SP Devices ADQ14AC-4C has a input range of $1.9 V_{pp}$ and has a variable DC offset of ± 1.05 V. It has an ENOB of 10.2, which gives an accuracy of 1.62 mV. This gives it worse accuracy and sampling rate then the Caen ADC.

A computer is needed to host the SP Devices ADC. The main requirement for the computer is that it is able to transfer data over PCIe close to the maximum data transfer rate of 3.2 GB/s specified in the ADQ14 datasheet. This puts requirements on the CPU, RAM, and motherboard. The CPU and motherboard needs to have eight available PCIe 2.0 lanes for the ADQ14. In addition, the CPU, chipset, and BIOS needs to support a PCIe payload size of 256 bytes.

A HP ProDesk 600 G2 with a micro-tower chassis has been purchased to be used with the new ADC. This has an Intel i7-6700 CPU, 64 GB of DDR4 RAM, a 256 GB SSD, and a 3 TB HDD.

Chapter 5: Characterization of IDE1180



Figure 5.1: Photo of IDE1180 evaluation board.

IDE1180, or Amadeus, by Oslo-based IDEAS is an early prototype integrated circuit for the front-end readout of radiation detectors. It features 16 channels of charge-sensitive pre-amplifiers and shapers with adjustable shaping time. Important specifications from the preliminary datasheet can be seen in table 5.1. The gain at default settings is specified as 12.45 mV/fC. Two chips, on evaluation boards 7045-1-03 (figure 5.1) and 7048-1-04 were characterized by the author, partly together with master student Sanjeeda Sharmin and chief engineer Thomas Poulianitis. The tests have been focused on the 7045 board as it showed the best characteristics, and the 7048 board is therefore only mentioned in section 5.11.

Table 5.1: Specifications from the IDE1180 datasheet [Maehlum et al., 2015].

Gain [mV/fC]	24/12/6/3 at different settings
Input range [fC]	0 to $\pm 50/100/200/400$
Maximum non-linearity	3 %
Equivalent Noise Charge (ENC) [e-]	1106 + 68 per pF load at default gain
Shaping time	20 to 40 ns
Maximum input event rate	5 MHz
Maximum power consumption	32 mW

The IDE1180 can be configured to different gains, shapes, etc. by setting different inputs on the ASIC. Some of these inputs are digital, and are set to either ground or

3.3 V. The rest are set by current inputs, which is done by setting a potentiometer, and connecting this to 3.3 V. The connections are done by adding jumpers to 3-pin pin-headers. The middle pin is connected to either the left side, ground, or the right side, 3.3 V. This is when looking at the PCB with the input on the left and the output on the right. No jumper should be equal to a ground connection. Using "1" and "0" to specify jumper positions can easily cause confusion, because the ground pins on the pin headers are marked with a "1" (pin 1) on the PCB. Therefore, "GND" and "3V3" is used to specify jumper positions in the tables in this chapter. An X is used for no jumper. The current in the potentiometers can be checked for future reference by connecting it to ground through a $10\text{ k}\Omega$ resistor using a GND jumper. The voltage across this resistor can be measured using a multimeter, and gives the current when divided by $10\text{ k}\Omega$.

5.1 Measurement Setups

The main measurement setup used for the characterization included the Caen V1729A ADC mentioned in section 4.3. This ADC has an input impedance of $50\ \Omega$, while the IDE1180 is configured to drive a load impedance of $1\text{ M}\Omega$. Therefore an in-house buffer was used between the IDE1180 and ADC. The in-house buffer cuts the signal at about 1.2 V which makes the ADC a bad choice for measurements that need to cover the entire dynamic range of IDE1180. By default, the IDE1180 has an output offset voltage of 0.5 V. Since the ADC has an input range from -1 V to +1 V, a 100 nF capacitor (DC block) was used to remove the offset. Some measurements used an oscilloscope instead of the ADC, which made the buffer and DC blocking capacitor unnecessary. Two different oscilloscopes have been used: Tektronix DPO 7254, and Agilent Infini-iVision MSO-X 3104A. The accuracy of the ADC is 0.3 mV. Both oscilloscopes have an effective resolution of 8 bit at the used sampling rates, which if the signal always covers minimum half the screen gives a quantisation error of maximum $0.78\% (\frac{100\%}{2^8/2})$.

A wave generator was used to simulate the pulse from a detector. This has been configured to a ramp with a long rise time and a fall time as short as possible. At first, Agilent 3325OA was used, but this generator was unable to produce a quick falling edge when a long rise time was used. The Tektronix AFG3252 wave generator was later used to obtain a rise time of 1 ms. Unless otherwise mentioned, the Tektronix wave generator has been used with a period of 1 ms. The wave generator is connected to the external calibrate input, where a test capacitance of 1 pF is present in series (see figure 5.4). The input charge to the pre-amplifier is then equal to 1 pF times the peak-to-peak voltage of the test pulse from the generator. The original $1\text{ pF} \pm 5\%$ capacitor

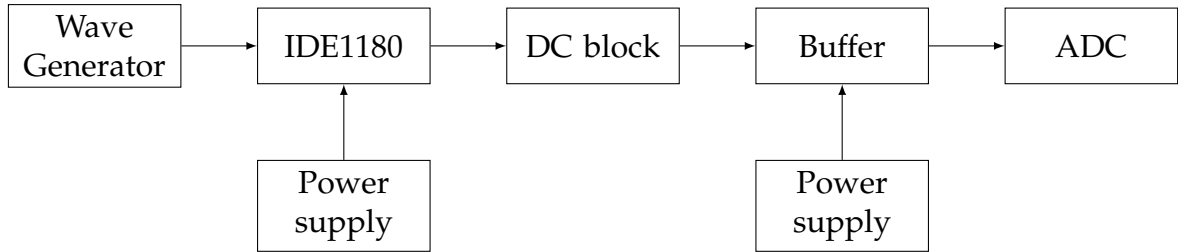


Figure 5.2: Measurement setup using the ADC.

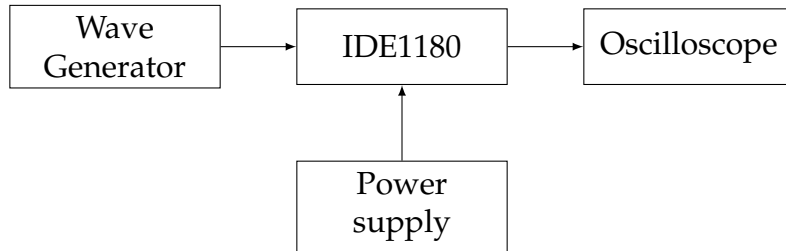


Figure 5.3: Measurement setup using an oscilloscope.

on the board was broken and replaced with a $1 \text{ pF} \pm 25\%$ on the 29.05.2016. The only measurements shown in this thesis with the original capacitor is those from table 5.4 to 5.3, table 5.9, and subsection 5.3.2. The rest are with the second capacitor. A third capacitor with $\pm 5\%$ was added on the 29.08.2016 to better estimate the values of the capacitors by comparing measurements with the exact same setup. This gave values of 1.02 pF , 0.95 pF , and $0.98 \text{ pF} \pm 0.02 \text{ pF}$ for the three capacitors. These values have been used for compensation in all the data of the thesis.

For many measurements it is required to vary the input load capacitance of the pre-amplifier, to simulate different detector capacitances. To make this possible, a mount was added that can be used to place through-hole capacitors, see figure 5.4. This connects the capacitor between the input of one channel and ground. A similar mount was made to connect an input to the output offset voltage.

The IDE1180 has been configured to six different shaping times: 40 ns (default), 100 ns, 300 ns, 500 ns, $1 \mu\text{s}$, and $2 \mu\text{s}$. The 100 ns and 300 ns settings have only been used to investigate the relationship between noise and shaping time. Table 5.2 shows the necessary parameters to configure the IDE1180 to these shaping times. 40 ns is the default shaping time, and therefore requires no jumpers. The voltages specify the potential that should be across the $10 \text{ k}\Omega$ resistor belonging to said signal, and can be measured when a GND jumper is in place. PZ_ENABLE enables the pole-zero cancellation on 3V3. PZ_BIAS_HI to 3V3 switches to high range of pole-zero time constant (low pole-zero resistance). SH_BIAS adjusts the shaper operation current. VFS_BIAS sets the

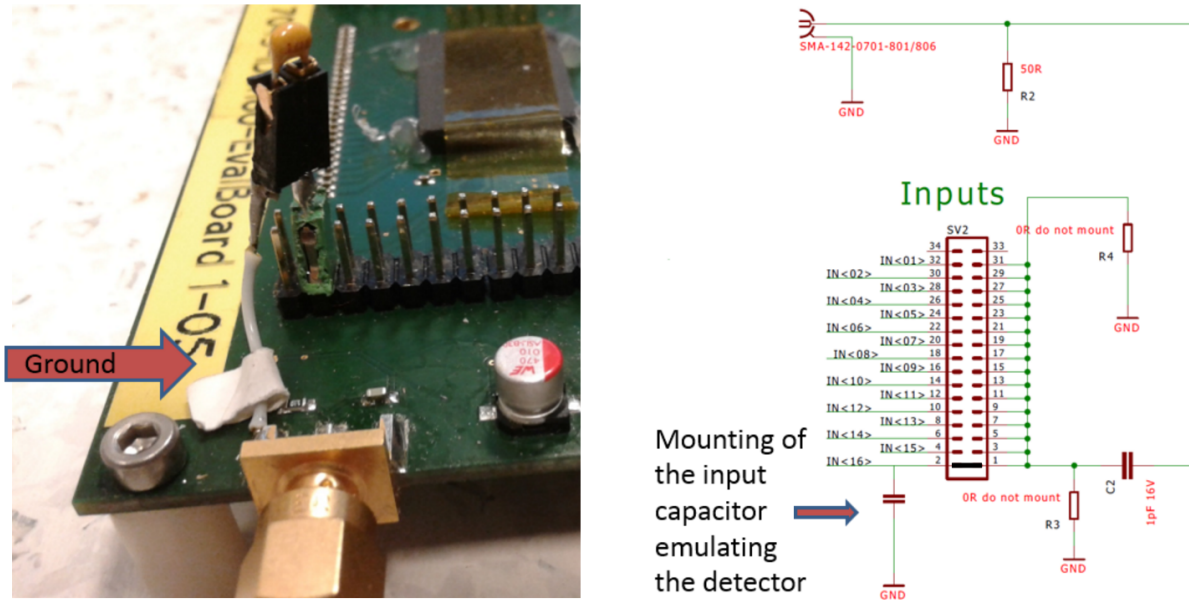


Figure 5.4: Image and schematic of capacitor mount. [Poulianitis, 2016] [Maehlum, 2015]

peaking time. PZ_BIAS adjusts the pole-zero time constant. SH_BIAS and VFS_BIAS must be enabled with 3V3 jumpers for settings to take effect, while for PZ_BIAS settings take effect for a GND jumper. Note that the other shaping times are outside the range the chip is designed to work in. It is therefore not expected that the chip will work as well at this configurations as for default shaping time.

Table 5.2: Configurations for different shaping times on IDE1180.

Shaping time	PZ_ENABLE	PZ_BIAS_HI	SH_BIAS	VFS_BIAS	PZ_BIAS
40 ns	X or GND	X or GND	X or GND	X or GND	X or GND
100 ns	3V3	X or GND	3V3, 144 mV	3V3, 132 mV	GND, 110 mV
300 ns	3V3	3V3	3V3, 308 mV	3V3, 81 mV	GND, 1790 mV
500 ns	3V3	3V3	3V3, 325 mV	3V3, 81 mV	GND, 500 mV
1 μ s	3V3	3V3	3V3, 350 mV	3V3, 92 mV	GND, 268 mV
2 μ s	3V3	3V3	3V3, 357 mV	3V3, 91 mV	GND, 109.5 mV

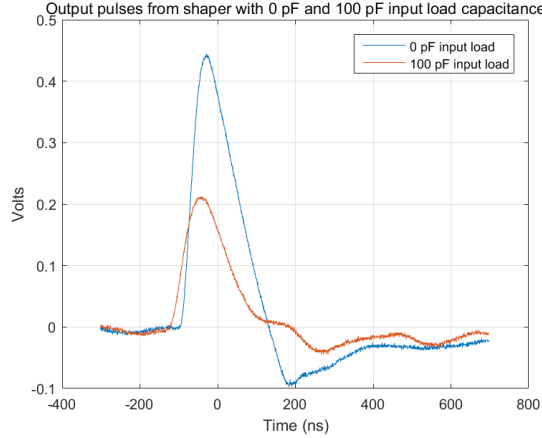


Figure 5.5: Pulses from IDE1180 with different input load capacitance.

5.2 Gain vs. Input Load Capacitance

During early measurements it quickly became evident that the output voltage from the IDE1180 is reduced when the input load capacitance is increased, see figure 5.5. This drop was at first not understood by the team. It was found to be caused by multiple effects, which are investigated in this section. Tables 5.3 to 5.6 show gain measurements with different gain settings, using different setups. The oscilloscope measurements were done by placing a cursor in the middle of the noise using the Tektronix oscilloscope. The ADC measurements are calculated from the mean of a gaussian fit to amplitude measurements done by the ADC. The measurements shown in these tables were done with an input ramp pulse with $1 \mu\text{s}$ period from the Agilent oscilloscope.

Table 5.3: Gain [mV/fC] vs. capacitance measured with ADC.

	PA_GAIN<1:0>	0pF	10pF	56pF	100pF
00	GND-GND	10.6	9.2	5.7	4.4

Table 5.4: Gain [mV/fC] vs. capacitance for different gain settings measured with oscilloscope without buffer connected.

	PA_GAIN<1:0>	0pF	10pF	56pF	100pF
00	GND-GND	11.2	9.9	6.5	5.0
01	GND-3V3	6.9	6.2	4.5	3.7
10	3V3-GND	4.2	4.0	3.3	2.9
11	3V3-3V3	2.3	2.2	2.0	1.7

Table 5.5: Gain [mV/fC] vs. capacitance for different gain settings measured with oscilloscope with buffer connected.

PA_GAIN<1:0>		0pF	10pF	56pF	100pF
00	GND-GND	10.0	8.4	5.3	4.2
01	GND-3V3	5.9	5.3	3.9	3.1
10	3V3-GND	3.5	3.4	2.8	2.5
11	3V3-3V3	2.0	1.9	1.6	1.4

Table 5.6: Gain [mV/fC] vs. capacitance for different gain settings measured with oscilloscope without buffer connected. Input load capacitor connected to V_{offset} instead of ground.

PA_GAIN<1:0>		0pF	56pF	100pF
00	GND-GND	10.7	6.1	4.6
01	GND-3V3	6.6	4.3	3.7
10	3V3-GND	3.9	3.1	2.7
11	3V3-3V3	2.2	1.8	1.6

As the ADC measurements takes the maximum peak signal, while the oscilloscope measurements are done with cursors in the center of the peak noise, it was expected that the table 5.3 values were slightly higher than the table 5.5 values. The values in table 5.5 are 10 to 20 % lower than those in table 5.4, showing that the in-house buffer does not perfectly pass the signal. This could be caused by gain lower than one, bandwidth limitations, or impedance problems. It should also be noted that the measured gains at 0 pF are very different from the gains of 24/12/6/3 mV/fC that are noted in the datasheet [Maehlum et al., 2015].

Figure 5.6 shows how the gain falls off for the different shaping times. This is measured using the Agilent oscilloscope, with the IDE1180 inside a Faraday cage. The drop becomes less and less distinct as the shaping time is increased, and at 2 μ s the gain vs. capacitance curve is fairly flat. It is possible to increase the gain of the IDE1180 by 50 % with the BUF_GAIN_HI setting. This can for example be useful when using the IDE1180 with long shaping times where the gain is very low.

One possible explanation for the gain drop could be leakage current from the capacitor. Since a large capacitance causes the rise time of the pulse to be very slow, it is possible that the leakage causes the pulse never being able to reach proper maximum value.

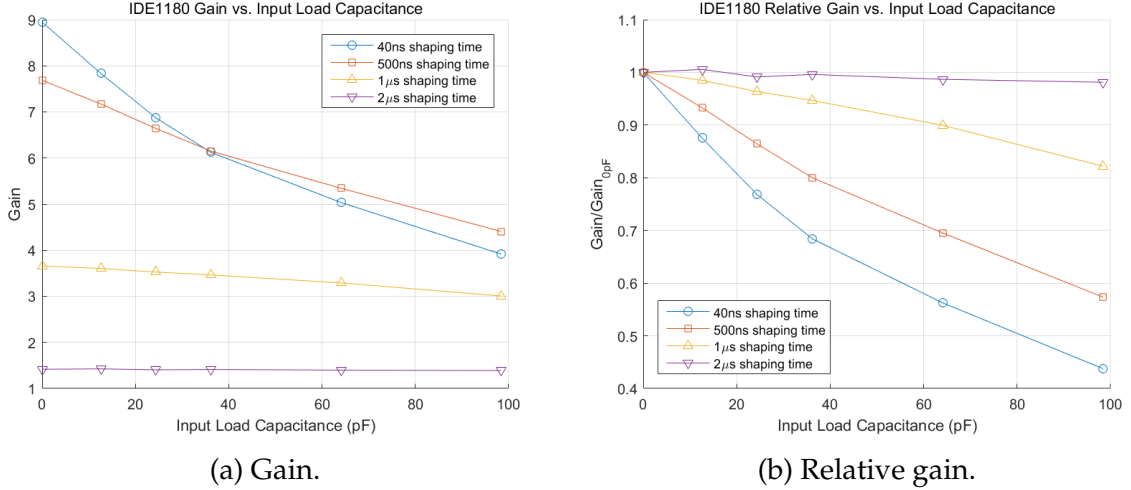


Figure 5.6: Gain and relative gain vs. capacitance at different shaping times.

Faraday cage load issue

Note that the default shaping time curve in figure 5.6 does not fit well with the data in the tables in this section. This was first assumed to be due to the differences in the two 1 pF test capacitors and the imperfect gain of the buffer, but after the 1 pF was compensated for it became obvious that this was not the only contributor. The real main reason was very late discovered to be the line capacitance of the Faraday cage and the cables on the output, see figure 5.7. The IDE1180 is made to drive a line capacitance of nominally 4 pF and maximum 20 pF [Maehlum et al., 2015]. The extra capacitance from the box and extra cables causes the pulse height to drop and the pulse fall time to increase. It was attempted to counter this by tuning the BUF_BIAS input, which is the output buffer operation current, but this only caused the opposite effect by increasing the fall time and reducing the peak height.

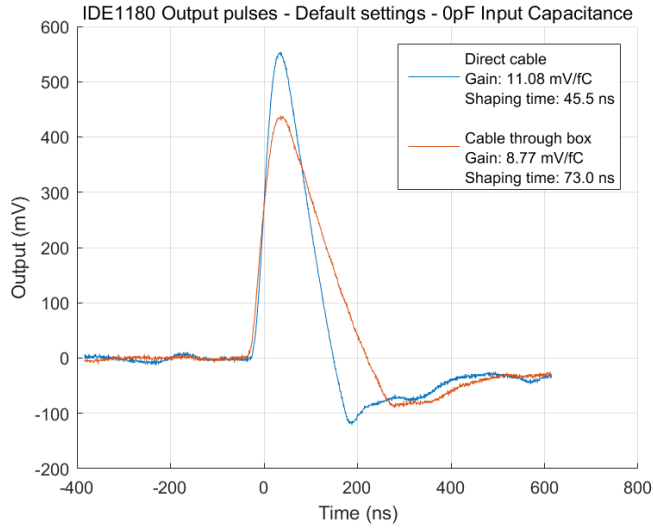


Figure 5.7: Pulses from IDE1180 with (blue) a direct cable from IDE1180 to Agilent oscilloscope, and (red) with first a cable to a connector on the Faraday cage and a cable on the other side to the oscilloscope.

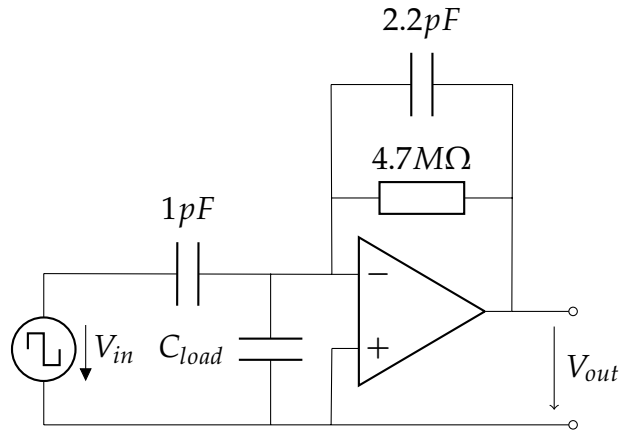


Figure 5.8: Schematic of simulated circuit.

5.2.1 Gain vs. Capacitance Simulations

To investigate the behaviour of a pre-amplifier being loaded with an input capacitance, a pre-amplifier was simulated in LTspice IV. One of the pre-amplifiers from [Tali, 2015] was simulated (figure 5.8), as the specifications of the IDE1180 pre-amplifier are unavailable. This was simulated both with an ideal operational amplifier (op-amp), and with the LT1122 that was tested in [Tali, 2015]. LT1122 is a fast settling amplifier with a good bandwidth, but is noisy and was therefore not used for the pre-amplifier in Tali's final design. The input signal for this simulation was a square wave of 2 ms period, 100 mV amplitude, and 10 ns edge times. Simulations were performed for C_{load} of 1 pF and 100 pF.

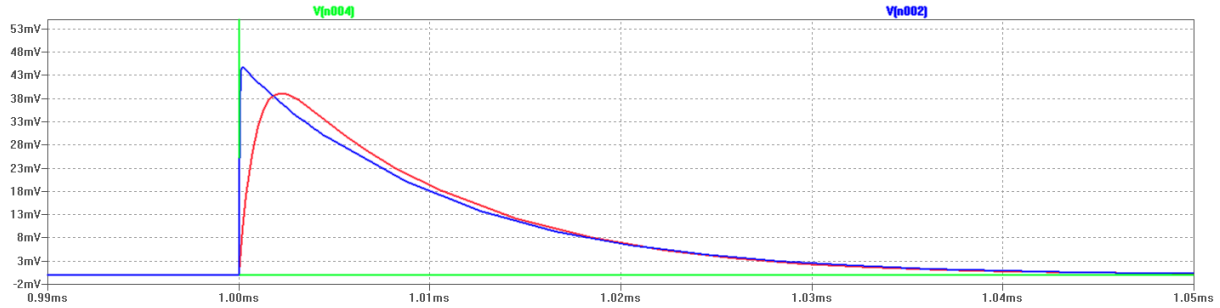


Figure 5.9: Simulation of ideal op-amp with 1 pF (blue) and 100 pF (red) load capacitance. Input pulse in green.

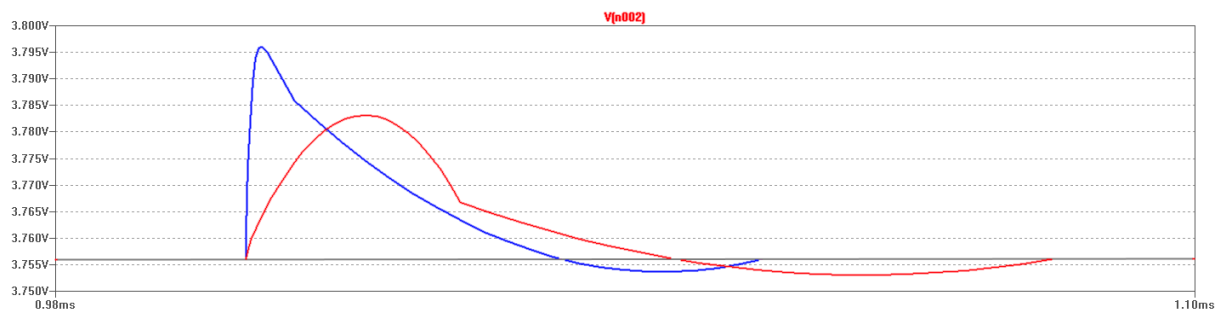


Figure 5.10: Simulation of LT1122 op-amp with 1 pF (blue) and 100 pF (red) load capacitance.

For the ideal op-amp, figure 5.9 shows a peak height drop of roughly 9 % and an increase in pulse area of about 1 % when the load capacitance is increased from 1 pF to 100 pF. Similarly for the LT1122, figure 5.10 shows a peak height drop of about 32 % and a pulse area increase of roughly 11 %. However, this pulse has a strange shape suggesting that some other effect is also taking place. Compared to the measured peak amplitude drops of almost 60 %, these simulations show that the drops should have been expected, but not in that magnitude. This has later been confirmed by figure 5.11 which shows an expected peak amplitude drop of about 10 % at 100 pF, calculated by IDEAS.

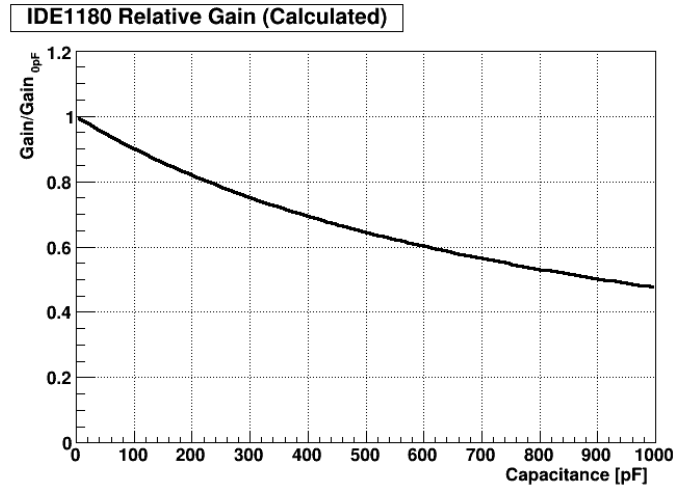


Figure 5.11: Calculated change in gain from increased input load capacitance. [Meier, 2016]

5.2.2 Ballistic deficit

Ballistic deficit (see section 4.1.2) is an error source that was investigated as a contributor to the drop in amplitude for high load capacitors. Figures 5.12 to 5.14 show measurements investigating the drop in gain by comparing the output signal from the IDE1180 when the shaper is connected and disconnected using the SH_ENABLE pin header. This is measured at default settings, using the Agilent oscilloscope, and the IDE1180 inside a Faraday cage. These data are based on only one curve saved from the oscilloscope, except for 100 pF with shaper disabled, where two curves were saved as the signal was very noisy. Therefore this data is not very accurate, but it is good enough for observing trends.

In figure 5.14a we see that even at 0 pF input load capacitance, the peaking time of the pulse from the pre-amplifier is 60 ns, which is longer than the shaping time of 40 ns. As the capacitance is increased, the peaking time is greatly increased, and we see the difference between the two curves in figure 5.12b increasing. This appears to be a ballistic deficit, but as gain reduction in the shaper from the increased capacitance is only about one fifth of the total gain reduction, ballistic deficit does not seem to be the main issue.

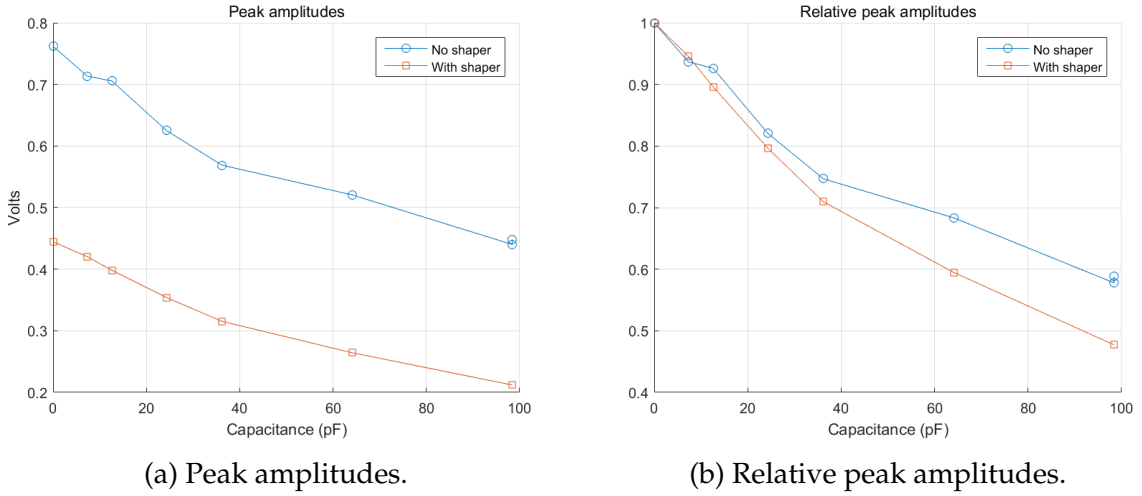


Figure 5.12: Amplitude comparison with and without shaper connected.

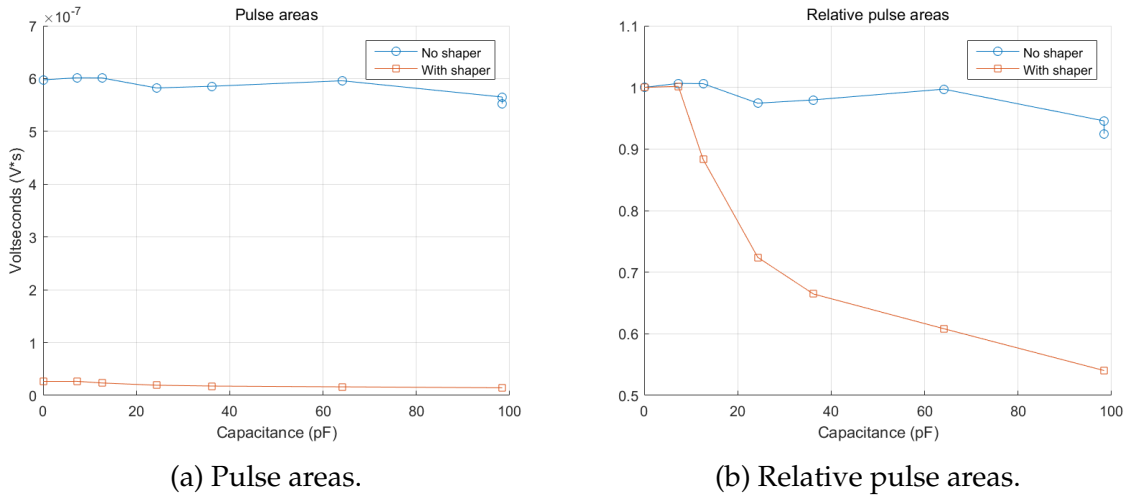


Figure 5.13: Area comparison with and without shaper connected.

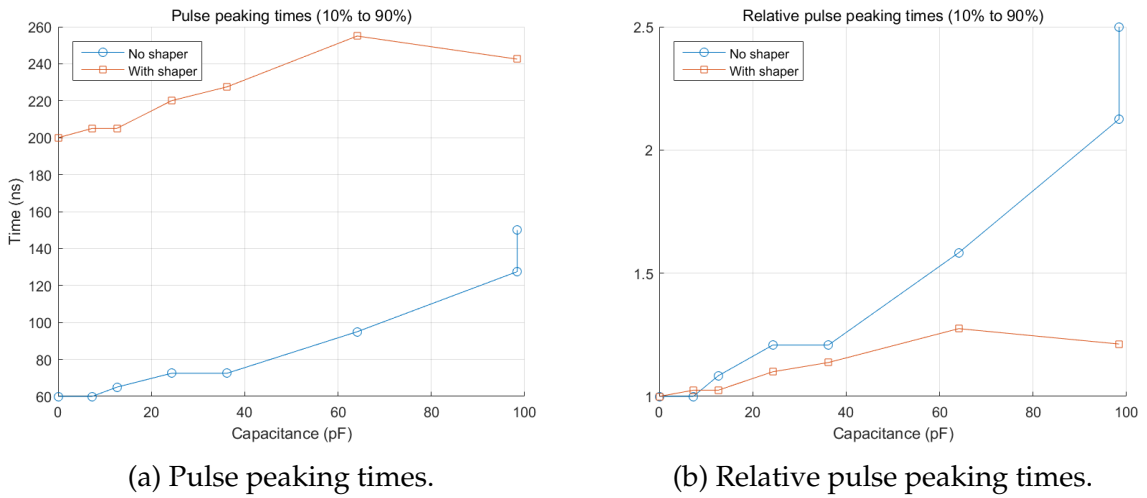


Figure 5.14: Pulse peaking time comparison with and without shaper connected.

5.3 Noise Measurements

Noise measurements on the IDE1180 have been performed with the ADC setup in figure 5.2, and the IDE1180 inside a Faraday cage. Three different methods have been used to measure the noise:

1. No input signal. Fit a Gaussian to the raw signal histogram.
2. With pulse on input. Fit a Gaussian to the raw signal histogram.
3. With pulse on input. Using peak detection. Fit a Gaussian to the peak histogram.

The results were expected to be somehow different on method three as it does not use the same histogram. Methods one and two observe variations in the baseline, while method three observes variations in the peak height. Figure 5.15 shows a comparison of measurement results on the same system with the three different methods. All methods show a slightly different slope. For method two, the higher noise values at high capacitance is because the histogram consists of two overlapping Gaussians.

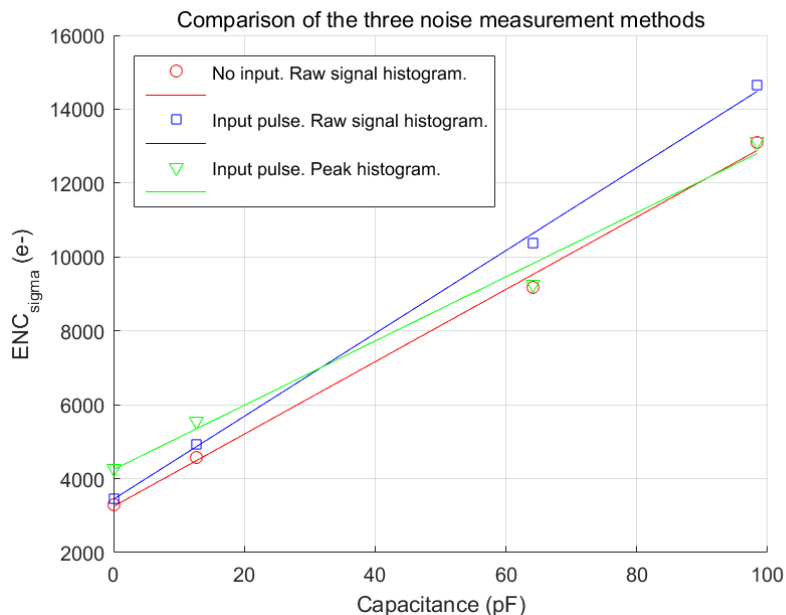


Figure 5.15: Comparison of the three noise measurement methods used.

Noise is calculated as Equivalent Noise Charge (ENC), the number of electrons needed on the input to create a signal equivalent to the measured noise, using eq. 5.1, where G is the gain, and σ (sigma) is the standard deviation of the noise histogram. The

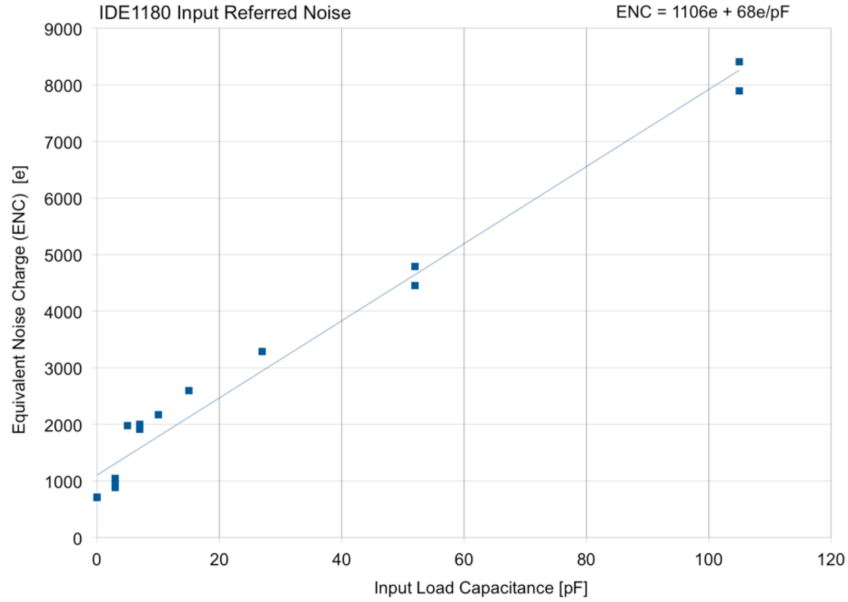


Figure 5.16: Measurement of the ENC vs. input capacitive load. [Maehlum et al., 2015]

noise can also be given in full width at half maximum (FWHM) by multiplying with $2\sqrt{2 * \ln 2}$ (≈ 2.355).

$$ENC_{\sigma}[e-] = \frac{\sigma[mV]}{G[mV/fC] * 1.6 * 10^{-4}[fC/e-]} \quad (5.1)$$

It is unknown if the noise measurement from IDEAS, figure 5.16, is measured from the baseline variations or peak height variations, or if it is calculated as σ or FWHM. It is therefore hard to compare to this measurement. Figure 5.17a shows a noise measurement using method 3, calculated with a gain of 12 mV/fC, as specified in the datasheet [Maehlum et al., 2015]. It is clear that the slope is extremely low, about 25 %, compared to the measurement from IDEAS in figure 5.16.

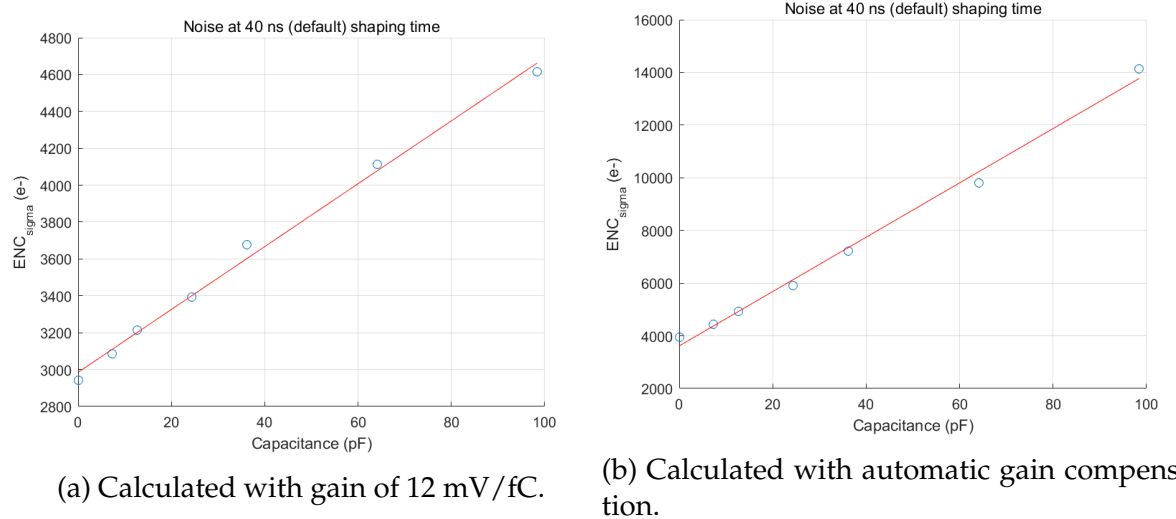


Figure 5.17: Measurements of the ENC vs. input capacitive load. Calculated with constant and changing gain.

5.3.1 Gain Compensation

As shown in equation 5.1, the gain is required to calculate the equivalent input noise, but as discussed in section 5.2 the gain varies with input load capacitance. It is therefore necessary to change the gain for different capacitances in the noise calculation. Originally, this was done using the tables in section 5.2, but as this is not optimal in case something in the system is changed. Therefore the MATLAB script for plotting the gain was modified to also calculate the gain at each capacitance when the third method for noise measurements was used. The gain is simply calculated by taking the mean of the peak histogram and dividing by the input charge.

When gain compensation is performed, see figure 5.17b, the noise curves have a slope very close to the one shown in the datasheet. Figure 5.18 shows the noise curves for all configured shaping times. We see that for longer shaping times, the noise becomes much less dependant on the capacitance. Figure 5.20 shows how the noise changes with shaping time. Unlike figure 4.5, this does not show a single minimum. The absolute minimum is at 100 ns, but there is a local minimum at 1 μs , where the absolute minimum was expected to be from theory. This non-linear behaviour could be explained by that it is not only the shaping time constant that is being changed for the different shaping times, but also the pole-zero cancellation, which has a large impact on the noise. Figure 5.19 shows the noise in mV measured on the output of the IDE1180. Here the two longest shaping times show the lowest noise levels, but since the gain is very low at these shaping times, the equivalent input noise is still high.

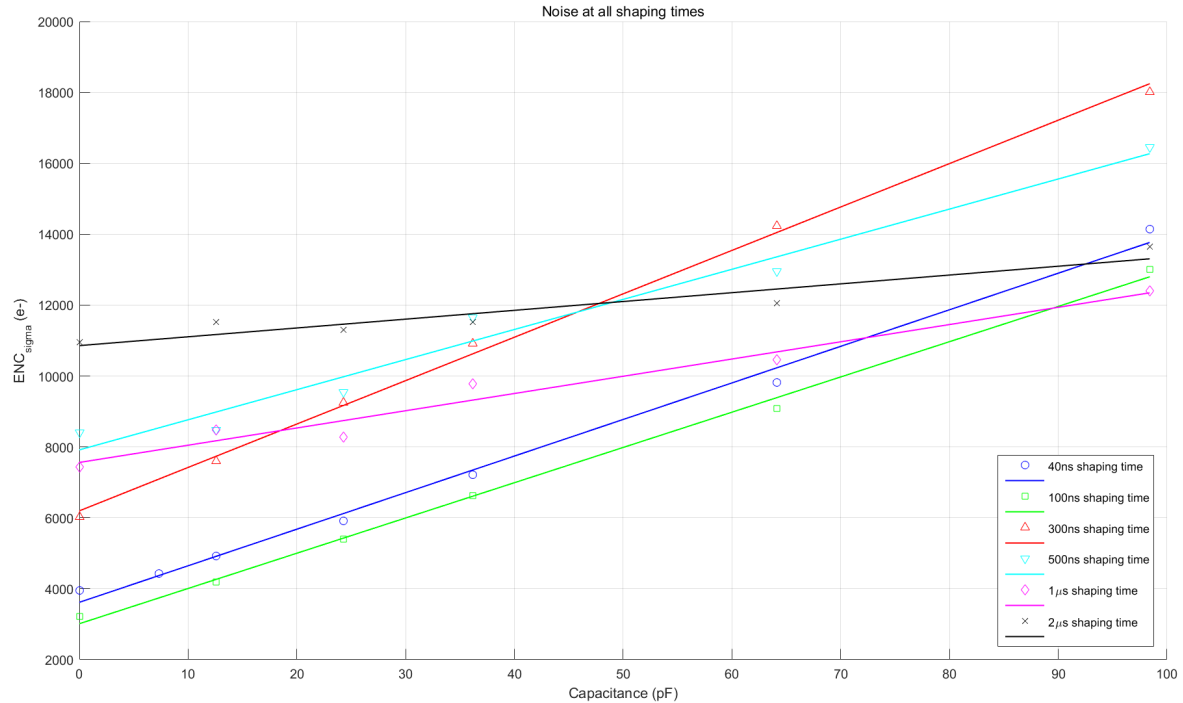


Figure 5.18: Measurements of the ENC vs. input capacitive load. Calculated with automatic gain compensation.

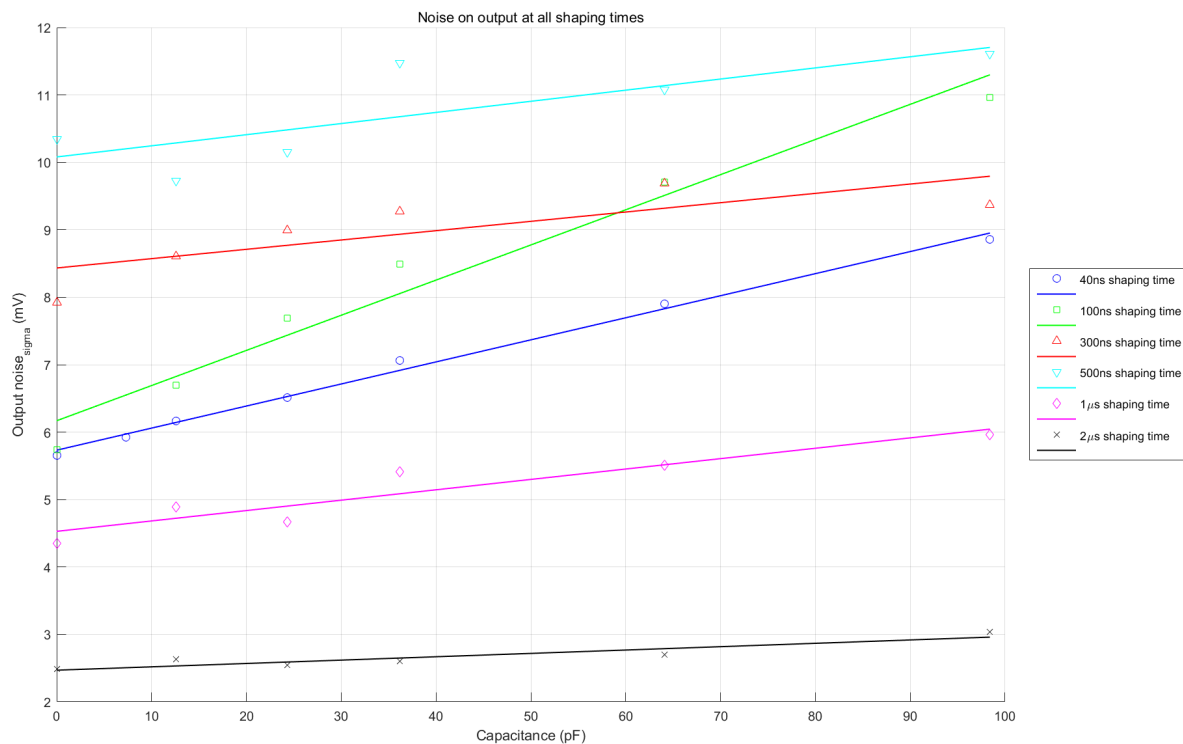


Figure 5.19: Measurements of the noise on the IDE1180 output vs. input capacitive load. Calculated with automatic gain compensation.

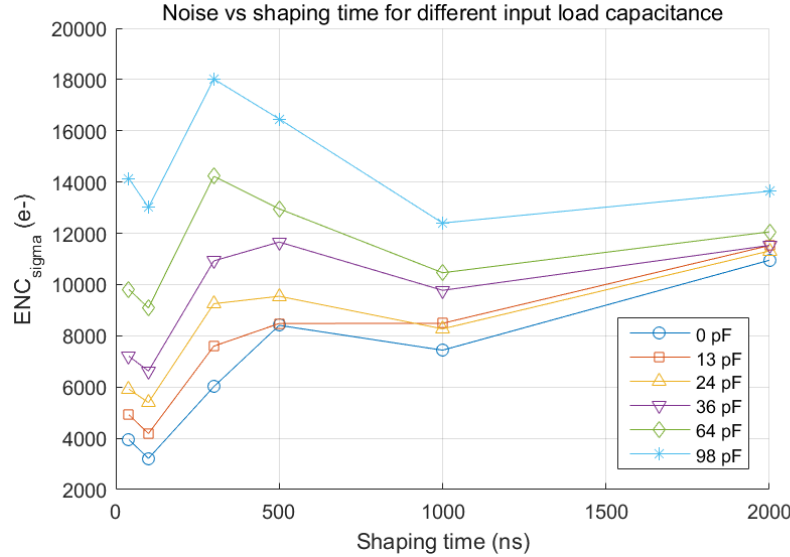


Figure 5.20: Measurements of the ENC vs. shaping time.

5.3.2 Noise from Input Circuitry

Since the noise measurements in the datasheet were performed directly on the ASIC while the measurements at UiB are performed on the PCB, it is easy to assume that the differences in noise are due to the extra input circuitry on the PCB. Therefore, noise measurements were performed with six different connections on the input. This was done with method 1 mentioned at the beginning of section 5.3 (except for measurement 6 which is using method 2), with 0 pF input load capacitance. Table 5.3 is used for gain compensation. The six connections were as following:

1. No input jumper on SV2 in figure 5.4 (SMA connector and 1pF capacitor disconnected from the ASIC).
2. Input jumper on SV2 (SMA connector and 1pF connected).
3. As 2, but aluminium foil covering input SMA.
4. Input jumper on SV2. SMA-BNC and BNC-LEMO adapters and short LEMO cable connected. Cable left floating.
5. As 4, but cable connected to wave generator. Generator powered on, but the output is turned off.
6. As 5, but with a ramp pulse from the generator output.

Table 5.7: Noise measurements with different input circuitry connected.

Measurement #	1	2	3	4	5	6
$\text{ENC}_\sigma [\text{e-}]$	1642	3578	3502	3527	3620	3944

The main conclusion from table 5.7 is that the input circuitry has a huge impact on the noise at low capacitance. From measurements 2-5, we see that the adapters, cable, and wave generator do not contribute noticeably to the noise. We also see an increase in noise between measurements 5 and 6, which indicates that method 2 is not a reliable form of measurement. Even though the noise for measurement #1 in table 5.7 is much lower, it is still twice the 0 pF measurement in figure 5.16. However, the input of the ASIC is still connected to one of the pins of the pin header, serving as an extra noise source that was not present in the measurement by IDEAS.

5.4 Gain Linearity

Gain linearity has been measured by saving pulses from the Agilent oscilloscope and using Matlab to find the pulse peak value. This was done since the buffer does not cover the entire dynamic range of the IDE1180. The IDE1180 was inside a Faraday cage. Since these measurements are only based on a single pulse for each data point, they have an extra inaccuracy from the noise that would be avoided by saving pulse height histograms on the ADC.

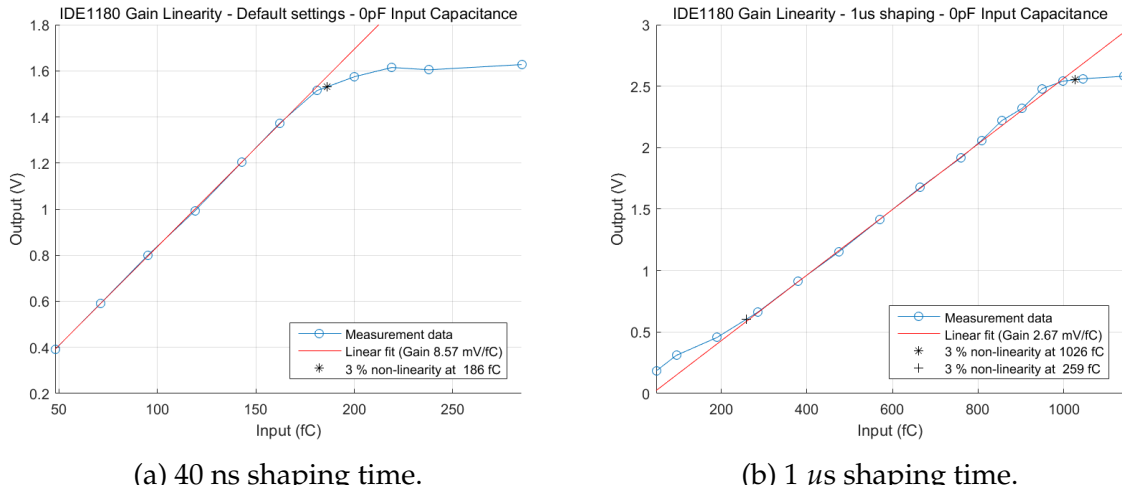


Figure 5.21: Two examples of gain linearity measurements.

Figure 5.21 shows two gain linearity graphs. The rest are in appendix E. The measurements at default settings look very much as expected with very good gain linearity, but all the other measurements show a bump in the low end, like in figure 5.21b. The

source of this is unknown, but it is likely not from measurement inaccuracies, since the same bump is visible for all the measurements. Since these configurations are far outside the shaping time range the IDE1180 is made to work in, some strange behaviour here is not unexpected. It is possible that it is somehow related to the pole-zero cancellation that is active for these configurations, but not the default setting. Another possibility is that the bump comes from noise, since the noise has a higher relative effect on weak signals. As seen in figure 5.20, the noise is higher for the other shaping times than for default settings.

5.5 Dynamic Range

The dynamic range of the pre-amplifier shaper is on the lower level limited by the noise. To be able to easily discern the signal from noise, the lower end of the dynamic range has been defined as 10 times the noise. The higher end of the dynamic range is set from the gain linearity curves, as the point where the curve is no longer linear. Table 5.8 shows the low and high limits to the dynamic range from the noise and gain linearity. The low limit from the gain linearity will not necessarily be a problem, but it is still listed in the table so it is not forgotten. It is possible to compensate for it using a linearising circuit or algorithm.

Table 5.8: Dynamic range measurements.

Setting & input load	Low limit [fC] (noise*10)	Low limit [fC] (gain linearity)	High limit [fC] (gain linearity)
40 ns 0 pF	6.4		186
40 ns 36 pF	11.5		235
500 ns 0 pF	13.4	80	180
500 ns 36 pF	20.3	97	211
1 μ s 0 pF	12.0	259	1026
1 μ s 36 pF	15.7	355	1040
2 μ s 0 pF	17.6	553	1769
2 μ s 36 pF	18.4	506	1755

The dynamic range has only been accurately calculated for the default gain setting. For the other three gain settings, the higher end of the dynamic range has been estimated by observing the output of the IDE1180 using the Tektronix oscilloscope. See table 5.9. The actual maximum input charge is slightly lower than this, as it is hard to see on an oscilloscope exactly when the pulse height increase stops being linear. Note that these estimates are very different from the 50/100/200/400 fC listed in the datasheet [Maehlum et al., 2015].

Table 5.9: Dynamic range estimates for different gain settings.

PA_GAIN<1:0>	Q _{in,max} [fC]	
00	GND-GND	200
01	GND-3V3	240
10	3V3-GND	300
11	3V3-3V3	440

5.5.1 Input Sharing

Input sharing was investigated as a method to increase the dynamic range to a higher level than what is possible by reducing the gain. The thought behind this was to connect multiple channels of the IDE1180 to the same signal, expecting that the signal charge would spread evenly across the channels. From this, it would be possible to divide the signal by a number between 2 and 15. However, tests showed that the charge was not spread evenly across the channels, making this method unreliable.

5.6 Shaping Time

The shaping time has some variations from the input load capacitance and input capacitance. The shaping times listed in table 5.2 are therefore not always accurate. Table 5.10 shows shaping time versus input load capacitance, calculated from the data that was used to create figures 5.12 to 5.14. These fluctuations appear very small and random, and could come from the noise. Figure 5.22 and appendix F show shaping time variations with input charge. These variations are larger, and appear more structured, with a general trend of increased shaping time with higher input charge. These data are calculated from the results of the gain linearity measurements. All the data in this section is calculated from snapshots of a single pulse, and therefore not the most accurate. If accurate measurements of the shaping time is needed, this could be done with a more complex LabVIEW program that calculates the shaping time of every pulse. The difference between the shaping times in table 5.10 and figure 5.22a is caused by the same issue as discussed in section 5.2 and figure 5.7. The results in this section can therefore be expected to be slightly higher than what would be obtained with a lower line capacitance.

Table 5.10: Shaping time vs. input load capacitance.

Capacitance [pF]	0	7.3	12.6	24.3	36.2	64.1	90.4
Shaping time [ns]	63.0	63.5	59.5	60.0	62.0	53.5	61.0

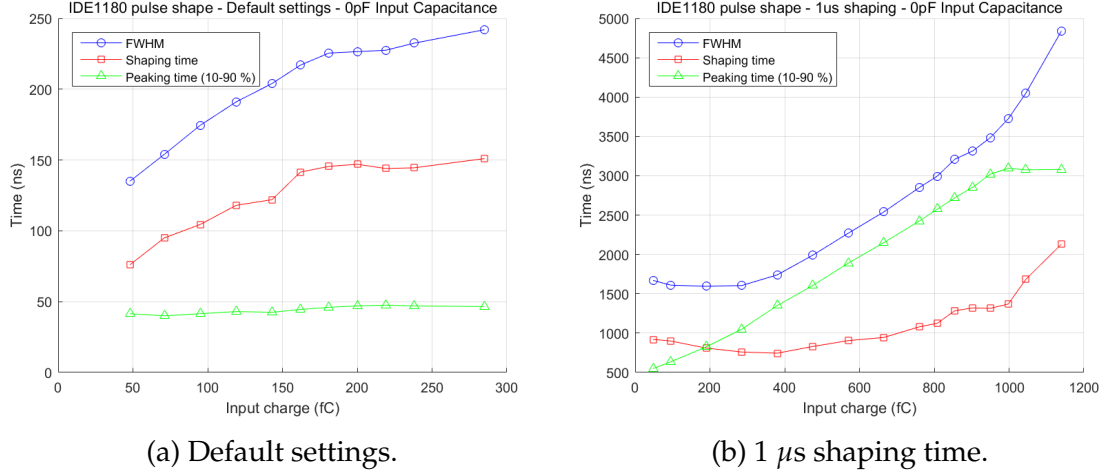


Figure 5.22: Two examples of shaping time, FWHM, and peaking time measurements.

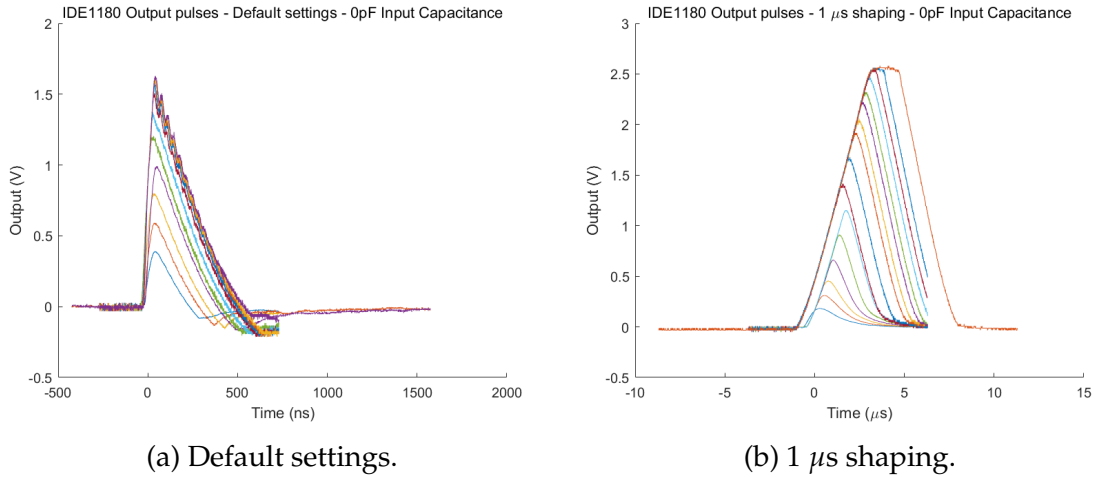


Figure 5.23: Output pulses from IDE1180 with input signals of varying charge. These are the pulses used to find gain linearity.

5.7 Peaking Time

Figure 5.23a shows that at 40 ns shaping time the slope increases when the amplitude increases, which makes sure that the peaking time is more or less unchanged, see figure 5.22a. For increased shaping time however, the slope in 5.23b is constant for all input charges. This leads to a greatly increased peaking time for higher input charges, see figure 5.22b. This unchanging slope looks very linear, which leads to the assumption that this could due to a slew rate limitations. The changes to the system performed to increase the shaping time might have reduced the maximum slew rate, which makes the system unable to increase the voltage fast enough. All peaking time measurements can be seen in appendix F. Peaking time has been calculated from 10 % to 90 % of peak value to reduce errors from the noise.

5.8 Crosstalk

It was attempted to measure crosstalk between the channels by measuring the noise on channel 2, with an input signal on channel 1. However, the crosstalk signal was too close to the noise to be noticeable on the noise histogram. Therefore, measurements were instead done by measuring the amplitude of the crosstalk signal by using an external trigger signal from the wave generator. Crosstalk was measured with the ADC, for default and 1 μ s shaping time, see table 5.12. For each shaping time, it was measured for the minimum amplitude from the Tektronix AFG3252 wave generator, and for the maximum amplitude before the in-house buffer cuts the signal. The wave generator signal was sent to channel 1, while the other channels were measured. The crosstalk was also roughly measured for default shaping time using cursors on the Agilent MSO-X 3104A oscilloscope, table 5.11, which showed that the crosstalk is roughly the same three channels away from the signal, as fifteen channels away. Therefore, the ADC measurements, which take some time, were not done for channels 6 to 15.

Table 5.11: Crosstalk estimates using oscilloscope. Input signal to channel 1.

Channel #	V _o [mV] (Q _{in} = 48fC)	[%]	V _o [mV] (Q _{in} = 95fC)	[%]	V _o [mV] (Q _{in} = 190fC)	[%]
1	375	100 %	775	100 %	1500	100 %
2	6.5	1.73 %	10	1.29 %	18	1.20 %
3	5.5	1.47 %	8.5	1.10 %	14	0.93 %
4	4.5	1.20 %	6	0.77 %	8	0.53 %
5	4.5	1.20 %	6	0.77 %	8	0.53 %
6	4	1.07 %	6	0.77 %	8	0.53 %
7	4	1.07 %	6	0.77 %	8	0.53 %
8	4	1.07 %	6	0.77 %	8	0.53 %
9	4	1.07 %	6	0.77 %	8	0.53 %
10	4	1.07 %	6	0.77 %	8	0.53 %
11	4	1.07 %	6	0.77 %	8	0.53 %
12	4	1.07 %	6	0.77 %	8	0.53 %
13	4	1.07 %	6	0.77 %	8	0.53 %
14	4	1.07 %	6	0.77 %	8	0.53 %
15	4	1.07 %	6	0.77 %	8	0.53 %
16	4	1.07 %	6	0.77 %	8	0.53 %

The noise during the table 5.11 was estimated to 4 mV, so the highest crosstalk was about 4.5 times the noise. Relative to the signal on channel 1, the crosstalk was between 0.5 % and 1.75 % of the signal strength.

Table 5.12: Crosstalk measurements. Input signal to channel 1.

Channel #	V_o [mV] ($Q_{in} = 48fC$) (40 ns shaping)	V_o [mV] ($Q_{in} = 95fC$) (40 ns shaping)	V_o [mV] ($Q_{in} = 48fC$) (1 μ s shaping)	V_o [mV] ($Q_{in} = 475fC$) (1 μ s shaping)
1	411.6 (100 %)	839.3 (100 %)	157.2 (100 %)	990.8 (100 %)
2	6.5 (1.58 %)	10.8 (1.29 %)	3.2 (2.04 %)	10.8 (1.09 %)
3	5.6 (1.36 %)	8.0 (0.95 %)	3.4 (2.16 %)	10.8 (1.09 %)
4	4.9 (1.19 %)	5.3 (0.63 %)		3.1 (0.31 %)
5	4.9 (1.19 %)	5.4 (0.64 %)		
16	5.2 (1.26 %)	5.4 (0.64 %)	2.3 (1.46 %)	2.9 (0.29 %)

Table 5.12 shows crosstalk between 0.3 % and 2 % of the signal strength. The noise was measured to roughly 3 mV for these measurements, making the highest crosstalk 3.6 times the noise. These measurements are a lot more accurate than the estimates in table 5.11, but the estimates are also included in this thesis as they cover the high end of the dynamic range that cannot currently be measured using the ADC.

5.9 Power Consumption

Power consumption was measured for different shaping times by connecting an ampere-meter between the power supply and the IDE1180. The power consumption was not affected by the input charge to the chip.

Table 5.13: Power consumption measurements.

Shaping time [ns]	40 (Default)	500	1000	2000
Power consumption [mW]	224	235	223	208

The power consumption values in table 5.13 are a lot higher than the 32 mW from the datasheet. This is expected, as the datasheet is made from measurements directly on the chip. The extra power consumption comes from components on the PCB.

5.10 Pile-up Considerations

The maximum count rate that can be used without causing pile-up has been calculated from the time between the pulse starts to rise until the signal has returned to the stable baseline, see table 5.14. This has been measured at the highest input signal of the dynamic range, as the pulse width is slightly increased by input charge. No dependency on input load capacitance was observed, so this was measured only with a capacitance of 24 pF. This was measured with the IDE1180 inside a Faraday cage, but with the lid of the cage open and a cable directly to the Agilent oscilloscope to avoid the problems of figure 5.7. Due to the noise of this setup, an accurate measurement is not easy, and this is therefore only an estimate. At 40 ns shaping time, the maximum count rate can be greatly increased by eliminating the undershoot using pole-zero cancellation.

Table 5.14: Pile-up estimates.

Shaping time [ns]	40 (Default)	500	1000	2000
Deadtime [μ s]	3	4	7	12
Maximum count rate [kHz]	333	250	145	85

5.11 The 7048 Evaluation Board

As mentioned in the beginning of this chapter, two evaluation boards were received by IDEAS. The gain on the 7048 board was briefly tested, shown in table 5.15. The difference between this and the 7045 board, table 5.3, led to an investigation on the gain settings of the 7048 board. This, in table 5.16, shows that on the 7048 chip, unlike the 7045, the gain was different for gain inputs floating and to ground. It should also be noted that for the 7045 board, gain inputs to ground gives the highest gain, while on the 7048 board 3.3 V gives the highest gain. Because of this strange behaviour, the 7048 board has not been tested any more, as it is hard to trust its settings.

Table 5.15: Gain [mV/fC] vs. capacitance measured with ADC on the 7048 PCB, with no jumpers in place.

PA_GAIN<1:0>	0pF	10pF	56pF	56pF	100pF
X-X	3.19	2.66	2.23	1.51	1.12

Table 5.16: Gain [mV/fC] measurements for different gain settings measured with oscilloscope on the 7048 evaluation board.

	PA_GAIN<1:0>	Gain
11	3V3-3V3	5.4
1X	3V3-X	5.2
10	3V3-GND	3.45
X1	X-3V3	5.3
XX	X-X	3.2
X0	X-GND	2.35
01	GND-3V3	2.2
0X	GND-X	1.8
00	GND-GND	1.0

Conclusions & Outlook

The work of this thesis on the 3DMiMic detectors suggests that SINTEF's fabrication process has been a success. The newest wafer shows many good I-V curves, and the newer wafers produced from the experiences of the measurements of this thesis should have some improvements. The detectors still need to be properly tested with radiation before any definite conclusions can be made. This work will be continued by Andreas Samnøy in his Ph.D. work, as well as by researchers at the University of Wollongong.

The work on the prototype IDE1180 pre-amplifier & shaper shows many deviations to the preliminary datasheet. Some differences were expected, as the preliminary datasheet was made from measurements directly on the ASIC without a test PCB. It might be possible to reduce many of the differences by designing a new PCB. The deviation in gain and dynamic range at the four gain settings between measurements and datasheet might suggest that the tests are executed on different revisions of the ASIC design. The high dependence of the gain to input load capacitance shows that the IDE1180 might have problems with detectors with high capacitance and requirements for high gain. This should not be an issue for the 3DMiMic detectors that have relatively low capacitance. The noise measurements show that the input referred noise is five times higher than in the datasheet at low input capacitance, and 75 % higher at high capacitance. This can partly be explained by extra noise from the PCB, but it is difficult to do a direct comparison as it is unknown how IDEAS has calculated the input referred noise from the measured noise on the output. Crosstalk between channels is not an issue as it is comparative to the noise.

As the 3DMiMic detectors have not yet been tested in detail with radiation, the charge collection time is not known. Therefore the minimum requirement for shaping time is unknown. At shaping times of 1 and 2 μ s it is possible to read out the biggest signals expected from the 3DMiMic detectors by using the IDE1180, while the dynamic range is not big enough at default settings and 500 ns shaping time. IDE1180 fails the requirements for 3DMiMic when it comes to the smallest signals. A Minimum Ionizing Particle is expected to deposit about 1000 electrons, while the lowest noise measured for IDE1180 is equivalent to about 3000 electrons on the input. IDE1180 usefulness

for the 3DMiMic detectors will therefore depend on the importance of the smallest radiation particles to the measurements. If the IDE1180 is going to be used, it will be crucial to make a portable Faraday cage to protect it from noise. This cage should be designed so that it does not affect the output signal as seen in figure 5.7. Note that the IDE1180 is designed for short shaping times and very low input load capacitance, and is therefore taken out of its element in many of these tests.

Because of the high noise levels of the other investigated circuits with a usable shaping time, I would recommend using the ORTEC 142A with the 3DMiMic for the time being. This requires the purchase of a fitting portable shaper. The 142A also fails the noise requirements of the 3DMiMic, but by a much smaller margin. The 142A datasheet specifies about 550 electrons of noise at 20 pF. This is lower than the 1000 electrons from a MIP, but by such a small margin that it can be hard to reliably measure these particles. However, the only known electronic systems with a noise level of less than 100 electrons are made for bump-bonding and therefore cannot be used directly with the standard 3DMiMic layouts. In the future it should be considered to either create a new dedicated readout system for 3DMiMic, or modify an existing system that is close to the 3DMiMic requirements. This could for example be IDE1180 or ALICE TPC PASA.

Appendices

Appendix A: 3DMiMic Layouts

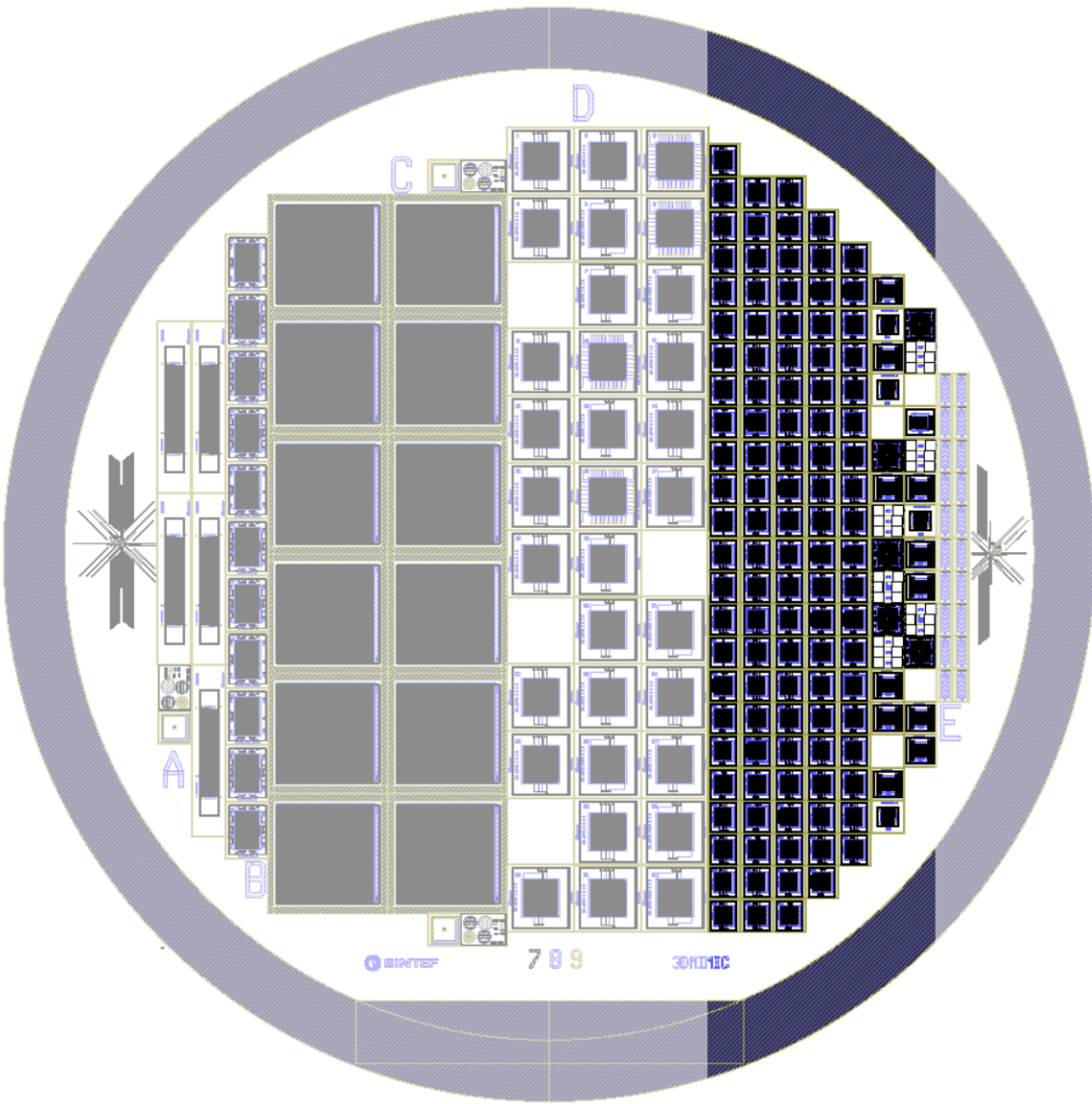


Figure A.1: 3DMiMic wafer.

Figure A.1 shows a whole 3DMiMic wafer. The highlighted area are the detectors that are relevant for this thesis. The large detectors on the left are made to be bump bonded with a Medipix chip. Figures A.3 to A.11 show some of the different layouts in the highlighted area. The detectors with "_L" in the name are of the "30 μm " size, while the others are of the "15 μm " size, see figure A.2. All figures in this appendix are from Marco Povoli at SINTEF.

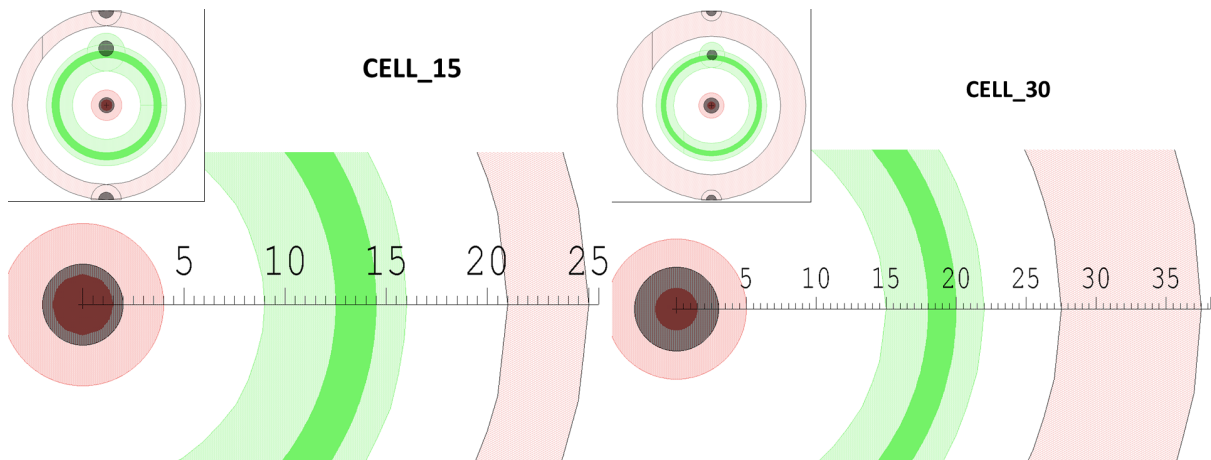


Figure A.2: 3DMiMic cell sizes. Distance scale is in μm .

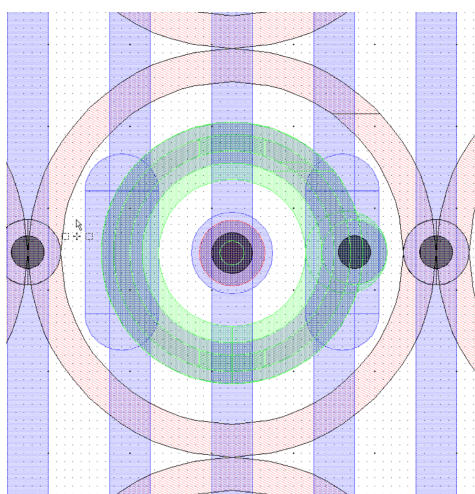


Figure A.3: MIC_ARRAY_1 layout.

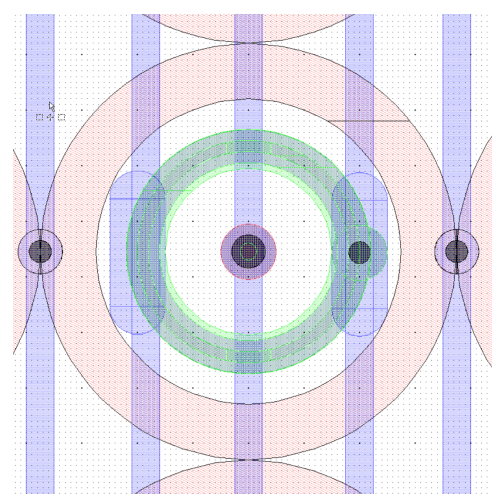


Figure A.4: MIC_ARRAY_1_L layout.

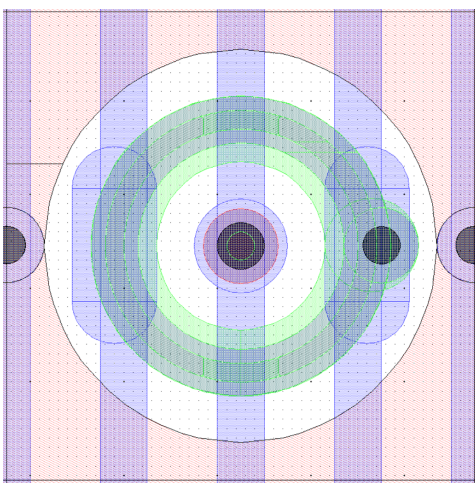


Figure A.5: MIC_ARRAY_2 layout.

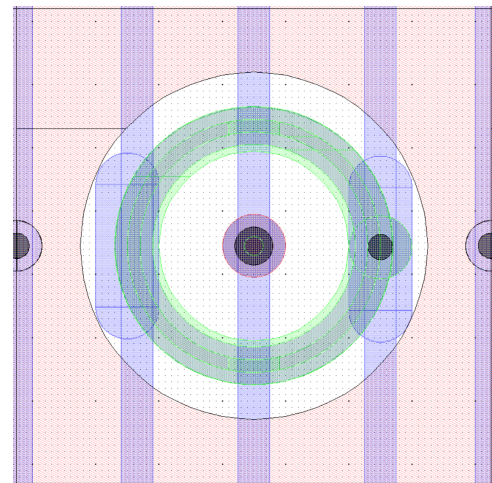


Figure A.6: MIC_ARRAY_2_L layout.

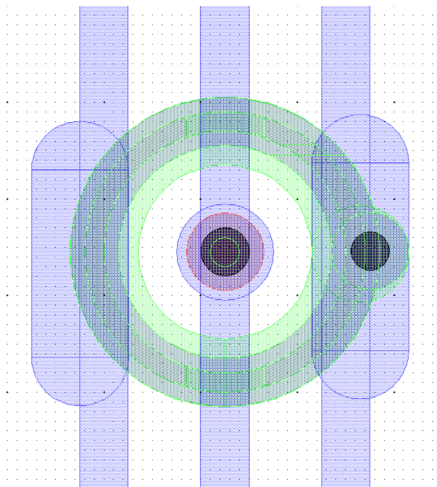


Figure A.7: MIC_ARRAY_3 layout.

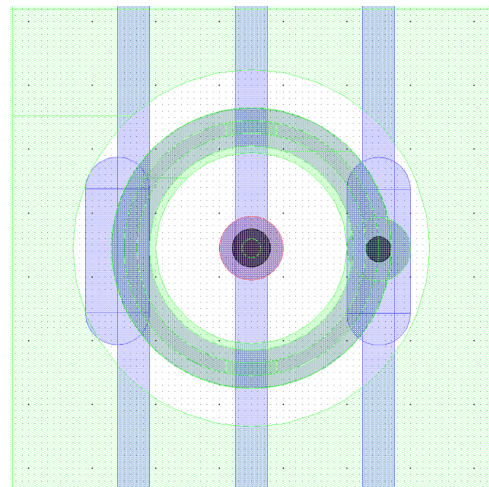


Figure A.8: MIC_ARRAY_3_L layout.

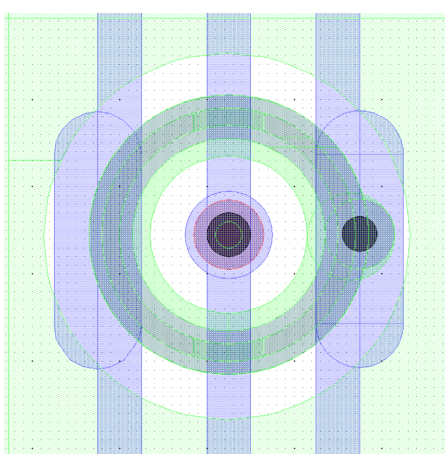


Figure A.9: MIC_ARRAY_PSTOP layout. Figure A.10: MIC_ARRAY_3_PSTOP_L layout.

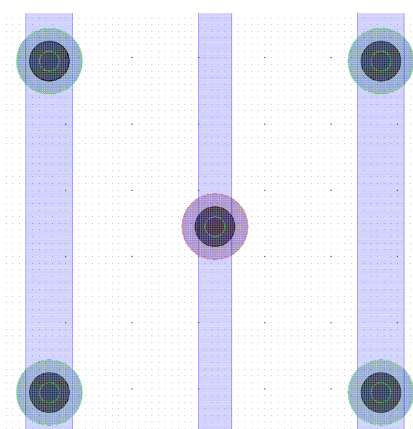
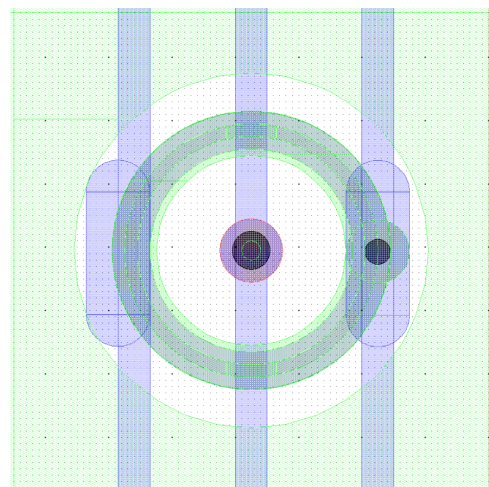


Figure A.11: MIC_3D layout. Every second column is n+ or p+ pillars.

The differences between the measured wafers are listed below [Povoli, 2016]:

S10-01 Fully planar wafer, all dopings performed with implantation.

S10-02 Same as S10-01.

S10-04 The p+ trench is NOT CLOSED and not filled with poly and is doped with gas phase, the n+ is planar and doped with implantation.

S10-11 Both p+ and n+ are etched but not filled, both dopings performed with gas phase.

S10-14 FULL 3D, both gas phase, but OLD metal (connection issues due to broken metal links).

S10-15 Both p+ and n+ etched and NOT CLOSED and not filled, p+gas phase, n+ implanted. (This wafer was tested in Japan).

S10-16 Like S10-15 but the p+ is also implanted.

S10-17 FULL 3D, complete trench and filled with poly, both doping gas phase, NEW METAL and no overetch in the process, should have better metal contacts than S10-14.

Appendix B: 3DMiMic I-V Measurements

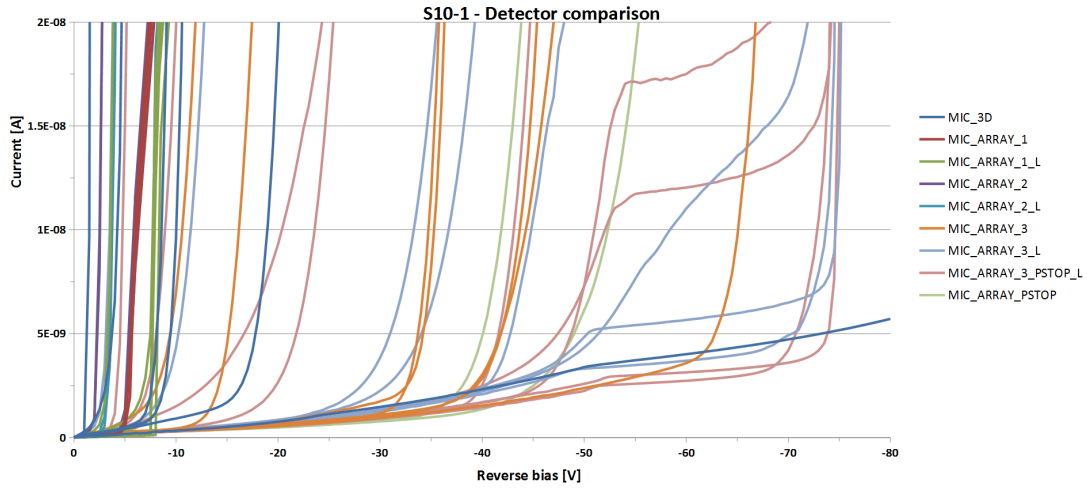


Figure B.1: I-V measurement of the S10-1 wafer.

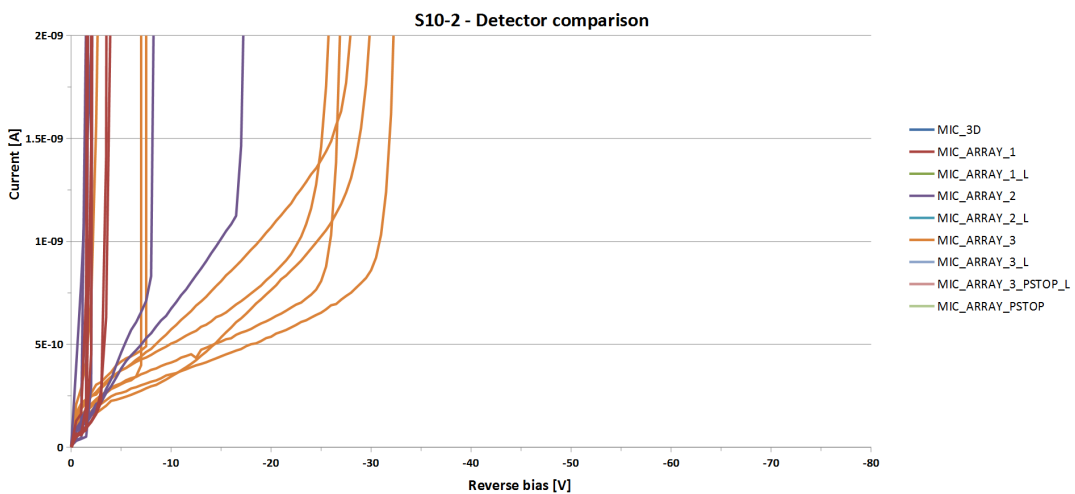


Figure B.2: I-V measurement of the S10-2 wafer.

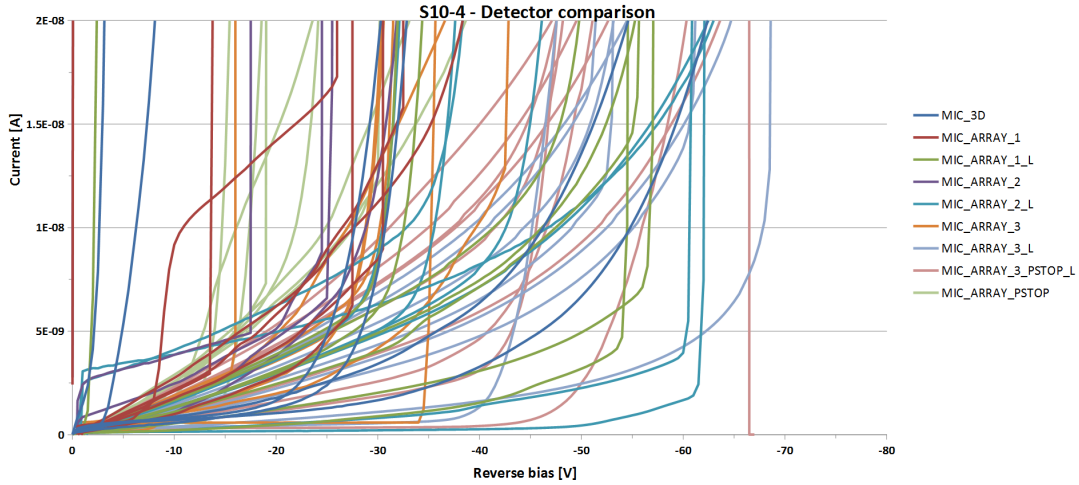


Figure B.3: I-V measurement of the S10-4 wafer.

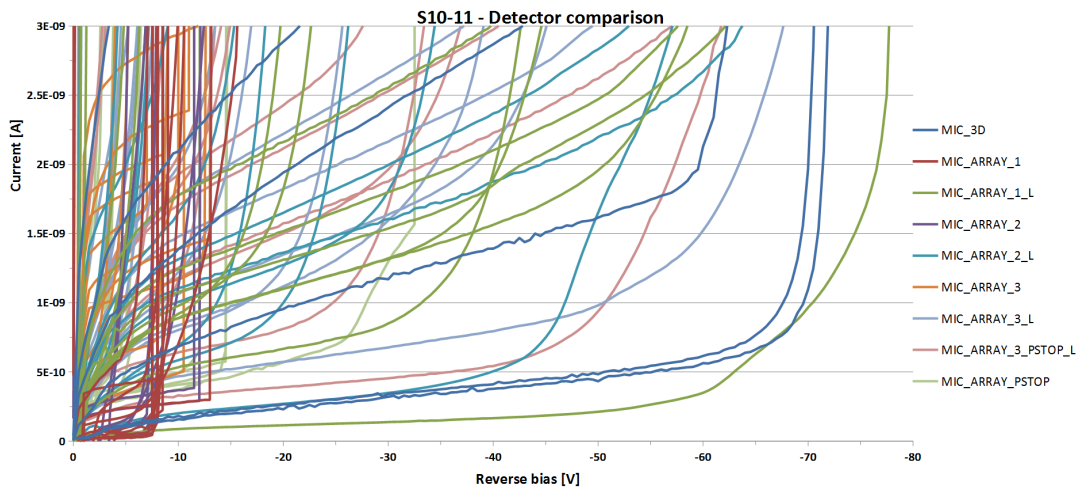


Figure B.4: I-V measurement of the S10-11 wafer.

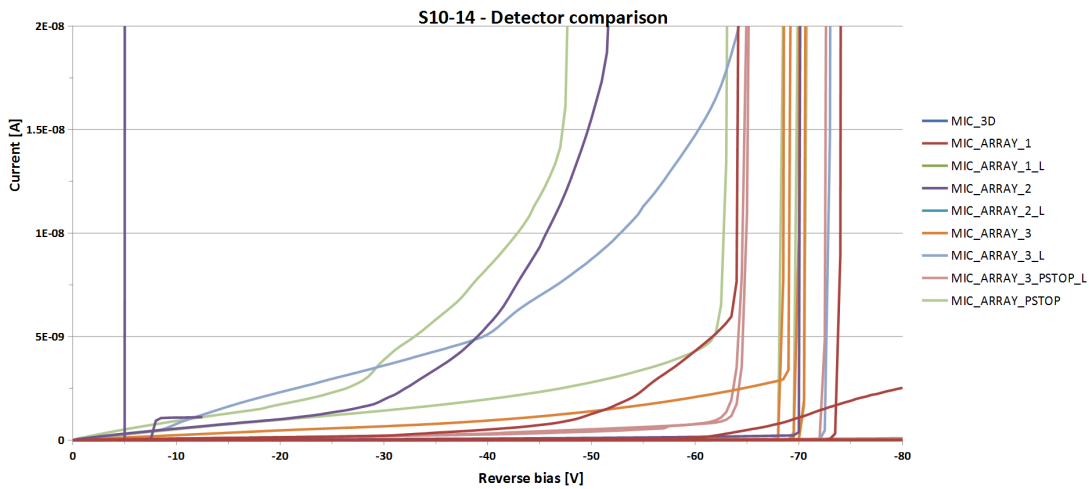


Figure B.5: I-V measurement of the S10-14 wafer.

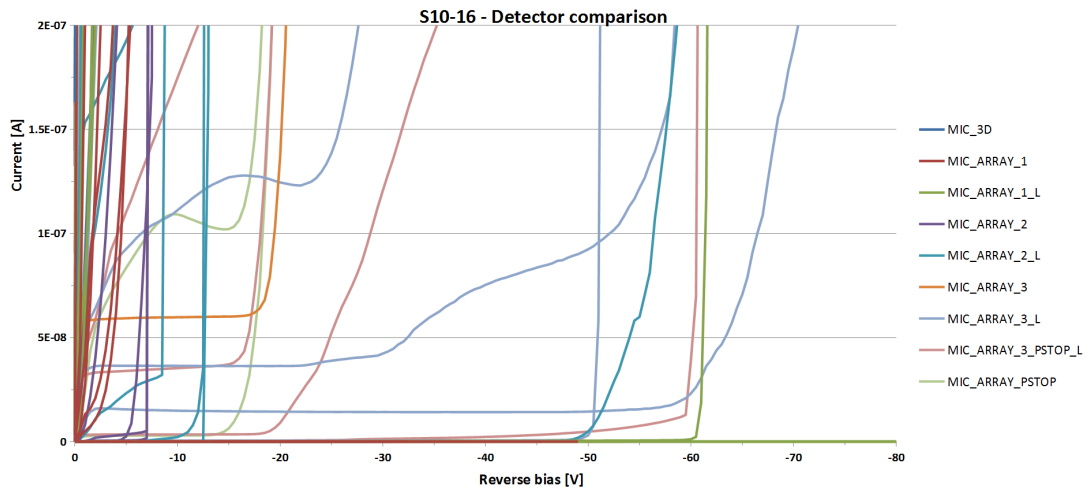


Figure B.6: I-V measurement of the S10-16 wafer.

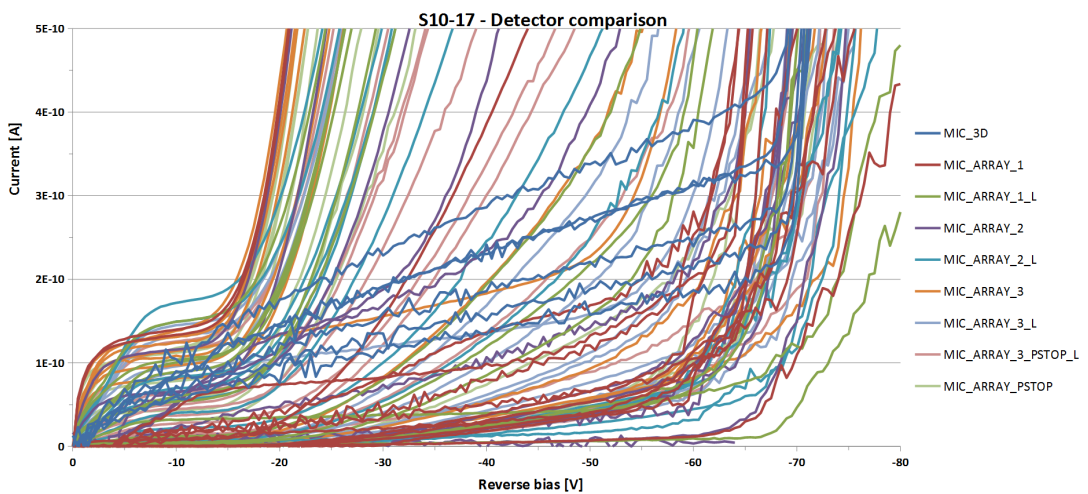


Figure B.7: I-V measurement of the S10-17 wafer.

Appendix C: Detector Interface PCB

A PCB was needed to connect the detector to the outside world, as the detector pads are too small for any other connection than wire-bonding. This PCB could simply have consisted of wire-bonding pads going to connectors for cables, but it was decided to make a more multi-purpose board to make it simple to try different set-ups. The board was made so that it is possible to connect the substrate, the guard rings, and the p+ rings individually to ground or external bias. It is also possible to read out the guard rings of the cells. Each channel can also be connected to a bias filter for removal of high frequency noise. The n+ core readout channel was designed to add as little capacitance as possible. LEMO connectors were chosen to connect to the outside world as they are well shielded and much used at IFT. The exposed metal is coated with electroless nickel immersion gold (ENIG) to provide better contact for wire-bonding. One mistake was done with the PCB design in that solder mask where the detector is mounted was forgotten. This has no consequences for the 3DMiMic detector, since there is an insulating layer between the bulk and the support wafer. The solder resist can be scratched off if the PCB is to be used for a different detector. The layout of the PCB can be seen in figure C.2 and a photograph can be seen in figure C.1.

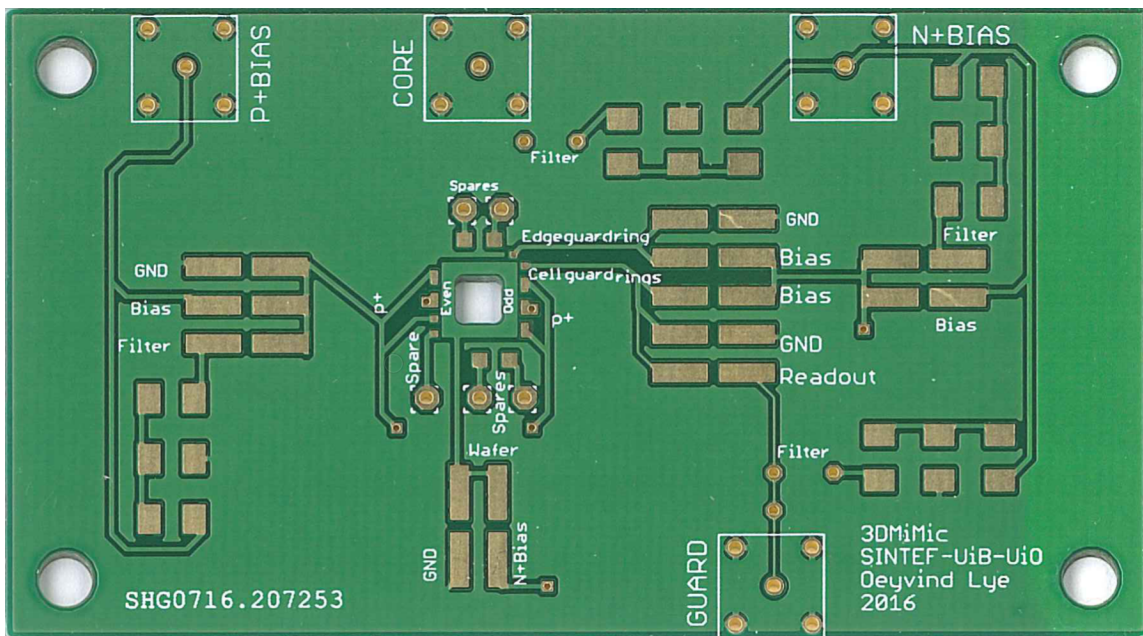


Figure C.1: Top side of PCB.

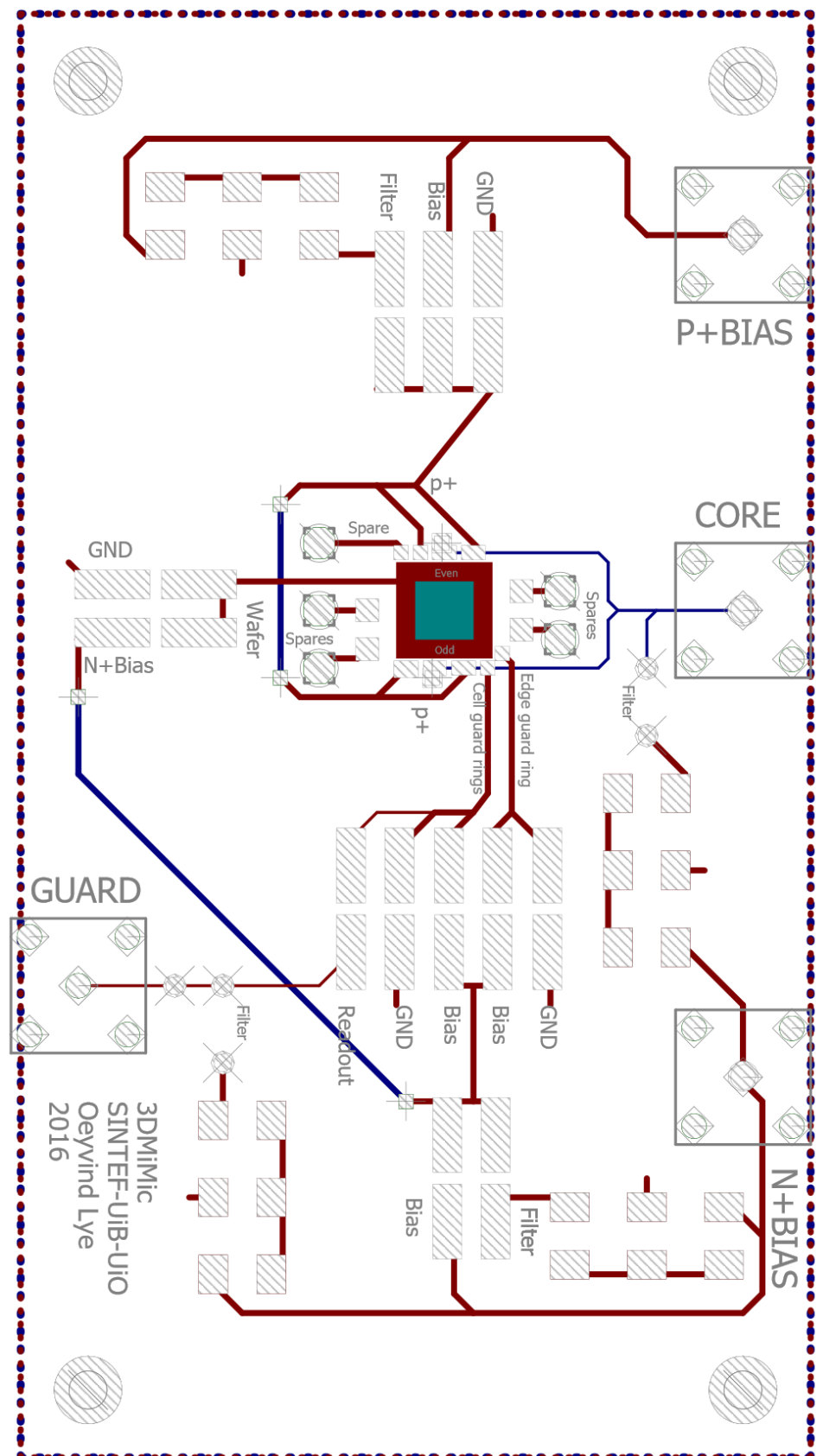


Figure C.2: PCB layout. Ground planes not shown.

After the design had been produced, it was again considered to read out the two sides of the detector separately, instead of in one signal. On the PCB, this can be solved by wire-bonding one of the sides to one of the spare pads and connecting this to the through-hole by the GUARD connector with a wire. To avoid extra capacitance, the wires leading to the unused surface-mounting pads can be cut with a knife. If cutting the wires after the detector has been mounted, try to protect the detector from flying debris. A new layout for two channel readout has been designed, and can be produced when needed.

UiB uses an X-Y table to position detectors during beam tests. This can move the detector in two dimensions with small, controlled steps. A mount was designed that can be used to connect the PCB to the X-Y table, see figure C.3.

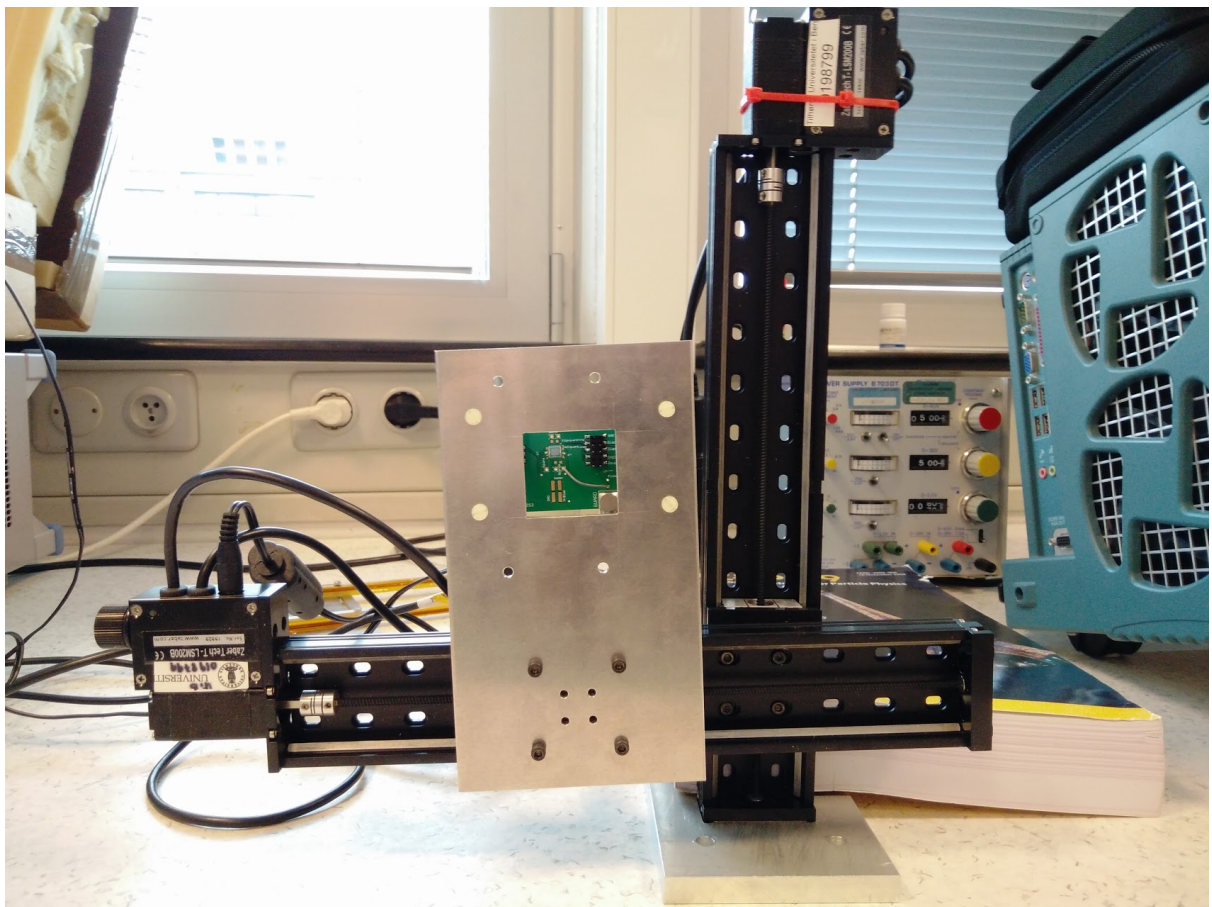


Figure C.3: 3DMiMic PCB mounted on X-Y table.

Figures C.4 to C.6 show how wire-bonding should be performed for different detectors and readout schemes. Figures C.7 to C.9 show where external wires (red) should be soldered, and where PCB lanes should be cut (black). Dotted line for optional wires not necessary for detector operation.

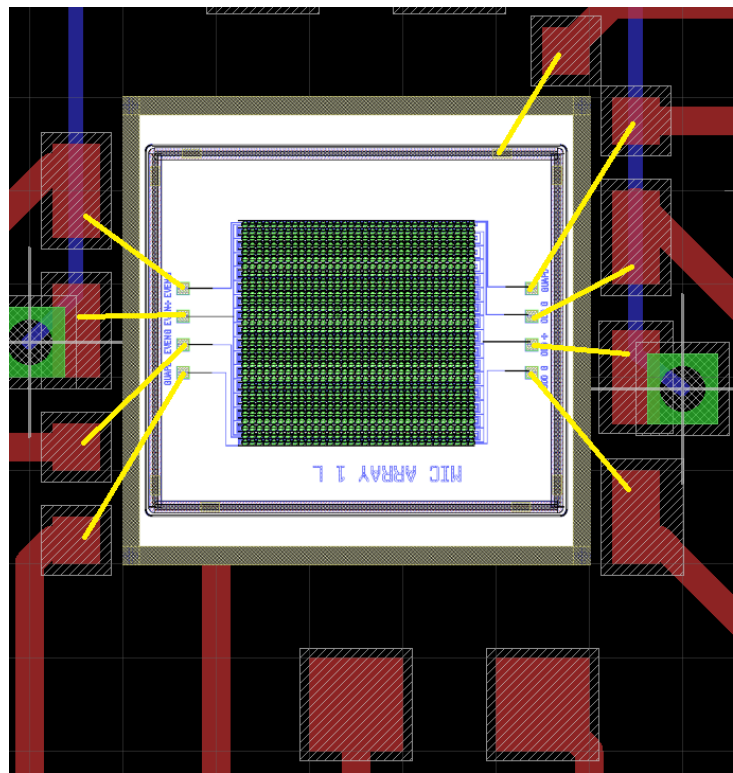


Figure C.4: Wirebonding for single channel readout on a detector with n⁺ guard rings.

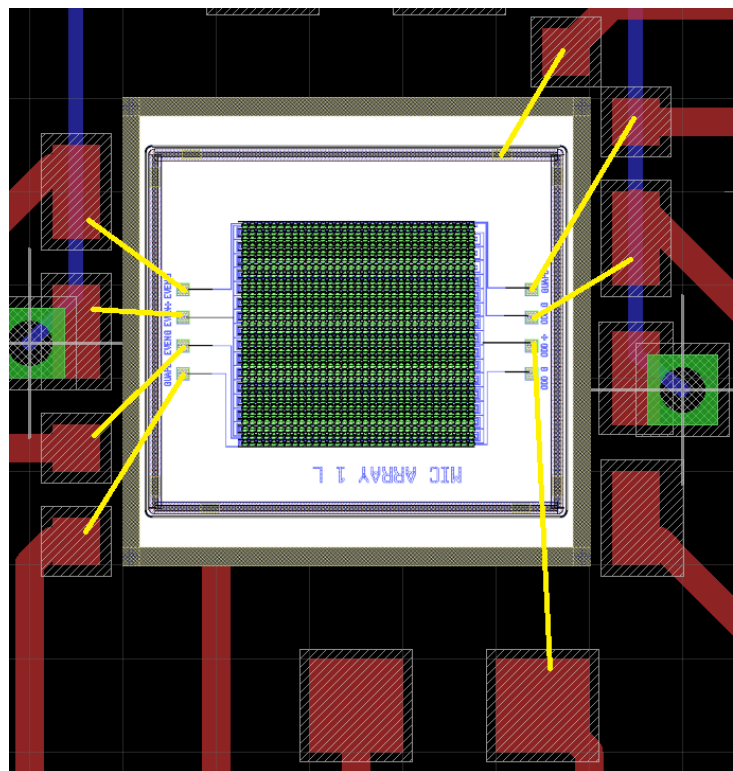


Figure C.5: Wirebonding for two channel readout on a detector with n⁺ guard rings.

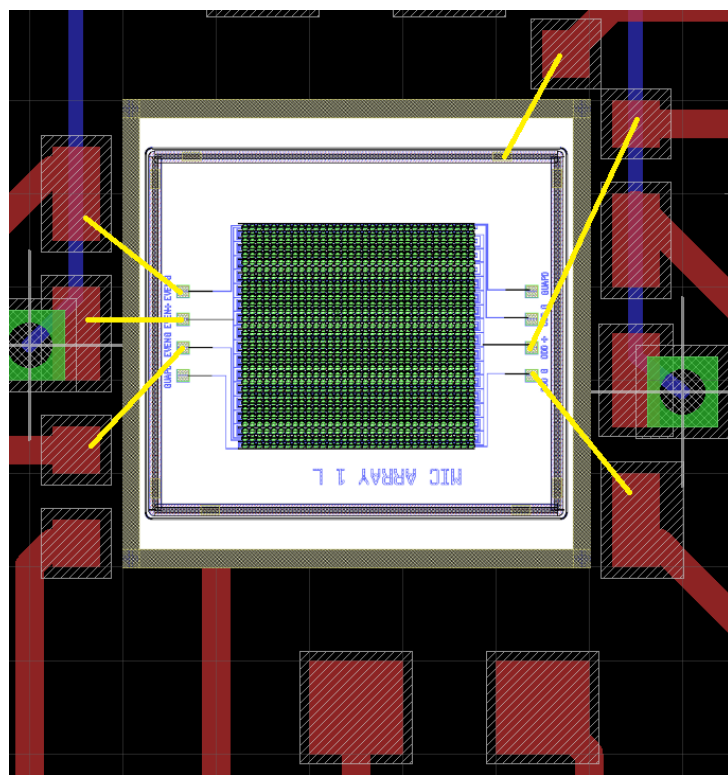


Figure C.6: Wirebonding for two channel readout on a detector without n+ guard rings.

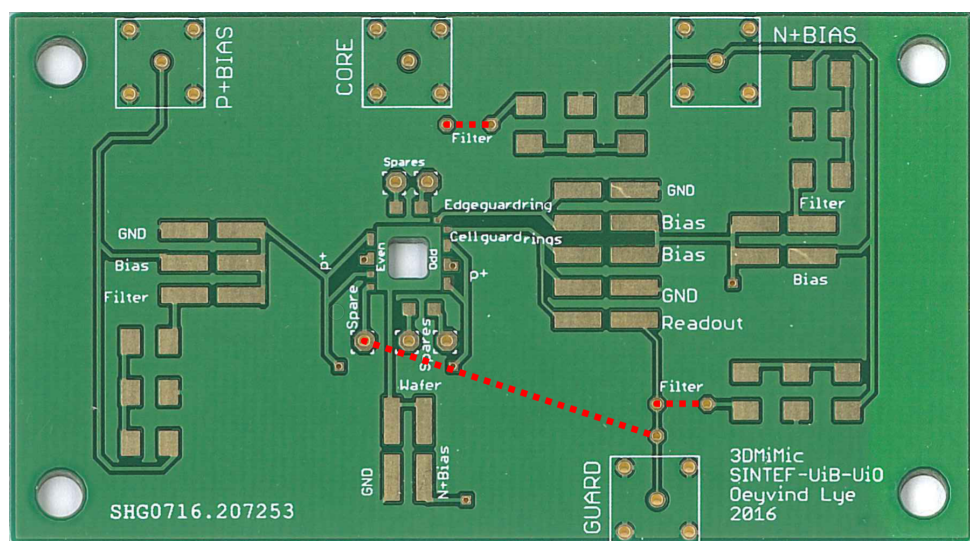


Figure C.7: Wiring for single channel readout on a detector with n+ guard rings.

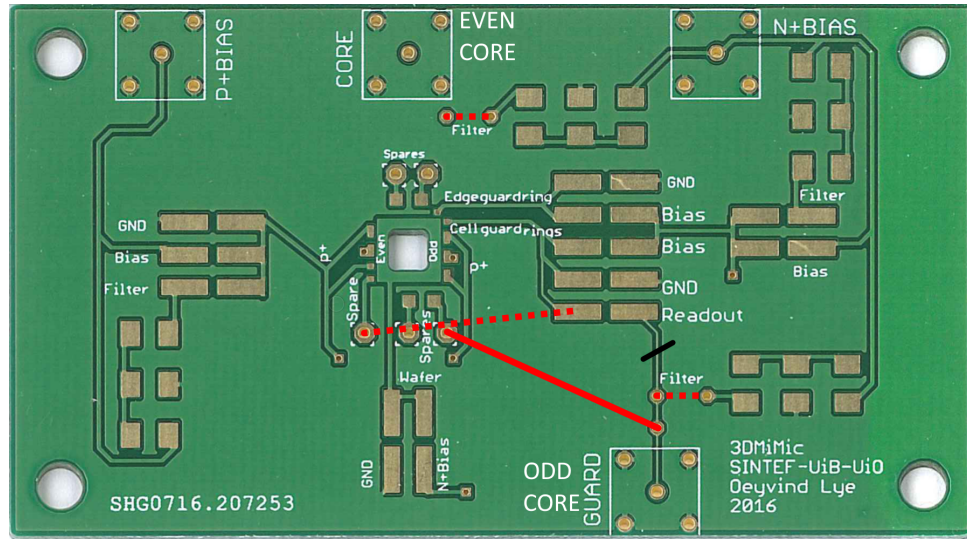


Figure C.8: Wiring for two channel readout on a detector with n+ guard rings.

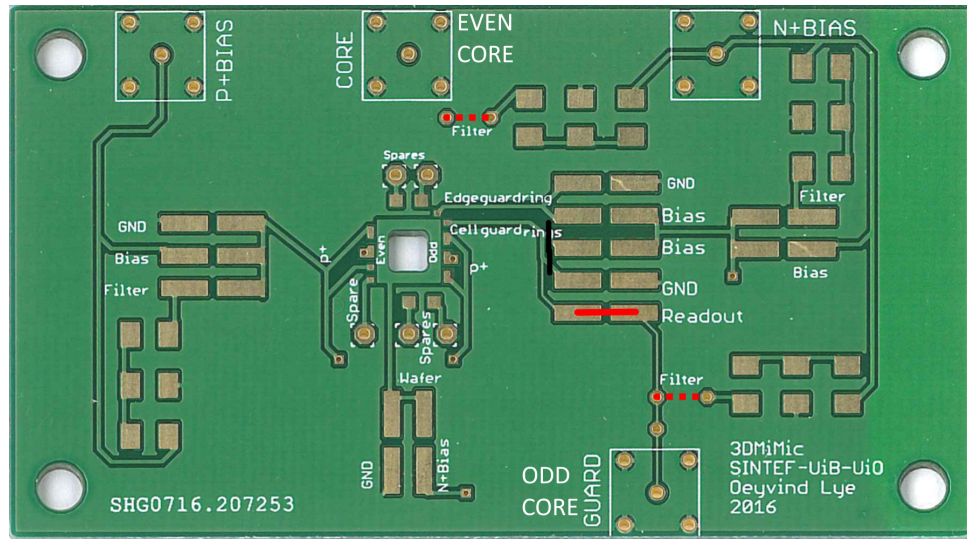


Figure C.9: Wiring for two channel readout on a detector without n+ guard rings.

A new version of the PCB layout will be designed and published to UiB's Macaos account shortly after this thesis is delivered. It will be designed specifically for two channel readout and feature some other minor improvements. This includes adding solder mask under the detector, adding option to mount the detector on the other side of the PCB, moving spare pads closer to the detector, and adding text for the connectors on the other side of the PCB.

Appendix D: List of Readout Electronics Systems

This appendix lists most readout electronics systems that has been considered during this project. ENC is shown for no detector connected, as not all specifications noted how the noise changes with capacitance. Some of the systems have a multiplexed output, which might be a problem in case many channels need to be read out continuously.

Table D.1: Readout electronics systems that has been considered for use during this project.

	Channels	Shaping time [ns]	ENC [e-]	Dynamic range [fC]	ADC bins	Reference	Note
CSAs with ADC							
Portable UiO System	2	1100	15750	2.5	32M	5200	12 bit
IDEAS VATA451	64	600 to 4000	30	0.005	10000	1.6	[Tali, 2015] [Oltedal, 2015]
R ³ B tracker ASIC	128	500 to 8000	7000	1.1	13.9M	2200	10 bit [IDEAS, 2016] [Jones et al., 2016]
CSAs without ADC							
ORTEC 142A	1		444	0.07	55M	8800	[ORTEC, 2011]
PANDA APFEL	22000		2600	0.42	18.8M	3000	No shaper
ALICE TPC PASA	16	190	244	0.04	938k	150	No shaper
IDEAS IDE1140	64	5000 to 8000	98	0.016	1.25M	200	[Soltveit et al., 2012]
IDEAS IDE1180	16	20 to 40	1106	0.18	2.5M	400	[IDEAS, 2016]
IDEAS IDE3465	16	1000	3500	0.56	16.2M	2600	[Mahlum et al., 2015]
	4	1000	26000	4.2	162M	26000	[IDEAS, 2016]
IDEAS IDE3466	32	1000	42000	6.7	16.2M	2600	Multiplexed
IDEAS VA32HDR14.2	4	1000	2700	0.4	162M	26000	Multiplexed
	32	2000	81M	1.3000	[IDEAS, 2016]	Multiplexed	
CSAs with ToT							
Timepix3	256x256	25ns to 410us	70	0.011	150k	24	[Llopert, 2011]
VELOpix	256x256	Low	1500	0.24	44.4k	7.1	Work in progress
Dosepix	16x16						[Zang et al., 2015]

Appendix E: IDE1180 Gain Linearity Graphs

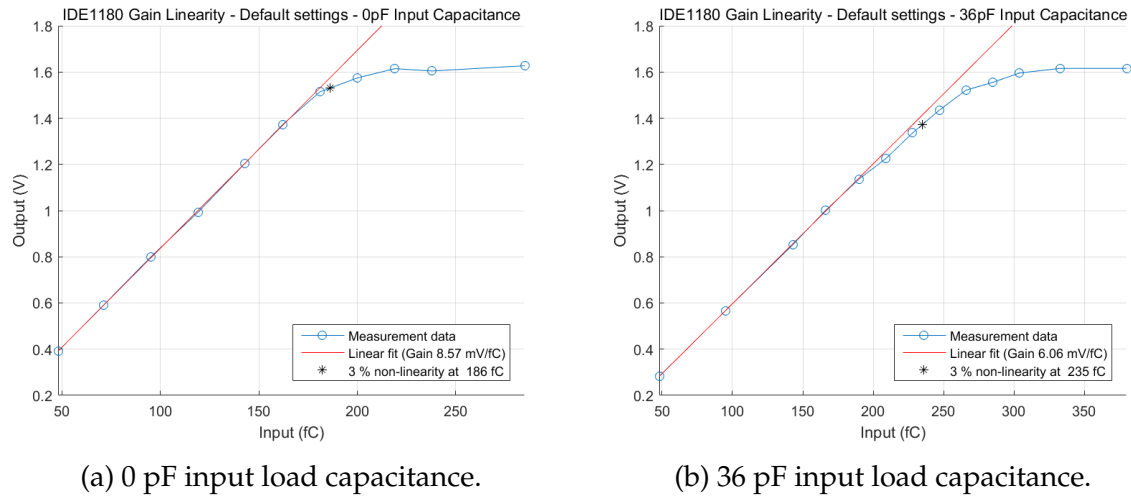


Figure E.1: Gain linearity measurements for default settings.

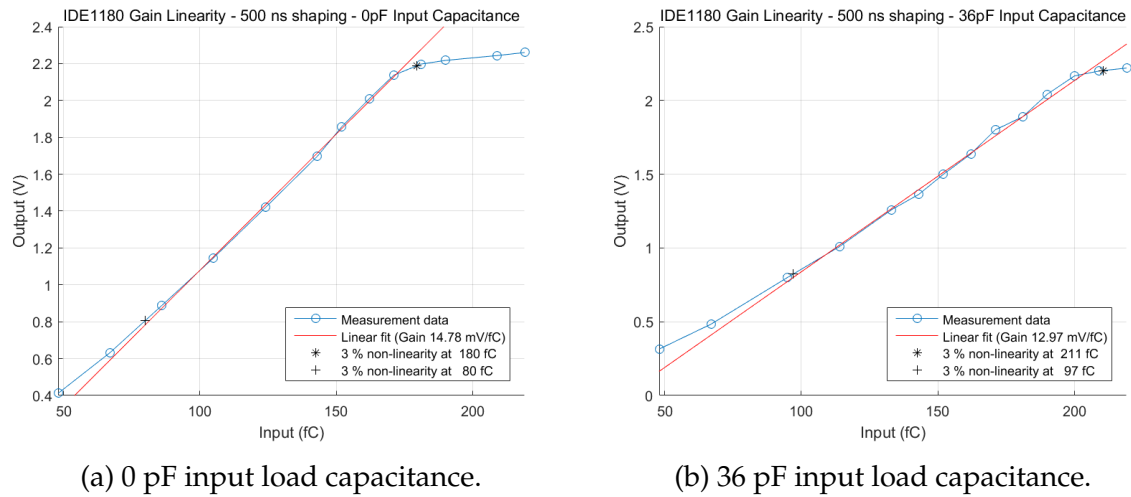


Figure E.2: Gain linearity measurements for 500 ns shaping time.

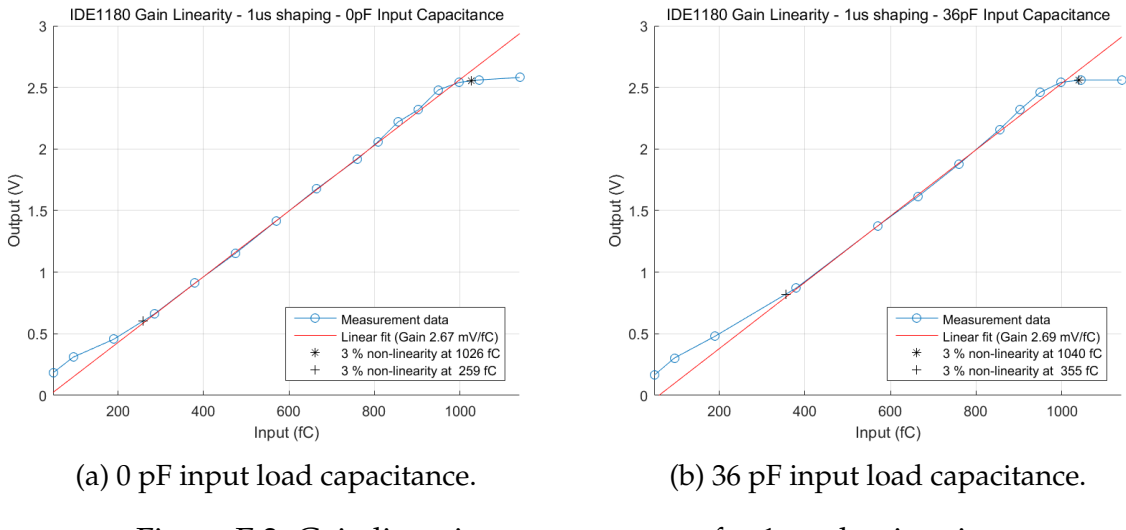


Figure E.3: Gain linearity measurements for 1 μ s shaping time.

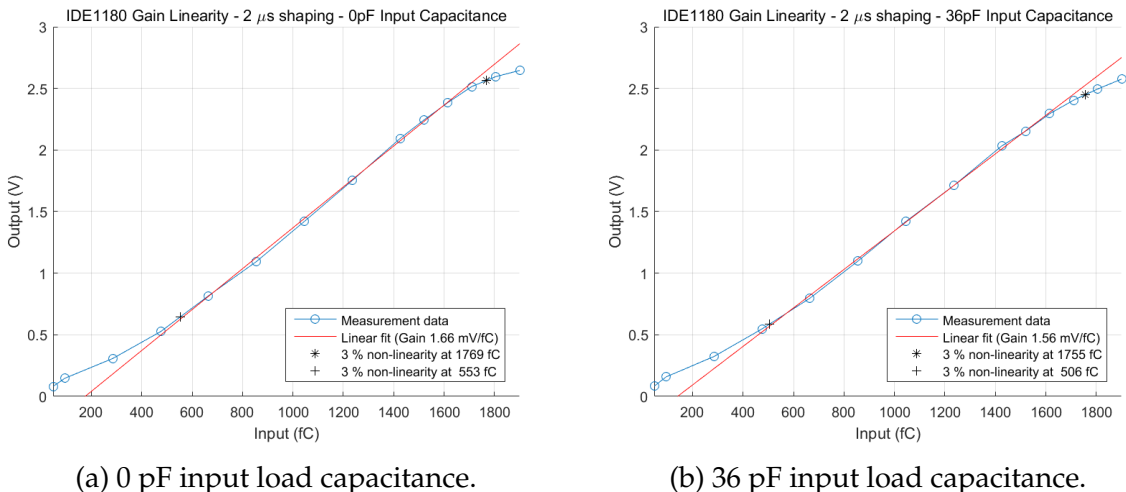


Figure E.4: Gain linearity measurements for 2 μ s shaping time.

Appendix F: IDE1180 Shape Graphs

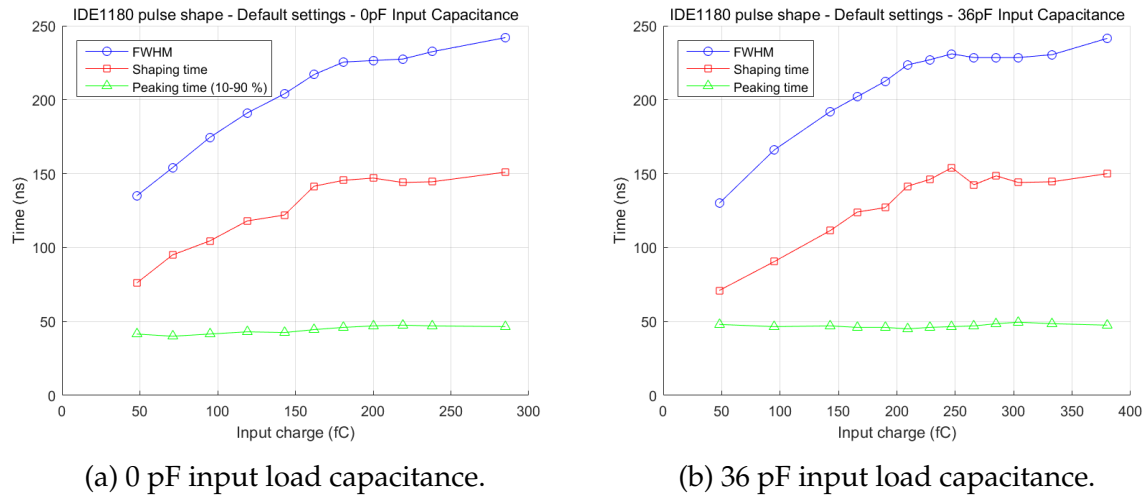


Figure F.1: Pulse shape parameters for default settings.

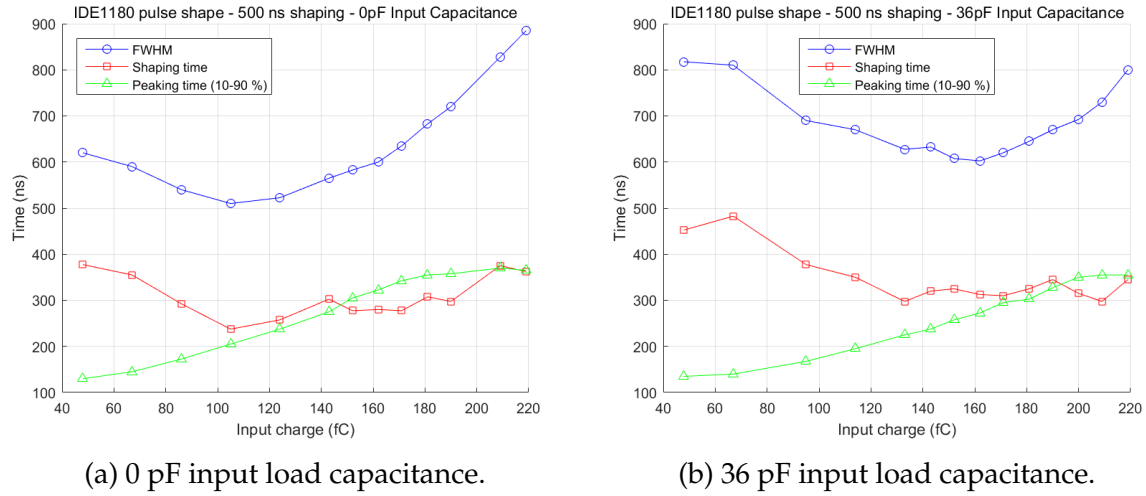


Figure F.2: Pulse shape parameters for 500 ns shaping time.

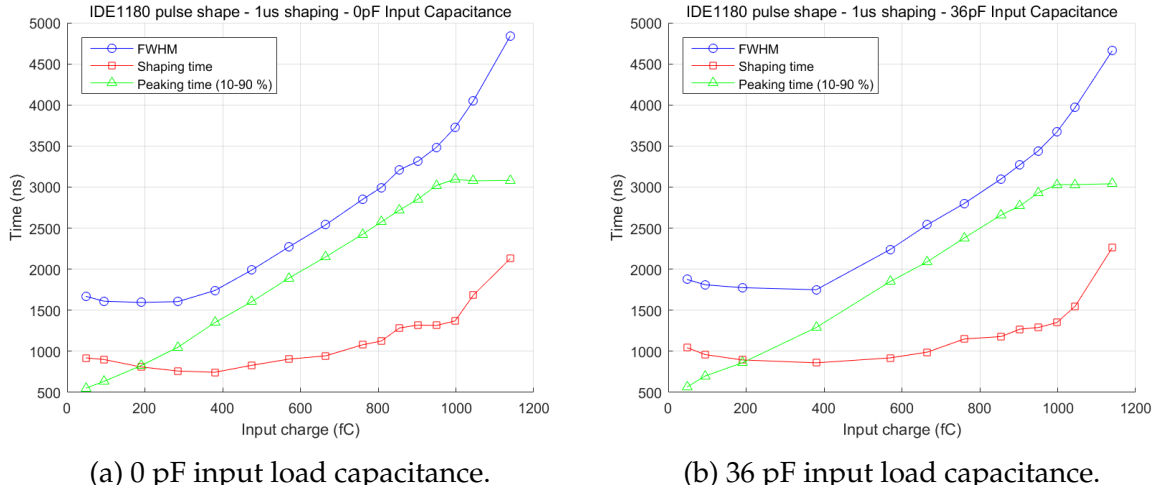


Figure F.3: Pulse shape parameters for 1 μ s shaping time.

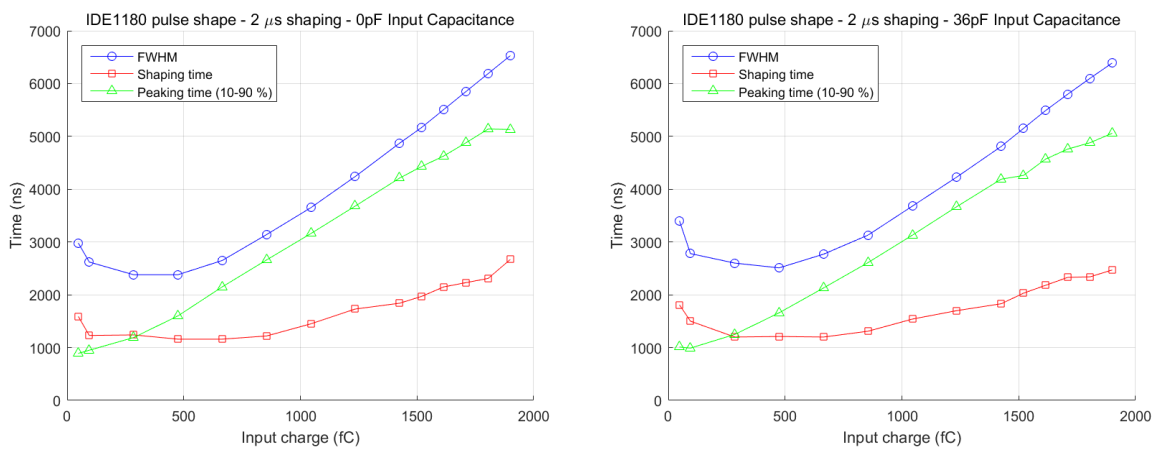


Figure F.4: Pulse shape parameters for 2 μ s shaping time.

Bibliography

- ASU (2000). Arizona State University: Mechanism for the Absorption of Light. <https://www.asu.edu/courses/phs208/patternsbb/PiN/rdg/mechanism/>. Accessed: 14/10/2015.
- Bansal, Y. (2015). PowerPoint-presentation: Characterization of Silicon based Neutron Pixel detectors.
- Bentley, J. P. (2005). *Principles of Measurement Systems*. Prentice Hall.
- Board of the Faculty of Clinical Radiology (2006). *Radiotherapy Dose-Fractionation*. Royal College of Radiologists, London.
- CERN. The Medipix website. <http://medipix.web.cern.ch/medipix/>. Accessed: 04/04/2016.
- Ermis, E. E. and C. Celiktas (2012). Timing Applications to Improve the Energy Resolution of NaI(Tl) Scintillation Detectors. *International Journal of Instrumentation Science* 1(5), 54–62. <http://article.sapub.org/10.5923.j.instrument.20120105.01.html>.
- Flemming, H. and P. Wieczorek (2011). Low noise preamplifier asic for the panda experiment. *Journal of Instrumentation* 6(12), C12055.
- Freeman, T. (2013). The potential of proton CT. <http://medicalphysicsweb.org/cws/article/research/53211>. Accessed: 15/10/2015.
- Gray, P. R., P. J. Hurstand, S. H. Lewis, and R. G. Meyer (2009). *Analysis and Design of Analog Integrated Circuits*. Wiley.
- Halámek, J., I. Visčor, and M. Kasal (2001). Dynamic range and acquisition system. *MEASUREMENT SCIENCE REVIEW* 1(1). <http://www.measurement.sk/PAPERS/Halamek1.pdf>.
- Hamamatsu (2001, 10). *Characteristics and use of Charge amplifier* (KACC9001E01 ed.). Hamamatsu Photonics.
- Hysing, L. B. (2015). Geometrical uncertainties in radiotherapy. Powerpoint presentation from PHYS213 lecture October 2015 at UiB.

IDEAS (2016). Ideas webpage. <http://www.ideas.no/>. Accessed: 10/09/2016.

Iniewski, K. (2010). *Electronics for Radiation Detection*. CRC Press.

JLab. Jefferson Lab: Radiation worker training: Effects of radiation on cells. https://www.jlab.org/div_dept/train/rad_guide/effects.html. Accessed: 06/10/2015.

Jones, L., S. Bell, Q. Morrissey, M. Prydderch, I. Church, I. Lazarus, M. Kogimtzis, V. Pucknell, M. Labiche, J. Thornhill, and M. Borri (2016). A 128-channel event driven readout asic for the r3b tracker. *Journal of Instrumentation* 11(02), C02076.

Khan, F. M. and J. P. Gibbons (2014). *Khan's The Physics of Radiation Therapy*. Lippincott Williams and Wilkins.

Knoll, G. F. (2010). *Radiation Detection and Measurement*. Wiley.

Llopart, X. (2011). Design of the timepix3. https://indico.cern.ch/event/122027/contributions/88228/attachments/69334/99368/FEE_Xavi_Final.pptx.

LU (1994). Table of Radioactive Isotopes. <http://nucleardata.nuclear.lu.se/toi/nuclide.asp?iZA=950241>. Accessed: 06/09/2016.

Lynnebakken, H. (2012). Jubler for partikkelterapi. <http://www.mn.uio.no/fysikk/forskning/aktuelt/aktuelle-saker/2012/jubler-for-partikkelterapi.html>. Accessed: 24/09/2015.

Maehlum, G. (2015, 11). IDE1180-EvalBoard V9 Schematic.

Maehlum, G., D. Meier, and T. Stein (2015, 11). *IDE1180 Preliminary Datasheet (V1R3 ed.)*. IDEAS.

Meier, D. (2016). From email conversation.

NIH (2010). National Institutes of Health: Radiation Therapy for Cancer. <http://www.cancer.gov/about-cancer/treatment/types/radiation-therapy/radiation-fact-sheet>. Accessed: 09/10/2015.

Oltedal, E. J. (2015). FPGA based readout of a silicon PIN detector.

ORTEC (2009). Introduction to amplifiers. <http://www.ortec-online.com/download/amplifier-introduction.pdf>.

ORTEC (2011, 03). *142A, B, and C Preamplifiers* (030211 ed.). ORTEC. <http://www.ortec-online.com/download/142A-B-C.pdf>.

P-Cure. P-Cure Clinics. <http://www.p-cure.com/index.aspx?id=4013>. Accessed: 12/10/2015.

Paganetti, H. (2012). Range uncertainties in proton therapy and the role of monte carlo simulations. *Physics in Medicine and Biology* 57(11), R99. <http://stacks.iop.org/0031-9155/57/i=11/a=R99>.

Poulianitis, T. (2016). Project work.

Povoli, M. (2016). From email conversation.

Povoli, M. et al. (2015). Simulation and testing of thin silicon microdosimeters realized with planar technology. <https://indico.cern.ch/event/351695/contributions/828320/>.

Samnøy, A. T. (2016). Ph.D. work.

Schroder, D. K. (2005). *Semiconductor material and device characterization*. Wiley.

Serway, R. A. and J. W. Jewett (2014). *Physics for Scientists and Engineers with Modern Physics*. Cenage Learning.

SINTEF (2015). Si-3DMiMic - Silicon-based 3D Mini and Micro-dosimeters. <https://www.sintef.no/en/projects/3dmimic/>. Accessed: 24/09/2015.

Soltveit, H., J. Stachel, P. Braun-Munzinger, L. Musa, H. Gustafsson, U. Bonnes, H. Oeschler, L. Osterman, and S. Lang (2012). The preamplifier shaper for the al-ice tpc-detector. <https://arxiv.org/abs/1203.3564>.

SparkFun. Real diode characteristics. <https://learn.sparkfun.com/tutorials/diodes/real-diode-characteristics>. Accessed: 26/08/2016.

Tali, M. (2015). Portable Front-End Readout System for Radiation Detection.

van Zeghbroeck, B. (2011). *Principles of Semiconductor Devices*.

Young, H. D., R. A. Freedman, and L. Ford (2007). *University Physics with Modern Physics*. Addison-Wesley.

Ytre-Hauge, K. S. (2015). Radiation therapy with photons, protons and carbon ions. Powerpoint presentation from PHYS231 lecture march 2015 at UiB.

Zang, A., G. Anton, R. Ballabriga, F. Bisello, M. Campbell, J. Celi, A. Fauler, M. Fiederle, M. Jensch, N. Kochanski, X. Llopart, N. Michel, U. Mollenhauer, I. Ritter, F. Tennert, S. Wölfel, W. Wong, and T. Michel (2015). The dosepix detector—an energy-resolving photon-counting pixel detector for spectrometric measurements. *Journal of Instrumentation* 10(04), C04015.

Glossary

ADC Analog-to-Digital Converter.

ASIC Application-Specific Integrated Circuit.

C-V Capacitance-Voltage.

CSA Charge-sensitive pre-amplifier.

CT Computed Tomography.

ENC Equivalent Noise Charge.

ENOB Effective number of bits.

FPGA Field-Programmable Gate Array.

FWHM Full width at half maximum.

I-V Current-Voltage.

IFT Department of Physics and Technology.

LET Linear Energy Transfer.

MIP Minimum Ionizing Particle.

op-amp Operational amplifier.

PCB Printed Circuit Board.

PCIe Peripheral Component Interconnect Express.

PMMA Polymethyl methacrylate.

RBE Relative Biologic Effectiveness.

SOBP Spread-Out Bragg Peak.

ToT Time over Threshold.

UiB University of Bergen.

UiO University of Oslo.

UOW University of Wollongong.